

Report Number 1643.01  
QA Report Number 34001.01-R013

PROBABILISTIC EVALUATION OF THE DIABLO CANYON  
TURBINE BUILDING SEISMIC CAPACITY  
USING NONLINEAR TIME HISTORY ANALYSES

Prepared For  
Pacific Gas & Electric Company  
77 Beale Street  
San Francisco, California 94106

Prepared By  
R. P. Kennedy  
D. A. Wesley  
W. H. Tong

December, 1988

8901100094 890104  
PDR ADOCK 05000275  
P PDC



ENCLOSURE

PROBABILISTIC EVALUATION OF THE DIABLO CANYON  
TURBINE BUILDING SEISMIC CAPACITY  
USING NONLINEAR TIME HISTORY ANALYSES



## TABLE OF CONTENTS

<u>Section</u>		<u>Page</u>
1.	INTRODUCTION	1-1
2.	TURBINE BUILDING MODEL	2-1
2.1	Shear Behavior of Shear Walls	2-5
2.1.1	Shear Strength	2-5
2.1.2	Shear Stiffness	2-12
2.1.3	Shear Wall Drift Limits	2-13
2.1.4	Force-Deflection Relationship For Shear Drift	2-17
2.2	Flexural Behavior of Shear Walls	2-26
2.2.1	Flexural Strength	2-26
2.2.2	Flexural Stiffness	2-32
2.2.3	Flexural Drift Limits	2-35
2.2.4	Force-Deflection Relationship For Flexural Drift	2-35
2.3	Operating Floor Beam Elements	2-36
2.4	Turbine Pedestal	2-39
2.5	Other Modelling Considerations	2-39
2.6	Treatment of Randomness and Uncertainty	2-42
3.	EARTHQUAKE GROUND MOTION RECORDS	3-1
4.	LINEAR ELASTIC RESPONSE FOR MEDIAN GROUND MOTION INPUT	4-1
5.	NONLINEAR ANALYSES WITH MEDIAN STRUCTURE PROPERTIES	5-1
5.1	Results	5-1
5.2	Prediction of Median (Randomness Only) Fragility From Elastic Results	5-7
5.3	Influence of Ground Motion Characteristics on Shear Wall Drift	5-25



## TABLE OF CONTENTS (Continued)

<u>Section</u>		<u>Page</u>
6.	NONLINEAR ANALYSES WITH UNCERTAIN STRUCTURE PROPERTIES	6-1
6.1	Results	6-1
6.2	Prediction of Fragility Including Uncertainty from Elastic Results	6-7
6.3	Other Sources of Variability and Conservatism	6-10
6.4	Influence of Ground Motion Characterization on Shear Wall Drift When Structure Parameter Variation is Incorporated	6-12
6.5	Influence of Structure Property Variability on Shear Wall Drift	6-16
7.	CONCLUSIONS	7-1
7.1	Overview of Study	7-1
7.2	Primarily Deterministic Observation on the Influence of Structure Property and Ground Motion Variation on Shear Wall Drifts	7-9
7.3	Observation on Potential for Impact Between Turbine Pedestal and Operating Floor	7-22
7.4	Probabilistic Capacity (Fragility) Estimates Resulting From Nonlinear Analyses	7-23
7.5	Prediction of Fragility from a Single Median Centered Elastic Analysis	7-29
8.	REFERENCES	8-1



## LIST OF FIGURES

<u>Figure</u>	<u>Title</u>	<u>Page</u>
2-1	Unit 2 Turbine Building Concrete Outline (E1 140 Feet)	2-45
2-2	Schematic Illustration of Turbine Building Nonlinear Model	2-46
2-3	Diablo Canyon Turbine Building DRAIN-2D Model	2-47
2-4	Strength of Concrete Shear Walls	2-48
2-5	Cyclic Load-Deflection Behavior of Concrete Shear Walls	2-49
2-6	Shear Deformation Hysteretic Behavior	2-50
2-7	Characteristics of the Hysteresis Model and Identification of Model Parameters	2-51
2-8	Shear Force-Drift Relationship for Lowest Element of Wall 31	2-52
2-9	Standard Takeda Model for Flexural Deformation Hysteretic Behavior	2-53
2-10	Shear-Deformation Curve for the Beam-Like Portion of the Operating Diaphragm at the Midspan	2-54
2-11	Shear-Deformation Curve for the Turbine Pedestal	2-55
3-1	Gazli, U.S.S.R., 17 May 1976, Karakyr Point, Component North, 5% Damped Spectral Acceleration - Record 1 Scaled to $\bar{S}_a = 3.0g$	3-12
3-2	Gazli, U.S.S.R., 17 May 1976, Karakyr Point, Component East, 5% Damped Spectral Acceleration - Record 2 Scaled to $\bar{S}_a = 3.0g$	3-13
3-3	Tabas, Iran, 16 September 1978, Component N74E, 5% Damped Spectral Acceleration - Record 3 Scaled to $\bar{S}_a = 3.0g$	3-14
3-4	Tabas, Iran, 16 September 1978, Component N16W, 5% Damped Spectral Acceleration - Record 4 Scaled to $\bar{S}_a = 3.0g$	3-15



## LIST OF FIGURES (Continued)

<u>Figure</u>	<u>Title</u>	<u>Page</u>
3-5	San Fernando, CA, 09 February 1971, Pacoima Dam Component S16E, 5% Damped Spectral Acceleration - Record 5 Scaled to $\bar{S}_a = 3.0g$	3-16
3-6	San Fernando, CA, 09 February 1971, Pacoima Dam Component S74W, 5% Damped Spectral Acceleration - Record 6 Scaled to $\bar{S}_a = 3.0g$	3-17
3-7	San Fernando, CA, 09 February 1971, Lake Hughes #12, Component N21E, 5% Damped Spectral Acceleration - Record 7 Scaled to $\bar{S}_a = 3.0g$	3-18
3-8	San Fernando, CA, 09 February 1971, Lake Hughes #12, Component N69W, 5% Damped Spectral Acceleration - Record 8 Scaled to $\bar{S}_a = 3.0g$	3-19
3-9	San Fernando, CA, 09 February 1971, Castaic, Component N69W, 5% Damped Spectral Acceleration - Record 9 Scaled to $\bar{S}_a = 3.0g$	3-20
3-10	Imperial Valley, CA, 15 October 1979, El Centro, Component, N00E, 5% Damped Spectral Acceleration - Record 10 Scaled to $\bar{S}_a = 3.0g$	3-21
3-11	Imperial Valley, CA, 15 October 1979, El Centro, Component N90W, 5% Damped Spectral Acceleration - Record 11 Scaled to $\bar{S}_a = 3.0g$	3-22
3-12	Imperial Valley, CA, 15 October 1979, El Centro #4, Component S50W, 5% Damped Spectral Acceleration - Record 12 Scaled to $\bar{S}_a = 3.0g$	3-23
3-13	Imperial Valley, CA, 15 October 1979, El Centro #4, Component S40E, 5% Damped Spectral Acceleration - Record 13 Scaled to $\bar{S}_a = 3.0g$	3-24
3-14	Parkfield, CA, 27 June 1966, Temblor, Component N65W, 5% Damped Spectral Acceleration - Record 14 Scaled to $\bar{S}_a = 3.0g$	3-25
3-15	Parkfield, CA, 27 June 1966, Temblor, Component S25W, 5% Damped Spectral Acceleration - Record 15 Scaled to $\bar{S}_a = 3.0g$	3-26



## LIST OF FIGURES (Continued)

<u>Figure</u>	<u>Title</u>	<u>Page</u>
3-16	Morgan Hill, CA, 24 April 1984, Coyote Lake Dam, Component N75W, 5% Damped Spectral Acceleration - Record 16 Scaled to $\bar{S}_a = 3.0g$	3-27
3-17	Morgan Hill, CA, 24 April 1984, Coyote Lake Dam Component S15W, 5% Damped Spectral Acceleration - Record 17 Scaled to $\bar{S}_a = 3.0g$	3-28
3-18	Coalinga, CA, 02 May 1983, Pleasant Valley Pump Station, (Switch-yard), Component 045, 5% Damped Spectral Acceleration - Record 18 Scaled to $\bar{S}_a = 3.0g$	3-29
3-19	Coalinga, CA, 02 May 1983, Pleasant Valley Pump Station, (Switch-yard), Component 135, 5% Damped Spectral Acceleration - Record 19 Scaled to $\bar{S}_a = 3.0g$	3-30
3-20	Dayhook, Scaled (X1.7), Component N10E, Baseline Corrected, 5% Damped Spectral Acceleration - Record 20 Scaled to $\bar{S}_a = 3.0g$	3-31
3-21	Dayhook, Scaled (X1.7), Component N80W, Baseline Corrected, 5% Damped Spectral Acceleration - Record 21 Scaled to $\bar{S}_a = 3.0g$	3-32
3-22	DCPP, North M=7.0, Strike Slip Bilateral, 5% Damped Spectral Acceleration - Record 22 Scaled to $\bar{S}_a = 3.0g$	3-33
3-23	DCPP East M=7.0, Strike Slip Bilateral, 5% Damped Spectral Acceleration - Record 23 Scaled to $\bar{S}_a = 3.0g$	3-34
3-24	DCPP North M=7.0 Strike Slip Unilateral, 5% Damped Spectral Acceleration - Record 24 Scaled to $\bar{S}_a = 3.0g$	3-35
3-25	DCPP East M=7.0 Strike Slip Unilateral, 5% Damped Spectral Acceleration - Record 25 Scaled to $\bar{S}_a = 3.0g$	3-36
3-26	Acceleration Response Spectra for Three Empirical Records Scaled to an Average Spectral Acceleration of 3.0g Over the Frequency Range of 3 to 8.5 Hertz	3-37



## LIST OF FIGURES (Continued)

<u>Figure</u>	<u>Title</u>	<u>Page</u>
3-27	Mean, Median, 84% NEP, and Upper Bound Spectra for Ensemble of 25 Scaled Records ( $\bar{S}_a = 2.25g$ )	3-38
5-1	Bilinear Force - Deflection Relationship Versus Pseudo Elasto-Perfectly Plastic Relationship of Equal Area and Equal Capacity $V_u$	5-32
5-2	Cumulative Probability Plots of Natural Logarithm of Drifts	5-33
6-1	Maximum Story Drift for $\bar{S}_a = 3.0g$ Versus Damping	6-19
6-2	Maximum Story Drift for $\bar{S}_a = 3.0g$ Versus Shear Wall Stiffness Ratio	6-20
6-3	Maximum Story Drift for $\bar{S}_a = 3.0g$ Versus Shear Wall Strength Ratio	6-21
6-4	Maximum Story Drift for $\bar{S}_a = 3.0g$ Versus Operating Floor Stiffness Ratio	6-22
6-5	Maximum Story Drift for $\bar{S}_a = 3.0g$ Versus Operating Floor Strength Ratio	6-23
6-6	Maximum Story Drift for $\bar{S}_a = 3.0g$ Versus Turbine Pedestal Stiffness Ratio	6-24
6-7	Maximum Story Drift for $\bar{S}_a = 3.0g$ Versus Turbine Pedestal Strength Ratio	6-25



## LIST OF TABLES

<u>Table</u>	<u>Title</u>	<u>Page</u>
2-1	Turbine Building Nonlinear Model Node Coordinates	2-56
2-2	Turbine Building Nonlinear Model Nodal Masses	2-57
2-3	Median Capacities of Shear Wall Elements	2-58
2-4	Effective Shear Wall Elastic Shear and Flexural Stiffness	2-59
2-5	Ratio of Total Drifts to Shear-Only Drifts and Equivalent Total Drift Knockdown Factor Used	2-60
2-6	Elastic Modal Properties of the Turbine Building Model with Median Structure Properties	2-61
2-7	Model Structural Property Values	2-62
3-1	Earthquake Time Histories	3-39
4-1	Elastically Computed Response for Figure 3-27 Median Spectrum Scaled to $\bar{S}_a = 2.25g$	4-5
5-1	Nonlinear Results for Median Structural Model at $\bar{S}_a = 3.0g$	5-34
5-2	Nonlinear Results for Median Structural Model at $\bar{S}_a = 6.0g$	5-35
5-3	Elastic Deformed Shape at Yield Versus Inelastic Deformed Shapes at Several Different Drift Levels for Wall 31	5-36
5-4	Estimated $F_y$ Values from Spectral Averaging Method for Various <sup>u</sup> Maximum Story Drifts in Wall 31	5-37
5-5	Estimated $F_y$ Values From Various Methods at Differing Maximum Story Drifts for Wall 31	5-38
6-1	Nonlinear Results for Uncertain Structural Properties	6-26
6-2	Comparison of Median and 90% Bounds on Drifts for $\bar{S}_a = 3.0g, 4.0g$ and $6.0g$ With and Without Uncertainty <sup>t</sup> on Structural Properties	6-27
6-3	Comparison of Fragility Estimates from Extrapolating Results of a Single Median-Centered Elastic Analysis With Results from Multiple Nonlinear Time-History Analyses	6-28
6-4	Turbine Building Fragility Estimate Incorporating Additional Variable Parameters	6-29



## 1. INTRODUCTION

During Phase II of the Diablo Canyon Long Term Seismic Program (LTSP) study, probabilistic seismic capacity estimates were made for all of the important civil structures using the standard fragility evaluation method described in References 1 and 2. This standard fragility evaluation method has been applied in the seismic probabilistic risk assessment of over thirty nuclear power plants and is well documented in many additional references. From the Phase II LTSP evaluation, it was found that the Turbine Building has the lowest seismic capacity of the important Diablo Canyon civil structures and is the only one that could possibly be a significant contributor to the seismic-induced risk of core damage.

The standard fragility evaluation method essentially involves artificially raising the ground motion level to obtain failure. The idea is not to predict failure at expected ground motion level but at a hypothetically higher level. During the Phase II study, a number of possible failure modes which could lead to overall severe distress of the Turbine Building were investigated using the standard fragility evaluation method. It was concluded that the most probable cause of overall severe distress of the Turbine Building was substantial inelastic drift and strength degradation of the two major east-west load



carrying shear walls spanning from foundation level (E1 85 feet) to the operating floor (E1 140 feet). It was further judged that conditions for these two walls was slightly more severe in Unit 2 than in Unit 1.

A series of nonlinear time-history analyses of the east-west earthquake response of the Unit 2 Turbine Building were performed with emphasis on the two major east-west load carrying shear walls below the operating floor. In these analyses, structural damping as well as both the strength and stiffness of each of the major east-west seismic load-carrying elements influencing the behavior of the shear walls were probabilistically varied. To account for the variability of ground motion characteristics, twenty five (25) different earthquake ground motion time-histories each with the same average spectral acceleration over the frequency range of interest were used. A total of fifty (50) nonlinear time history analyses (each of the 25 ground motion records used twice) were conducted at a specified average spectral acceleration in order to probabilistically describe the resulting inelastic drift of the major east-west shear walls. A criterion relating inelastic drift to probability of severe distress and strength degradation was specified for these walls. Using this criterion, the probability of severe wall distress was estimated for each of the 50 analyses. This process was repeated at three different average spectral acceleration levels. The probability of severe wall distress as a function of the three average



spectral acceleration levels was then estimated. It was found that the resultant probabilities of severe wall distress could be reasonably fit by a lognormal distribution. This determination formed the basis for estimates of the median capacity (50% probability of severe distress) and randomness (ground motion related) and uncertainty (structure related) variabilities. It was also found that the substantially largest source of variability of shear wall drifts comes from ground motion variation and not from uncertainty in structure properties. Therefore, differences of opinion over structural strength, stiffness, and damping properties are relatively unimportant compared to variability in ground motion characteristics.

The purposes of this study were to:

1. Improve the Phase II LTSP study fragility estimate for severe overall distress of the Turbine Building, and
2. Compare the fragility estimate based upon multiple nonlinear analyses with the estimate extrapolated from a single median-centered elastic response spectrum analysis obtained using the standard separation-of-variables fragility evaluation method.

This report describes the probabilistic nonlinear analysis of the Turbine Building and presents the results obtained from this study. It should be emphasized that this study is concerned with the prediction of ground motion levels associated with the onset of severe structural



distress and significant strength degradation of the major east-west shear walls of the Turbine Building and not the prediction of failure capacity. It is the authors' opinion that the prediction of partial or total collapse is essentially impossible for such a civil structure. In the Diablo Canyon seismic probabilistic risk assessment, the onset of severe structural distress of the east-west shear walls was conservatively used as a surrogate for the structure-induced failure of all safety equipment housed in the Turbine Building. While the precise degree of conservatism introduced by this substitution would be difficult, if not impossible, to ascertain, it is reasonably certain that it is considerable.



## 2. TURBINE BUILDING MODEL

Figure 2-1 shows a plan view of the Unit 2 Turbine Building; Figure 2-2 presents a schematic elevation view, emphasizing the major east-west shear walls at Column Lines 19 and 31 (herein called Wall 19 and Wall 31) which support the heavy operating floor at E1 140 feet. There is an east-west braced frame on line 35; however, it is neglected for simplification of the model, resulting in some conservatism in wall demands. Essentially, Walls 19 and 31 are the only two major walls available to resist east-west drift of the heavy operating floor. In turn, nearly all of the in-plane lateral loads imposed on these two walls come from the east-west inertial loads of the operating floor plus their own self-weight. Although additional in-plane loads enter due to east-west inertial loads at intermediate floors (E1 104 feet and 123 feet at Wall 19 and E1 107 feet and 119 feet at wall 31), these floor masses are small compared to that of the operating floor, and much of their east-west inertial load is carried by external buttresses added to the Turbine Building. The inertial loads transferred into Walls 19 and 31 from the superstructure above the operating floor are also small; they were approximated by a slight increase in the weight at the operating floor level. The base of Walls 19 and 31 are at E1 85 feet. Each wall is 55 feet high by approximately 137 feet long and contain several openings (particularly Wall 19). The thickness of Wall 19 above



E1 104 feet is 20 inches; below E1 104 feet the wall thickness varies but averages about 35 inches. Wall 31 is 24 inches thick over its entire height. Thus, these walls are long relative to their height and are rather thick.

The operating floor consists of a 12 inch concrete slab supported on a steel beam framing system. It is 139 feet wide and 267 feet long between Wall 19 and 31 plus a 77 foot overhang beyond Wall 31. The slab contains a cutout for the independently supported turbine pedestal that is approximately 59 feet wide by 212 feet long. Thus, for east-west lateral forces, the operating floor was treated as two independent 267 foot long by about 40 foot deep beams between Walls 19 and 31. The stiffness and capacity of these beams are influenced by the small cutouts shown on Figure 2-1.

A minimum gap of 3.375 inches exists between the turbine pedestal and the operating floor. This gap is insufficient to preclude impact between the turbine pedestal and the operating floor at the high ground motion levels of interest in the fragility evaluation. Furthermore, the effective inertial mass to be lumped at the top of the turbine pedestal exceeds the entire inertial mass supported by Wall 19 plus Wall 31; therefore, it was judged that impact could possibly lead to additional distress in the shear walls. Thus, the turbine pedestal was included in



the nonlinear model together with a gap element interconnecting it to the operating floor beam elements on each side.

Because the turbine pedestal and the operating floor beam elements are very ductile, they are each capable of undergoing lateral drifts in excess of 18 inches before failure while the stiff shear Walls 19 and 31 are expected to suffer severe distress at lateral drifts of 6 inches or less at the operating floor level. Thus, severe distress of the shear walls is expected to occur well before failure of either the operating floor beam elements or the turbine pedestal (see nonlinear results in Table 5-2). For this reason Walls 19 and 31 were modeled in more detail than either the operating floor beam elements or the turbine pedestal. The operating floor and turbine pedestal were only modelled in sufficient detail to approximate their potential for distributing inertial loads to the shear walls.

The shear walls were modelled into three segments each along their height (E1 85 feet to 104 feet, 104 feet to 123 feet, and 123 feet to 140 feet for Wall 19, and E1 85 feet to 107 feet, 107 feet to 119 feet, and 119 feet to 140 feet for Wall 31). These segments were chosen because they correspond to points where both the stiffness and strengths of the walls greatly change. Because of the low height-to-length ratio, the wall shear stiffness is less than the flexural stiffness



(particularly for Wall 31). Except for segment 2 of Wall 19 (E1 104 feet to 123 feet), where the flexural capacity (controlled by yield moment) and the shear yield capacity are essentially equal, the shear capacity is less than the flexural capacity. Although probably unnecessary, it was decided to model each shear wall segment with both a nonlinear shear element and a nonlinear flexural element combined in series because each element has different nonlinear properties. This modelling has the slight advantage of separately defining shear deformations from flexural deformations so that the probability of severe distress criteria could be defined in terms of inelastic shear deformations. To properly account for rotational effects, the flexural elements were assigned a length equal to the segment height and the series coupled shear elements were given a very short length relative to the flexural elements. Each element type was provided with appropriate nonlinear force-deflection characteristics. This approach to nonlinear modelling of shear walls has previously been used in References 3 and 5 and the details are discussed in greater depth therein.

The analysis was only concerned with east-west response due to an east-west input; therefore, the schematic model shown in Figure 2-2 was simplified into the two-dimensional model shown in Figure 2-3 which is compatible with the DRAIN-2D nonlinear analysis computer program (Reference 28). The Turbine Building model node coordinates and nodal



masses are given in Tables 2-1 and 2-2, respectively. Stiffness and strength characteristics of each element are discussed in the following subsections. Mass, stiffness, and strength characteristics of the operating floor elements and the turbine pedestal were provided by Pacific Gas and Electric (Reference 30).

The model shown in Figures 2-2 and 2-3 with the properties described herein was developed based on a review of Turbine Building responses obtained from the substantial 3-D finite element model of the entire building used during the design process. Based on this review, it was judged that the simple model shown in Figure 2-3 was fully adequate to describe the in-plane shear wall behavior of Walls 19 and 31. This model adequately represents the shear and moments induced in these walls by the overall building response. This model also properly describes the nonlinear response characteristics of the shear walls, including the influence of nonlinear behavior of the operating floor and turbine pedestal impact.

## 2.1 Shear Behavior of Shear Walls

### 2.1.1 Shear Strength

Barda (Reference 7) determined that the ultimate shear strengths of low-rise walls (height less than length) can be represented by the following relationship:



$$\begin{aligned} v_U &= v_C + v_S \\ &= 8.3 \sqrt{f'_C} - 3.4 \sqrt{f'_C} \left( \frac{h_W}{l_W} - 0.5 \right) + \rho_n f_y \end{aligned} \quad (2-1)$$

where:

$v_U$  = Ultimate shear strength, psi

$v_C$  = Contribution from concrete, psi

$v_S$  = Contribution from steel reinforcement, psi

$f'_C$  = Concrete compressive strength, psi

$h_W$  = Wall height, in

$l_W$  = Wall length, in

$\rho_n$  = Vertical steel reinforcement ratio

$f_y$  = Steel yield strength, psi



The contribution of the concrete to the ultimate shear strength of the wall as a function of  $h_w/\ell_w$  is shown in Figure 2-4. Also shown in Figure 2-4 are the available test values (References 7 through 10) and the corresponding ACI 318-83 formulation. The tests included load reversals and varying reinforcement and  $h_w/\ell_w$  ratios. Web crushing generally controlled the failure of the test specimens. Tests were performed with no axial loads; however, an increase in shear capacity due to the presence of axial loads of  $N/4\ell_w t$  was recommended, where  $N$  is the axial load in pounds, and  $t$  is the wall thickness in inches.

One of the conclusions reached by Oesterle (Reference 10) was that for walls with  $h_w/\ell_w = 1$ , vertical steel has no effect, and the entire contribution to shear strength is due to the horizontal steel. In order to estimate the effect of the horizontal and vertical steel, the steel contribution to wall shear strength was determined from test values for the range of  $0.5 < h_w/\ell_w < 2$  using the test data from the above references. The effective steel shear strength was assumed to be in the form:

$$v_{se} = Av_{sn} + Bv_{sh} \quad (2-2)$$

where  $A$ ,  $B$  are constants and



$v_{sn} = \rho_n f_y$  = Vertical steel contribution to shear strength.

$v_{sh} = \rho_h f_y$  = Horizontal steel contribution to shear strength.

$\rho_h$  = Horizontal steel reinforcement ratio.

The constants A and B were calculated based upon the concrete contribution to the ultimate strength as given in Equation 2-1.

Constants A and B were approximated as follows in terms of the height-to-length ratio:

$\frac{h_w}{l_w}$	A	B
$\leq 0.5$	1	0
0.5 to 1.0	$-2.0(h_w/l_w)+2.0$	$2.0(h_w/l_w)-1.0$
$\geq 1.0$	0	1

Thus the median ultimate shear strength is given by:

$$\begin{aligned}
 v_u &= v_c + v_{se} \\
 &= 8.3 \sqrt{f'_c} - 3.4 \sqrt{f'_c} \left( \frac{h_w}{l_w} - 0.5 \right) + \frac{N}{4l_w t} + \rho_{se} f_y
 \end{aligned}
 \tag{2-3}$$



where  $\rho_{se} = A\rho_n + B\rho_h$  with A and B determined as shown above. The logarithmic standard deviation associated with this equation was estimated to be 0.20.

The data used to substantiate the median shear strength equations presented above were derived from tests conducted on cantilever walls whose height,  $h_w$ , was known. However, the Turbine Building east-west shear spans more than one story. For these walls, the equivalent cantilever wall height,  $h_{we}$ , was taken as the ratio of the in-plane moment to the in-plane shear at the section under consideration. The equivalent height,  $h_{we}$ , was used to determine the median wall shear strength and provides a more accurate representation of the moment-shear interaction.

The determination of the median shear strength of the lower story of Wall 31 of the Unit 2 Turbine Building is selected as an example. This wall is 2 feet thick and approximately 137 feet long. It is reinforced by No. 6 bars spaced 12 inches apart at both faces and in both the vertical and horizontal directions. There are also 56 #11 vertical trim bars at elevation 85'. These are utilized for flexural capacity only. Grade 60 steel was used for the vertical reinforcing steel while grade 40 was used for the horizontal direction. The median concrete



compressive strength was estimated to be 6600 psi and the median yield strengths were taken to be 66 ksi and 51 ksi for the vertical and horizontal bars, respectively. There are also structural steel columns embedded in Wall 31. Anchorage of these columns to the shear wall is provided by steel shear lugs welded to both flanges of the columns. The steel columns are expected to act as dowels to provide additional shear strength. However, at the bottom story, the shear strength contribution from these embedded steel columns is limited by the strength of the column anchor bolts which is much lower than the columns and thus dowel effects from the vertical columns were conservatively ignored in this lower segment. The equivalent cantilever wall height based on the elastic load distributions was estimated to be approximately 47 feet. Since the floor slabs are supported primarily by the structural steel frames, the effect of the axial load acting on the wall was neglected with slight resulting conservatism. The median concrete shear strength was found to be:

$$v_c = 8.3 \sqrt{6600} - 3.4 \sqrt{6600} (47/137 - 0.5)$$
$$= 718 \text{ psi}$$

The effective wall height-to-length ratio is less than 0.5 ( $47/137 = 0.34$ ) so the reinforcing steel shear strength was based upon the vertical wall reinforcement.



$$\rho_{se} = \rho_n$$

$$= \frac{2 \times 0.44}{24 \times 12} = 0.00306$$

The steel shear strength was found to be:

$$v_{se} = 0.00306 (66000) = 202 \text{ psi}$$

For a rectangular wall with uniformly distributed vertical reinforcement, the effective depth,  $d$ , from the extreme compressive fiber to the resultant of the tensile force was taken to be  $0.6 \lambda_w$  from Reference 9. The median wall shear strength was found to be:

$$v_u = (718 + 202) (0.6 \times 137 - \underbrace{3.38' - 6.33'}_{\text{openings}}) (2) (144) (10^{-3})$$

$$= 19,200 \text{ k}$$

At higher elevations up the wall, credit was taken for dowel behavior of the embedded steel columns. To determine the portion of shear carried by the columns, the columns were converted into equivalent concrete areas based on their relative shear modulus.



The median shear capacity,  $v_c$ , carried by the concrete (including dowel action) and the median ultimate capacity,  $v_u$ , are presented in Table 2-3. It is estimated that the logarithmic standard deviation associated with uncertainty of both  $v_c$  and  $v_u$  is about 0.25 when the uncertainty with Equation 2-3 and the uncertainty in concrete and steel strengths are both included. As a result, the 95% confidence capacities are estimated to be about 66% of the values listed in Table 2-3.

#### 2.1.2 Shear Stiffness

The shear stiffness of each shear wall segment was estimated by:

$$K_s = F_s \frac{A_v G}{h_w} \quad (2-4)$$

where  $A_v$  is the shear area,  $G$  is the shear modulus,  $h_w$  is the wall segment height, and  $F_s$  is a stiffness knock-down factor to account for concrete cracking. The shear area,  $A_v$ , was taken as the full cross-sectional area of the wall subtracting out the effects of major openings and not adding any stiffening effect from embedded steel columns. The shear modulus was taken as  $G = 2.85 \times 10^5$  KSF. The stiffness knock-down factor due to concrete cracking is uncertain for such thick, low-rise shear walls which do not have substantial normal stress. Tests by Los



Alamos National Laboratory for the U.S. Nuclear Regulatory Commission, Sozen, and others would indicate that at the concrete capacity level,  $V_C$ , the factor  $F_S$  is highly variable, but is generally well below unity. It was the authors' judgement to select a median value of  $F_S = 0.50$ ; thus, the median stiffness in shear was taken to be one-half the uncracked stiffness. The resulting median "elastic" shear stiffnesses for each wall segment are given in Table 2.4. Because of the highly uncertain nature of  $F_S$ , the logarithmic standard deviation to account for uncertainty in shear stiffness was taken to be 0.50. With this large an uncertainty, the 5% - 95% confidence bounds on stiffness are 44% to 228% of the stiffnesses listed in Table 2-4 corresponding to the capacity  $V_C$ . At shear loads beyond  $V_C$ , the wall softens substantially below the values given in this table, and this softening is accounted for in the nonlinear force-deflection model.

### 2.1.3 Shear Wall Drift Limits

Corley (Reference 11) reports on the drift capacity of a large number of shear walls subjected to cyclic load. Using data only for walls whose capacity is governed by shear, the data reported in Reference 11 would suggest that the 95% - 5% confidence bounds on the drift capacity of shear walls at the onset of significant strength degradation ranges from about 1% to 3% of the wall height. Drift capacity of walls governed by flexure would be even higher.



Ferritto (Reference 12) performed an extensive study of various types of three-story concrete structures subjected to the 1971 San Fernando earthquake. Defining Damage Ratio as the ratio of repair cost to replacement cost, Reference 12 presents an estimate of Damage Ratio versus Drift Ratio (drift to wall height) for shear wall structures. A Damage Ratio of 1.0 (essentially collapse) is reported to correspond to Drift Ratios of 7% and greater. However, a Damage Ratio of 0.30 is judged by the authors to correspond to the onset of significant strength degradation capable of severely damaging those structures if the ground motion had lasted longer. A Damage Ratio of 0.30 was reported to correspond to Drift Ratios of 1% to 2% for shear walls. Equally important, at a Drift Ratio of 0.5%, the reported Damage Ratio was only 0.05 which would correspond to very limited wall damage.

The Reference 11 data and the Reference 12 data to some extent are for shear walls with considerably greater height to length ratios than the walls of interest herein and thus may be too optimistic for the low rise Turbine Building walls. A limited amount of good quality data also exists for low rise shear walls whose failure is governed by shear. However, because of model size limitations, these data are likely to be too pessimistic for the thick, full scale Turbine Building walls. Estimated mean, coefficients of variation (COV) and approximate 95%



exceedance limits are presented for the onset of significant strength degradation from these limited data:

SOURCE	MEAN	COV	95% LIMIT
Barda (Ref. 7)	0.62%	0.16	0.48%
Shiga (Ref. 13)	0.55%	0.31	0.33%
LANL (Ref. 14)	0.54%	0.11	0.45%

Considering all of these data together with their limitation, the following was taken to represent the estimated median drift limit and associated logarithmic standard deviation,  $\sigma$ , corresponding to the onset of significant strength degradation of Walls 19 and 31:

$$\begin{aligned}
 \text{Median Drift Limit, } D &= 0.7\% \\
 \text{Randomness Variability, } \sigma_R &= 0.15 && (2-5) \\
 \text{Uncertainty Variability, } \sigma_U &= 0.30 \\
 \text{Composite Variability, } \sigma_C &= 0.335
 \end{aligned}$$



These estimates result in the following:

SEVERE DISTRESS PROBABILITY	DRIFT LIMIT (% OF WALL HEIGHT)	
	50% CONFIDENCE	95% - 5% CONF. BOUND
50%	0.70	0.43 - 1.15
16%	0.60	0.37 - 0.99
5%	0.55	0.33 - 0.90

When treated on a composite basis (using  $\beta_c$ ), there is about a 16% probability of severe distress at 0.5% drift and about an 84% probability at 1.0% drift. These estimates might be more conservative than necessary, but appear reasonable.

Both Walls 19 and 31 were segmented into three elements up their height because of changing capacities and stiffnesses. With the shear capacities listed in Table 2-3, drift percentages tend to be greatest within the lower element of Wall 19 or within the lower or upper elements of Wall 31. It was conservatively decided to limit the element having the greatest drift percentage to the limits specified by Equation 2-5. Thus, the probability of severe distress was based upon the shear element with the largest drift percentage obtained as a percent of the element height, such that the limit criterion was essentially treated as



an element drift criterion. The total drift of either Wall 19 or 31 was less than the maximum element drift percentage times the total wall height of 55 feet (often substantially less). Thus, the above drift criterion was used in a more conservative manner than if it had been applied over the entire wall height.

#### 2.1.4 Force-Deflection Relationship For Shear Drift

Reinforced concrete walls resist shear through various mechanisms. Initially, the wall is elastic and shear resistance is developed according to elastic beam theory. Inclined shear cracks develop when the principal tensile stresses exceed the concrete tensile strength. Once shear cracks open, the shear force is resisted mainly by the reinforcing bars and aggregate interlock. Other mechanisms such as dowel action, truss action, and the flexural compression zone also contribute to the shear resistance. The opening and closing of cracks under load reversals causes a pinching behavior to be noted in the hysteresis loops. Also, as shear cracks open wider and damage to the concrete increases, the contribution of concrete, through aggregate interlock, to shear resistance decreases. This effect causes strength degradation under large displacement cycles. A typical shear force-shear distortion diagram obtained during a structural wall test is shown in Figure 2-5 which illustrates the reverse cycle loading behavior



characterized by stiffness degradation and pinching of the hysteresis loops. Relatively few reversing load tests of low-rise walls have been reported. Fiorato and Corley (Reference 15) have summarized the laboratory testing conducted on low-rise walls with typical reinforcement ratios in the range of 0.25 to 0.5%, which are more typical of commercial building construction as reported in References 7, 8, 9, 16, 17, and 18. Much of the structural wall testing conducted at the University of California, Berkeley, summarized by Bertero (Reference 20) and Popov (Reference 21), provides useful information on the behavior of low-rise wall segments. Cyclic load testing of low-rise box structures with reinforcement ratios in the range of 0.6 to 1.6% has been limited to model structures and conducted primarily in Japan (References 22 through 25) and by the Los Alamos National Laboratory for the U.S. NRC (Reference 14 and others).

Considering these test data, Kennedy (Reference 4) has suggested that the primary or envelope loading curve for inelastic shear elements representing the shear flexibility of low-rise reinforced concrete walls can be defined by a bilinear approximation of the deformation behavior of low aspect ratio walls under monotonically increasing load. The consideration of a bilinear curve consisting of two linear segments is based on the work by Umemura (References 22 and 23) interpreted in terms of the Arakawa formula for shear strength of reinforced concrete



members. The slope of the first segment represents the effective "elastic" shear stiffness of the concrete wall section, while the slope of the second segment represents the effective stiffness of the reinforcing steel after cracking has occurred.

The hysteresis behavior for the shear element is defined by a set of ten rules. These rules are described below, and they are also shown by their corresponding numbers in Figure 2-6.

- Rule 1: The shear deformation curve, defined by a linear stiffness,  $K$  is elastic up to the yield shear force,  $V_y$ .
- Rule 2: Once the yield point in any direction is exceeded, loading continues on the second slope defined by a softer linear stiffness parameter,  $sK$ .
- Rule 3: Unloading is initiated when the direction of loading changes. A degrading unloading stiffness feature, as shown in Figure 2-7, is built into the model. Therefore, if the system unloads from Rule 2, instead of unloading parallel to the elastic stiffness,  $K$ , to a recovery point such as  $\delta_r^1$ , unloading is towards a new recovery point,  $\delta_r$ , such that



$$\delta_r = (1-\alpha)\delta_r^i \quad (2-6)$$

where  $\alpha$  is the unloading stiffness parameter. The reduced unloading slope is used for subsequent unloading as long as the maximum deformation is not exceeded. If the recovery point,  $\delta_r$ , is reached, loading in the opposite direction is according to Rule 4. Reloading from this part is according to Rule 8.

Rule 4: Once the unloading is finished, the system would initially exhibit a low stiffness in the opposite direction. This is a typical pinching behavior which is observed in shear wall tests. The pinched behavior is due to opening and closing of cracks under cyclic loads. Loading stiffness for this point is assumed to be the same as the second slope of the primary curve,  $s_k$ . Once zero deformation is reached, loading will be according to Rule 7. Unloading from this part is according to Rule 5.

Rule 5: Unloading from Rule 4 is parallel to the unloading (Rule 3) slope on the same deformation side. Once zero shear force is reached, loading in the opposite direction is according to Rule 8. If the direction of loading changes, loading is according to Rule 6.



Rule 6: If the direction of loading changes while in Rule 5, loading will be on the same line until the point where unloading was initiated is reached (Point A in Figure 2-6). Loading is according to Rule 4 thereafter. On the other hand, unloading from this part is according to Rule 5.

Rule 7: Once the cracks are closed ( $\delta = 0$  in Rule 4), loading begins toward the previous point of maximum deformation. In addition, a stiffness degrading feature, as shown in Figure 2-7b, is built into the model. Thus, instead of loading towards the previous point of maximum drift (Point  $\bar{A}$  in Figure 2-7b), a new target point such as  $\bar{B}$  is defined such that

$$\delta_{\bar{B}} = \delta_{\bar{A}}/\gamma \quad (2-7)$$

where  $\gamma$  is the stiffness degradation parameter. Once point  $\bar{B}$  is reached, loading starts on the second slope again (Rule 2). Unloading from this part is according to Rule 3.



Rule 8: This rule assures that any loading from Rule 3 will be towards the previous intermediate point (Points B and C in Figure 2-6). Once this point is reached, loading is according to Rule 7 (Point C in Figure 2-6). However, for a point such as B, loading from Rule 8 is on the second slope (Rule 2). Unloading from this part is according to Rule 9.

Rule 9: Unloading from Rule 8 is parallel to the last minimum unloading slope (Rule 3). Once unloading is finished, loading in the other direction is according to Rule 4. A change of direction in load would cause the system to follow Rule 10.

Rule 10: Loading from Rule 9 is on the same slope until the previous intermediate point (Point D in Figure 2-6) is reached. Loading is according to Rule 8 thereafter. Unloading from this part is according to Rule 9. The small amplitude or shakedown behavior of the shear hysteresis model is shown in Figure 2-7c.

The 10 Rule hysteretic model defined above is based on quasistatic cyclic load tests of shear wall elements representative of nuclear plant box-type reinforced concrete structures. The model is similar to the



shear models used by Banon (Reference 26) and Saiidi (Reference 27). Except for shear pinching and strength degradation, the model is very similar to the modified Takeda model (Reference 28) built into Computer Program DRAIN-2D for use to represent the hysteretic behavior of reinforced concrete in flexure. Comparison of the model behavior with available cyclic load test data indicates that the model provides good agreement with test results when large displacement cycles are considered up to displacements associated with the onset of substantial strength degradation. The shakedown behavior (i.e., behavior after peak deformation is reached as shown in Figure 2-7c) used in this model is unverified because of insufficient experimental data on cyclic behavior after peak response is reached. However, proper modeling of this shakedown behavior is unimportant so long as a peak drift criteria is used as the measure of damage. The proper modeling of this shakedown behavior would be very important if a total hysteretic energy absorption criterion had been used as the measure of damage. The lack of experimental data on shakedown behavior is one of the primary drawbacks to the use of a total hysteretic energy absorption criteria as a measure of damage.

Once the overall shear force-deformation model was established, it was necessary to estimate the parameters to use in this model. Figure 2-8 shows the envelope loading curve which would be expected for the lower



segment of Wall 31 based upon the strength, stiffness, and drift estimates described in Subsections 2.1.1 through 2.1.3, respectively. Also shown is the chosen bilinear representation of this expected curve. This bilinear representation is a compromise of competing objectives. The yield point,  $V_y$ , on this bilinear representation was chosen to correspond to the shear capacity of the concrete only,  $V_c$ , while the second slope factor,  $s$ , was set at 0.03.

This bilinear representation conservatively underpredicts the expected shear force at drifts less than about 0.45% and overpredicts the expected shear force at 0.7% drift by about 14%. It does maintain the total area under the expected force-drift diagram out to 0.7% drift. The loading diagram would have been better fit if the effective yield point,  $V_y$ , had been set midway between  $V_c$  and  $V_u$  with a lesser secondary slope value. However, it should also be noted that  $s$  also defines the slope of the pinching behavior after unloading (see Rule 4 of the 10 rule hysteretic model) and an  $s$  of 0.03 is already rather low for this pinched behavior. The maximum drift is reached after several strong nonlinear response cycles for strong ground motion from magnitude 6.5 and greater earthquakes (see Reference 4) and is influenced by the hysteretic energy absorbed in the pinched hysteretic loops. Use of an  $s$  value less than 0.03 would have significantly reduced the hysteretic energy absorbed in these pinched hysteretic loops. Furthermore,



Reference 4 shows that the maximum drift reached for a given ground motion level is rather insensitive to the second slope,  $s$ . It is judged that the conservatism introduced by setting  $V_y$  equal to  $V_c$  more than compensates for the 14% overshoot of the ultimate capacity,  $V_u$ , at a drift of 0.7%. Lastly, it is judged that uncertainties introduced by choosing this model are encompassed within the previously defined variabilities for strength, stiffness, and drift limits corresponding to the onset of severe damage.

For all of the wall elements, the yield capacity  $V_y$  was set equal to  $V_c$  and  $s = 0.03$  was used. The above discussion applies equally to all of these elements. The remaining hysteretic rule parameters were set at:

Unloading stiffness parameter,  $\alpha = 0.35$

Stiffness degradation parameter,  $\gamma = 0.95$

These same parameter values have previously been used in References 4 and 5 for similar shear wall evaluations. Reference 4 has shown that the maximum shear drifts are not very sensitive to a reasonable range on either of these two parameters.



## 2.2 Flexural Behavior of Shear Walls

### 2.2.1 Flexural Strength

Equations to predict the overturning (in-plane) moment capacity of rectangular shear walls containing uniformly distributed vertical reinforcement are found in Reference 9. These equations were derived from the basic ultimate strength design provisions for reinforced concrete members subjected to flexure and axial loads contained in Section 10.2 of ACI 318-83. These provisions are based upon the satisfaction of force equilibrium and strain compatibility.

Equation 1 of Reference 9 can be used to predict the flexural strength of rectangular walls having uniformly distributed reinforcement. The accuracy of this equation has been verified by testing. Equation 2 of Reference 9 shown below, was presented as an adequate approximation to Equation 1.

$$M_U = 0.5 A_S f_y l_w \left( 1 + \frac{N_U}{A_S f_y} \right) \left( 1 - \frac{c}{l_w} \right) \quad (2-8)$$



where

$A_s$  = Total area of vertical reinforcement at section

$f_y$  = Yield strength of vertical reinforcement

$l_w$  = Horizontal length of wall

$c$  = Distance from extreme compressive fiber to neutral axis

$N_u$  = Axial load, positive in compression

Inspection of Equation 2-8 reveals that the overturning moment capacity of a rectangular wall can be adequately represented by lumping the total area of the uniformly distributed vertical reinforcement at midlength of the wall and applying the basic design provisions in Section 10.2 of ACI 318-83.

$$M_u = (A_s f_y + N_u) \left( \frac{l_w}{2} - \frac{\beta_1 c}{2} \right) \quad (2-9)$$

where  $\beta_1$  is the ratio of the depth of the equivalent rectangular concrete stress block to the distance to the neutral axis,  $c$ .



This approach was typically used to predict the median flexural strength for walls without concentrated reinforcement. Concentrated reinforcement can be embedded steel columns well tied to the concrete wall or the vertical wall reinforcement bars within the effective flanges of the cross walls cast integrally with the wall evaluated. The compression flange steel is typically neglected since it is near the neutral axis, and its effect on the moment capacity is small. The total moment capacity of reinforced concrete shear walls including concentrated reinforcement is then:

$$M_U = (A_s f_y + N_U) \left( \frac{l_w}{2} - \frac{B_1 C}{2} \right) + \sum A_f f_{fy} \left( d - \frac{B_1 C}{2} \right) \quad (2-10)$$

where

$A_f$  = Area of concentrated reinforcement steel

$f_{fy}$  = Yield stress of concentrated reinforcement steel

$d$  = Distance from the extreme compressive fiber to the centroid of concentrated reinforcement steel

As an example the lower segment of Wall 31 is analyzed here for flexure. Additional resistance contributed by the dead weight of the



wall and the embedded steel columns is more significant to the flexural strength than to the shear strength. However, the column contribution at the lower story is limited by the yield strength of the column anchor bolts which is 240 kips per column. The effect of vertical ground acceleration is included in the analysis. In the following, the concrete compression strength is taken as 6.6 ksi and the steel yield strength is 66 ksi.

$$A_s = 207.8 \text{ in}^2$$

$$A_s f_y = 207.8 \times 66 = 13,720 \text{ kips}$$

$$A_f f_y = 240 \text{ kips per column (limited by anchor bolts)}$$

$$e_w = 137'$$

$$N_u = 2260 \text{ kips (compression)}$$

$$b_1 c = \frac{13720 + 240 \times 5 + 2260 [1 - 0.4 (5/6 A)]}{0.85 \times 6.6 \times 24}$$

$$= 127.6 - 5.6 A, \text{ inches}$$

$$= 10.6 - 0.47 A, \text{ feet}$$



where  $0.4 (5/6 A)$  accounts for concurrent upward ground acceleration for structures with vertical frequencies in the rigid range.

$$\begin{aligned}
 M_U = & 13720 \left( \frac{137}{2} - \frac{10.6 - 0.47 A}{2} \right) + \\
 & 240 \left( 23.92 - \frac{10.6 - 0.47 A}{2} \right) + \\
 & 240 \left( 38.92 - \frac{10.6 - 0.47 A}{2} \right) + \\
 & 240 \left( 57.42 - \frac{10.6 - 0.47 A}{2} \right) + \\
 & 240 \left( 81.69 - \frac{10.6 - 0.47 A}{2} \right) + \\
 & 240 \left( 108.23 - \frac{10.6 - 0.47 A}{2} \right) + \\
 & 2260 [1 - 0.4 (5/6 A)] \left( \frac{137}{2} - \frac{10.6 - 0.47 A}{2} \right)
 \end{aligned}$$

The influence of  $A$  is small and will be approximated. By equating  $M_U$  to the Hosgri elastic load bending moment at the wall base scaled by the ratio of  $A$  to the peak Hosgri ground acceleration level,  $1.08 \times 10^6 A$ , the  $A$  is solved to be 0.96 g. Therefore,



$$M_u = 1.04 \times 10^6 \text{ k-ft}$$

Following this same procedure the median moment capacity for each of the wall segments was computed. The effects of the embedded steel columns were included, but the contribution of these columns was limited by column splices and anchor bolts. The resultant moment capacities are shown in Table 2-3. After the wall flexural capacities were evaluated, equivalent yield shear forces were estimated by using the relative ratio of elastic computed shear and moment loads in the wall segments. These equivalent yield shear forces are also shown in Table 2-3 and may be directly compared with the shear capacities. It can be seen that flexural yielding should not occur in any of the wall segments except possibly the middle segment of Wall 19 since capacities are limited by shear for all other segments. This expectation was borne out by the nonlinear analyses results. The median yield capacities of the nonlinear flexural elements were defined by the  $M_u$  values in Table 2-3. For flexure, the logarithmic standard deviation associated with uncertainty in strength was taken to be the same as for shear, or 0.25. This assumption is conservatively larger than necessary, but had little effect on the results.



### 2.2.2 Flexural Stiffness

It was intended to estimate the flexural drift,  $\delta_{f_i}$ , and rotation,  $\alpha_i$ , at the top of each shear wall segment  $i$  from:

$$\delta_{f_i} = \frac{V_i h_{w_i}^3}{3EI_i F_{SF}} + \frac{M_i h_{w_i}^2}{2EI_i F_{SF}} + \delta_{i-1} + \alpha_{i-1} h_{w_i}$$

(2-11)

$$\alpha_i = \frac{V_i h_{w_i}^2}{2EI_i F_{SF}} + \frac{M_i h_{w_i}}{EI_i F_{SF}} + \alpha_{i-1}$$

where  $I_i$  is the uncracked moment of inertia,  $E$  is the modulus of elasticity,  $F_{SF}$  is the flexural stiffness reduction factor to account for the effect of wall cracking,  $h_{w_i}$  is the wall segment height, and  $(i-1)$  represents the top of the segment below. For estimating  $I$ , no credit was taken for end flanges and the effects of major cutouts was included. The modulus of elasticity was taken as  $E = 6.67 \times 10^5$  KSF.

However, during review of the results, it was found that the analyst had used for flexural drift:

$$\delta_{f_i} = \frac{V_i h_{w_i}^3}{6EI_i} + \delta_{i-1} \quad (2-12)$$



which overstates the flexural stiffness since the first term (shear term) in Equation 2-11 is two to four times as stiff as it should be (based on  $F_{SF}$  ranging from 1.0 to 0.5) while the second term (moment term) and fourth term (rotational term) are ignored. The resulting median flexural stiffnesses for each wall segment using Equation 2-12 are tabulated in Table 2-4.

The net result of using Equation 2-12 is that computed flexural drifts were negligible compared to shear drifts in that the flexural stiffnesses used for Wall 19 were twenty to sixty times the shear stiffnesses, and were one hundred to three hundred times the shear stiffnesses for Wall 31.

For walls with height to length ratios less than 0.5 (such as Walls 19 and 31), it is common practice to ignore flexural flexibility and base flexibility only on shear flexibility. Use of the erroneous flexural stiffnesses obtained from Equation 2-12 and listed in Table 2-4 is equivalent to making this common assumption of ignoring flexural flexibility and considering only shear flexibility. However, the shear stiffnesses contained a judgementally selected stiffness knockdown factor  $F_S$  of 0.50 which should compensate for ignoring flexural flexibility.



To study the influence of inadvertently ignoring flexural flexibility, the ratio of total-drift to essentially shear-only-drift using stiffnesses tabulated in Table 2-4 was computed for Walls 19 and 31 using static horizontal application of the inertial wall weights shown in Table 2-2. The total drift properly includes flexural drift computed from Equation 2-11 with  $F_{SF}$  judgementally selected as unity. The ratios of total-drift to shear-only-drift ( $R_{T/S}$ ) are shown in Table 2-5. Then, an equivalent total-drift stiffness knockdown factor  $F_T$  to be applied to the essentially shear-only-drift results based on the Table 2-4 stiffnesses can be computed from:

$$F_T = (R_{T/S})F_S \quad (2-13)$$

where  $F_S$  is the shear stiffness knockdown factor of 0.50. These equivalent total-drift stiffness knockdown factors,  $F_T$ , are also shown in Table 2-5. The net result of using Equation 2-12 for flexural drift (i.e., essentially ignoring flexural drift) is equivalent to using the equivalent total-drift stiffness knockdown factors in Table 2-5 in lieu of an  $F_S$  value of 0.5. Since all of the  $F_T$  values in Table 2-5 are well within the uncertainty range of stiffness knockdown factors due to concrete cracking, and since a large logarithmic standard deviation of 0.50 was included in this study to account for shear stiffness



uncertainty, it was concluded that stiffness errors introduced by the use of the erroneous Equation 2-12 were small and easily tolerable when compared to the stiffness uncertainty variation already included in this study. A logarithmic standard deviation of 0.50 was also used for the uncertainty associated with flexural stiffness.

### 2.2.3 Flexural Drift Limits

Nonlinear flexural drifts are small in each of the wall segments compared to the maximum shear drift. Also, flexural drift capacities are larger than shear drift capacities. Therefore, no drift limits were developed or specified for flexural drifts.

### 2.2.4 Force-Deflection Relationship For Flexural Drift

The nonlinear force-deflection hysteretic behavior for flexural drift was approximated using a modified Takeda model. The standard Takeda model built into DRAIN-2D (Reference 28) is shown in Figure 2-9. This standard Takeda model is very similar to the shear deformation hysteretic model shown in Figure 2-6 except that it does not contain pinching behavior, reduced unloading stiffness behavior, or stiffness reduction behavior upon reloading. Thus, the standard Takeda model absorbs considerably more hysteretic energy per nonlinear cycle than



does the shear model of Figure 2-6, and it does not ratchet towards increased drifts with each nonlinear cycle. For flexural drifts of shear walls, the standard Takeda model was modified to incorporate a reduced unloading stiffness defined by  $\alpha = 0.35$  which is the same value as previously defined for shear drifts. However, no pinching behavior or loading stiffness reduction was incorporated. It was judged that this modified Takeda model provided a good nonlinear hysteretic behavior representation for flexural drifts. It was used for all flexural shear wall elements, the operating floor beam elements, and the turbine pedestal element.

For the shear wall flexural elements, the yield point was defined by the strength values in Table 2-3 and stiffness values in Table 2-4. The second slope was defined by  $s = 0.03$  to account for some work hardening effects.

### 2.3 Operating Floor Beam Elements

A monotonic or enveloping force-deflection diagram for each of the two operating floor beam elements developed by the Diablo Canyon Project Civil Group (Reference 30) is presented in Figure 2-10. This force-deflection curve was based upon their review of static nonlinear finite element cracked concrete analysis results previously obtained for the



operating floor. This diagram accounts for different degrees of concrete cracking as loadings are increased. Slightly different force-deformation curves were developed for east to west and west to east responses of the beam-like portions of the operating floor diaphragm. For the DRAIN input, the operating floor diaphragm force-deformation curve was approximated by the bilinear curve also shown in Figure 2-10 which uses the same bilinear representation for both east to west and west to east responses of the diaphragm. It should be noted that the strengths and stiffnesses defined in Figure 2-10 are applied equally to Operating Floor Elements 1, 2, 3, and 4 shown in Figure 2-3.

It can be seen in Figure 2-10 that the simplified bilinear representation fits well up to floor deformations of about 6 inches. Beyond a deformation of about 8 inches, this bilinear representation significantly overpredicts the stiffness of the operating floor. This significant overprediction of stiffness leads to an underprediction of deformation of the operating floor and an overprediction of loads distributed to the shear walls from the operating floor for deformation in excess of about 8 inches. Since the drift capacity of the operating floors is judged to be in excess of 18 inches which is not expected to be reached prior to severe distress in the shear wall, the potential underprediction of operating floor drifts is of little concern. However, the overprediction of loads transferred to the shear walls will



lead to some conservatism in the estimated probabilities of failure of the shear walls for a given ground motion.

The above discussion applies when median stiffnesses are used. However, for the probabilistic evaluation, stiffnesses are multiplied by a probabilistically defined stiffness factor. For an operating floor probabilistic stiffness factor of  $R_{O\text{STIFF}}$ , the overprediction of loads on the shear walls and underprediction of operating floor relative drifts is only significant when the operating floor relative drift,  $\Delta_o$ , does not satisfy the following:

$$\Delta_o \leq \frac{8 \text{ inches}}{R_{O\text{STIFF}}} \quad (2-14)$$

Each case where  $\Delta_o$  exceeds the limits of Equation 2-14 is specifically noted in the section where the results of the nonlinear probabilistic evaluations are reported. It will be shown that no such cases exist for the trials with average spectral acceleration ground motion of 3.0g, very few cases exist at 4.0g; therefore, the issue only becomes important with the 6.0g trials. Since the 3.0g trials were of the greatest interest and the 6.0g trials were of much lesser interest, it was decided to accept the overprediction of shear wall loads from the operating floor rather than develop a more complex nonlinear model.



The modified Takeda model described in Section 2.2.4 was used to define the nonlinear hysteretic behavior of the operating floor beam elements. The same logarithmic standard deviation values previously described for the shear walls were used to describe the uncertainty in the operating floor stiffness and strength.

#### 2.4 Turbine Pedestal

The expected enveloping force-deflection diagram shown in Figure 2-11 for the turbine pedestal was developed by the Diablo Canyon Project Civil Group (Reference 30). This diagram was simplified to the elasto-perfectly plastic approximation also shown in Figure 2-11, which provides a good fit at all drifts. The modified Takeda model described in Section 2.2.4 was used to define the nonlinear hysteretic behavior. Uncertainties in stiffness and strength of the turbine pedestal were defined by the same lognormal deviations as previously described for shear walls.

#### 2.5 Other Modelling Considerations

A 3.375-inch gap element was used to couple the turbine pedestal to each of the operating floor elements as shown in Figure 2-3. Thus, for elastic response, the turbine pedestal is uncoupled from the operating floor and shear wall model.



The elastic response of the turbine pedestal model consists of one mode with a median frequency of 3.1 Hz (based on median stiffness properties). There are three important elastic modes for the shear walls and operating floor model. Their median frequencies are shown in Table 2-6. Approximately 92% of the mass is incorporated into these three modes. The 4.0 Hz mode consists of deformation of the operating floor with the shear walls nearly stationary. The 8.6 Hz mode consists of drift of Wall 31 with both the operating floor and Wall 19 being nearly stationary. The 9.5 Hz mode consists of drift of Wall 19 with both the operating floor and Wall 31 nearly stationary.

Modal shears and moments are also presented in Table 2-6 for the turbine pedestal mode plus the three important shear wall and operating floor modes. The modal shears and moments have been premultiplied by the appropriate base input motion participation factor so that they correspond to a 1g input spectral acceleration. Lastly, Table 2-6 presents modal displacements for each of these modes defined for a 1g input spectral acceleration.

Based upon a review of the modal properties, it was judged that significant nonlinear drifts of the shear walls would be primarily



influenced by spectral accelerations in the 3 to 8.5 Hz frequency range. For this reason, it was decided to scale all ground motion records to the same average 5% damped spectral accelerations in the 3 to 8.5 Hz frequency range. Throughout the remainder of this report the symbol,  $\bar{S}_a$ , will be used to define the average 5% damped spectral acceleration over the 3 to 8.5 Hz frequency range.

For all nonlinear runs, elastic damping was probabilistically defined with a median value of 7% and an uncertainty logarithmic standard deviation of 0.35. Thus, the 95% - 5% confidence bounds on elastic damping ranged from 4% to 12.5%. Considering that some energy is radiated from the structure back into the ground, this range of elastic damping is considered to be reasonable. In the results section, it will be shown that the probabilistically selected damping value had an unobservable effect on the resultant shear wall drift or probability of failure. Shear wall drifts are much more influenced by the energy dissipated in the hysteresis loops than by the elastic damping selected.

Lastly, it was found from sensitivity studies that stable predictions of the shear wall drifts for this model could generally be obtained from the DRAIN-2D computer program when a time step size of  $\Delta t = 0.005$  seconds was used. This time step size was used for most analyses reported herein. In a few cases, particularly at  $\bar{S}_a = 6.0g$ , it was



necessary to reduce the time-step size to  $\Delta t = 0.0025$  seconds.

## 2.6 Treatment of Randomness and Uncertainty

As noted in the previous sections, strength, stiffness, damping, and drift limits were each treated as lognormally distributed random variables defined by a median value and randomness, uncertainty, and composite logarithmic standard deviations as given below:

VARIABLE	MEDIAN	LOGARITHMIC STANDARD DEVIATION		
		RANDOM	UNCERTAINTY	COMPOSITE
DAMPING	7%	0	0.35	0.35
STIFFNESS RATIO	1.0	0	0.50	0.50
STRENGTH RATIO	1.0	0	0.25	0.25
SHEAR WALL DRIFT LIMIT	0.7%	0.15	0.30	0.335

In addition, randomness of the ground motion characteristics were incorporated by using 25 different ground motion records each scaled to the same average 5% damped spectral acceleration,  $\bar{S}_a$ , in the 3 to 8.5 Hz range. The probabilistic shear wall drift limit criteria was used to predict the probability of severe distress for the drifts computed in



any given nonlinear analysis. The remaining probabilistic variables were used as defined in the remainder of this subsection.

For each value of  $\bar{S}_g$  (3.0g, 4.0g, and 6.0g), 50 nonlinear analyses were performed. For each nonlinear analysis, the median stiffnesses and strengths of the shear walls, operating floor, and turbine pedestal were multiplied by probabilistically defined stiffness and strength ratios. Stiffness and strength ratios were independently defined for each element type (shear walls, operating floors, and turbine pedestals). Thus, a given element could have a high stiffness ratio and a low strength ratio in a given nonlinear analysis. Similarly, shear walls could have a low strength ratio while the operating floor had a high strength ratio in the same analysis. However, all six shear wall elements in shear and flexure had the same stiffness and strength ratios for a given analysis. Similarly, the four operating floor elements had the same stiffness and strength ratios for given analyses. This approach was judged to provide the most realistic variation of stiffnesses and strengths throughout the model. At the same time elastic damping was considered to be an independent probabilistically defined variable.

Using the lognormal probabilistic density functions defined above, specific values of the stiffness ratio, strength ratio, and damping were



independently and randomly selected for each of the 50 nonlinear analyses. The 50 sets of independently selected properties are listed in Table 2-7.

Each of the 25 earthquake ground motion time histories described in the next section were used twice. The records were each used once in the first 25 trials and then were repeated in the same order in the next 25 trials. Thus, Record 1 was used in Trials 1 and 26; Record 10 in Trials 10 and 35; and so on. For each trial, the largest story drift (defined as a percent of height) associated with the 6 shear elements representing portions of Walls 19 or 31 was compared with the probabilistically defined shear wall drift limit for predicting the probability of severe distress from that trial. In other words, the probabilistic drift limits were treated as dependent for all 6 shear elements. This dependency was considered to be the most appropriate treatment of the drift limits.



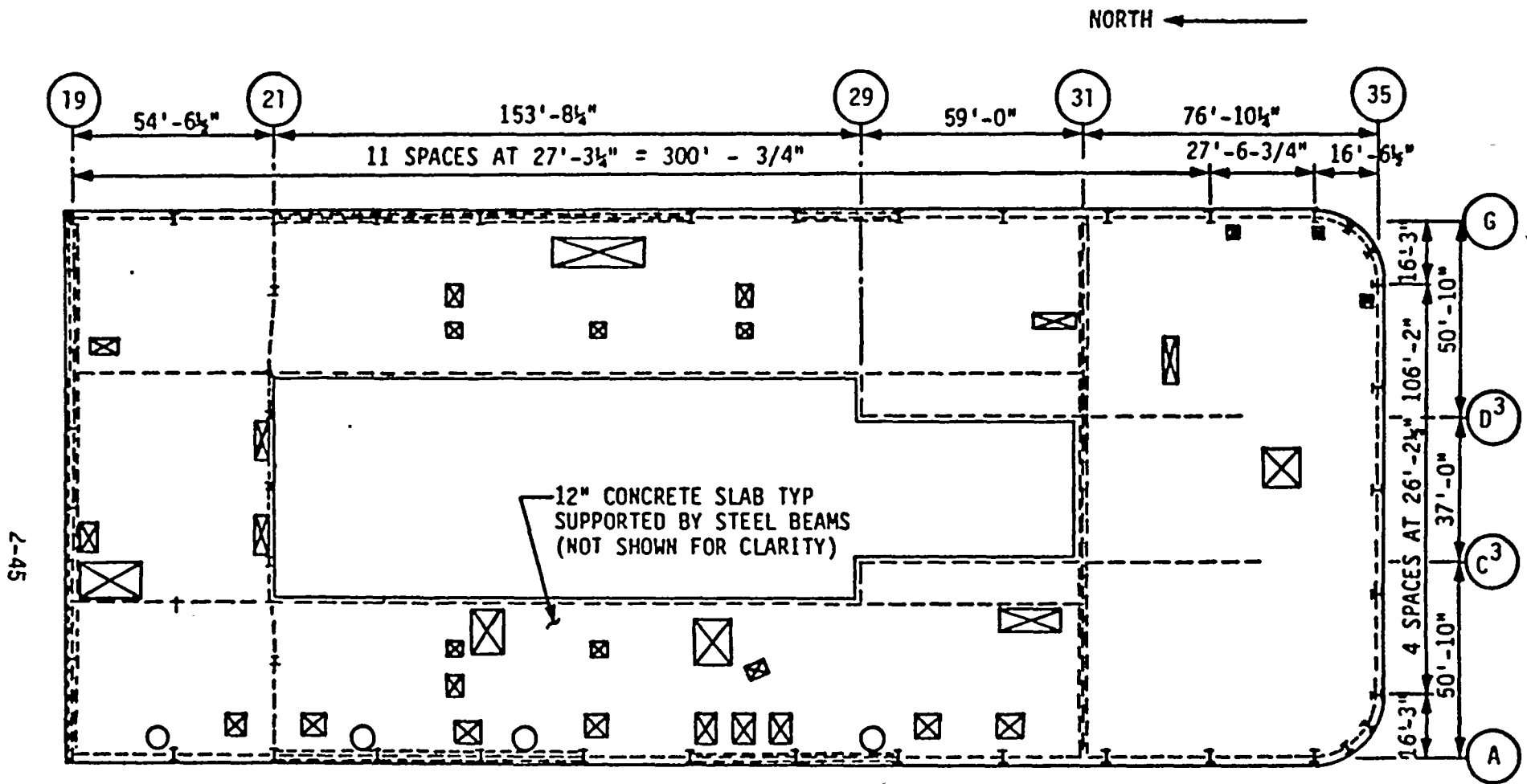


Figure 2-1. Unit 2 Turbine Building Concrete Outline (Elevation 140 Feet)



2-46

NORTH ←

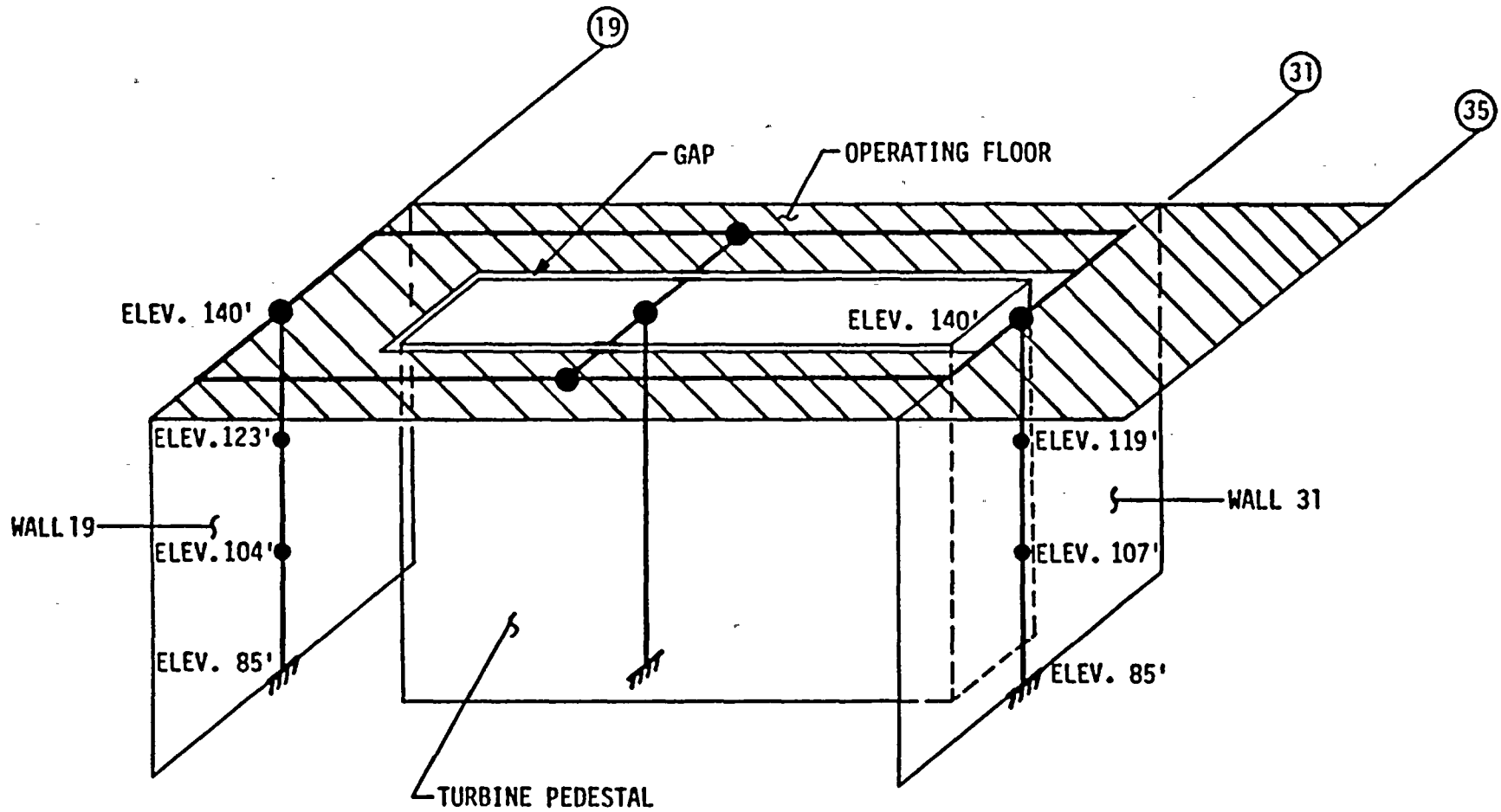
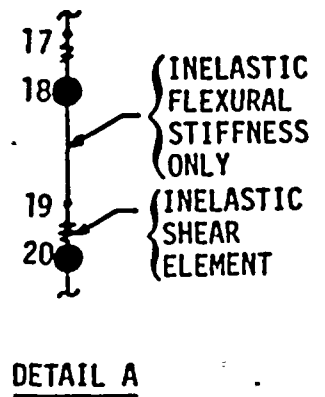
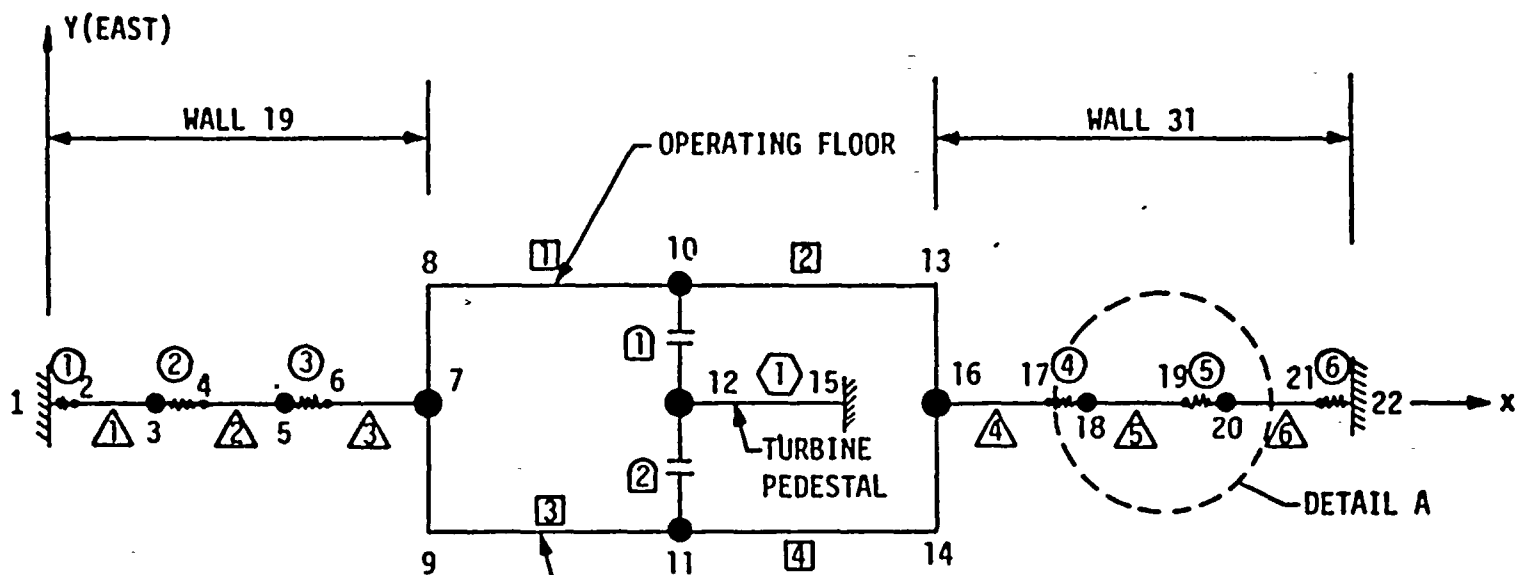


Figure 2-2. Schematic Illustration of Turbine Building Nonlinear Model





- ① - INELASTIC SHEAR ELEMENTS (SHEAR DEFORMATION ONLY)
- △ - INELASTIC FLEXURAL BEAM ELEMENT (FLEXURAL DEFORMATION ONLY)
- - OPERATING FLOOR ELEMENT
- ⬡ - TURBINE PEDESTAL
- Ⓛ - GAP ELEMENT

Figure 2-3. Diablo Canyon Turbine Building DRAIN-2D Model

2-47



2-48

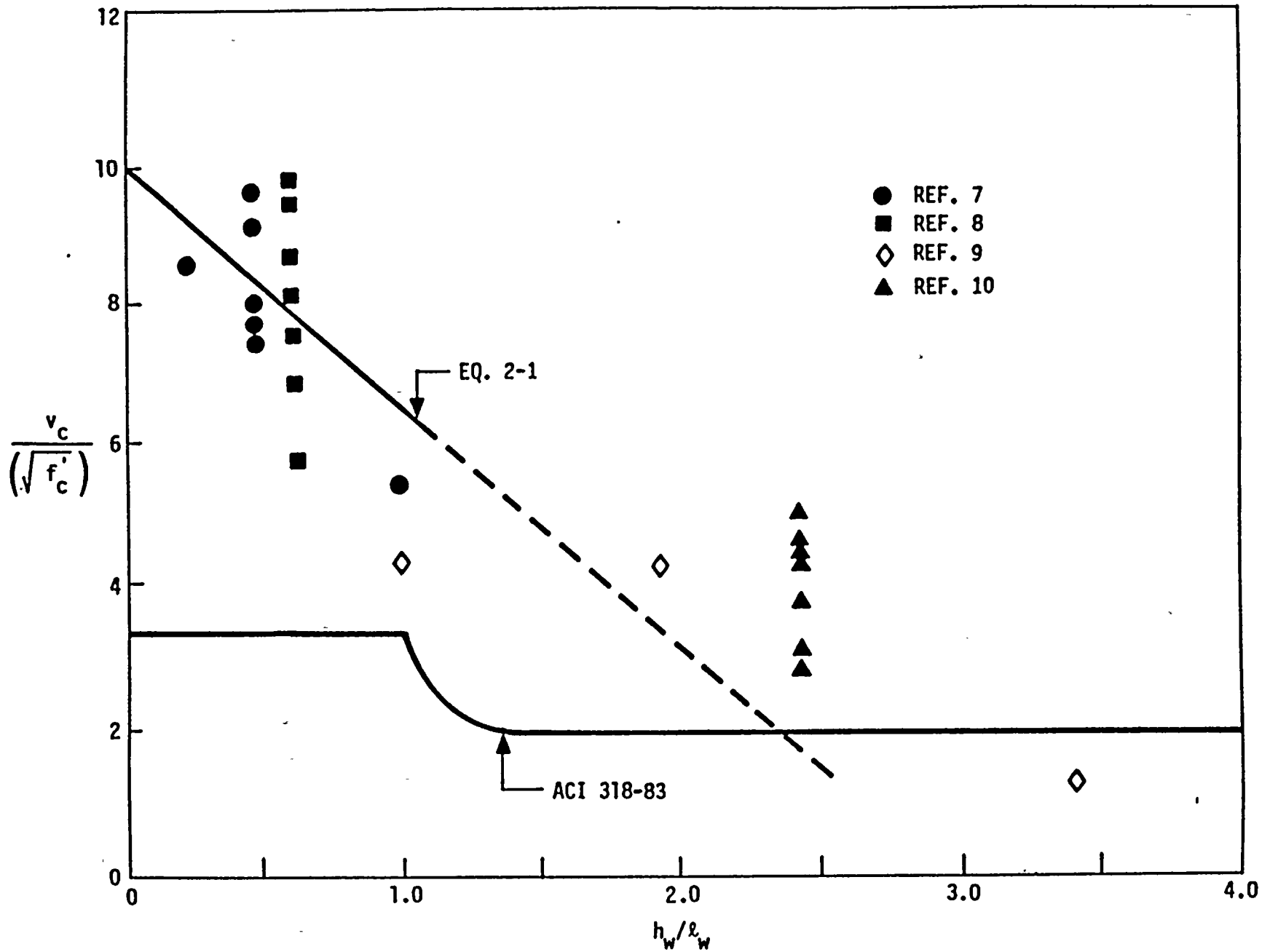
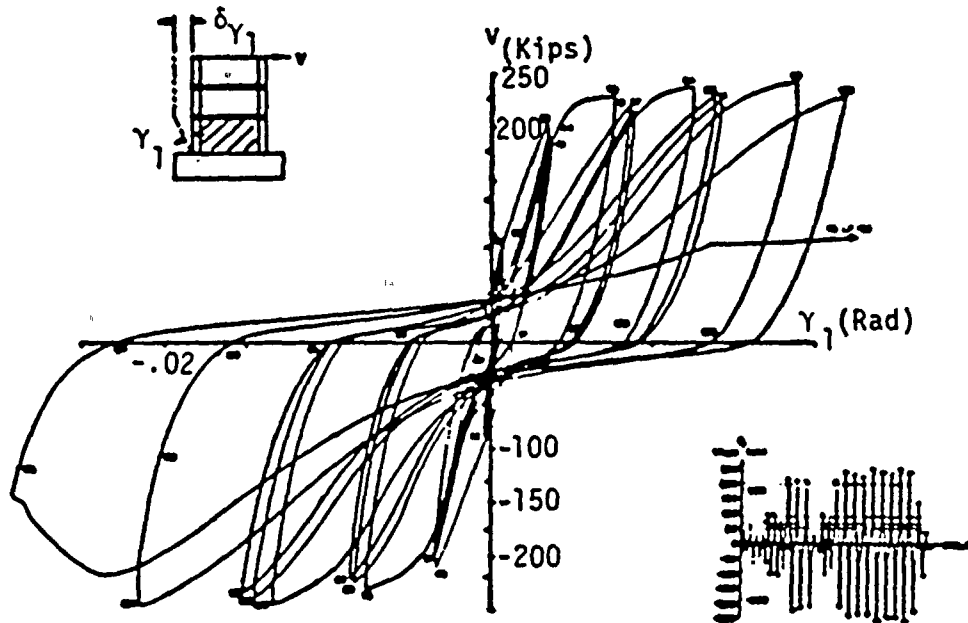


Figure 2-4. Strength of Concrete Shear Walls





SHEAR FORCE-SHEAR DISTORTION DIAGRAM FOR STRUCTURAL  
CONCRETE WALL TEST (Ref. 19)

Figure 2-5. Cyclic Load-Deflection Behavior of Concrete  
Shear Walls



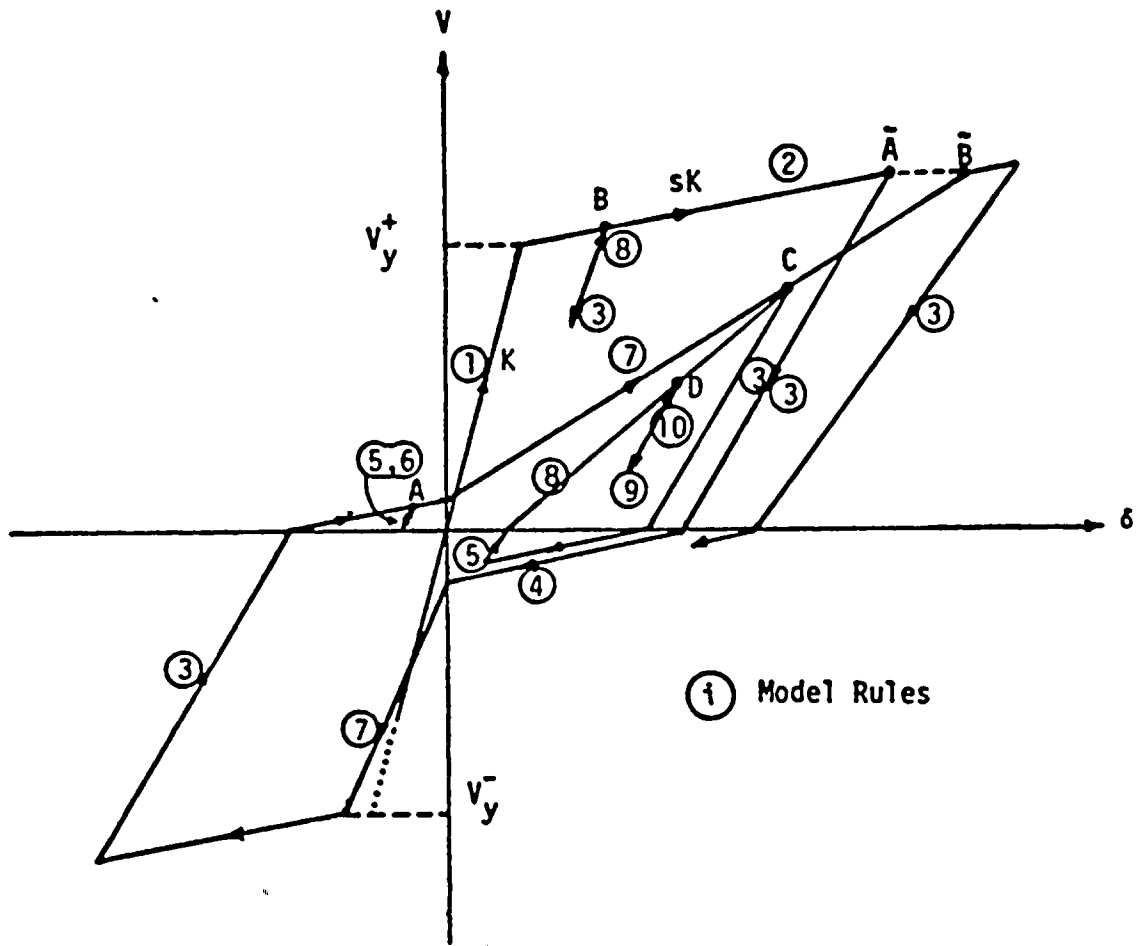
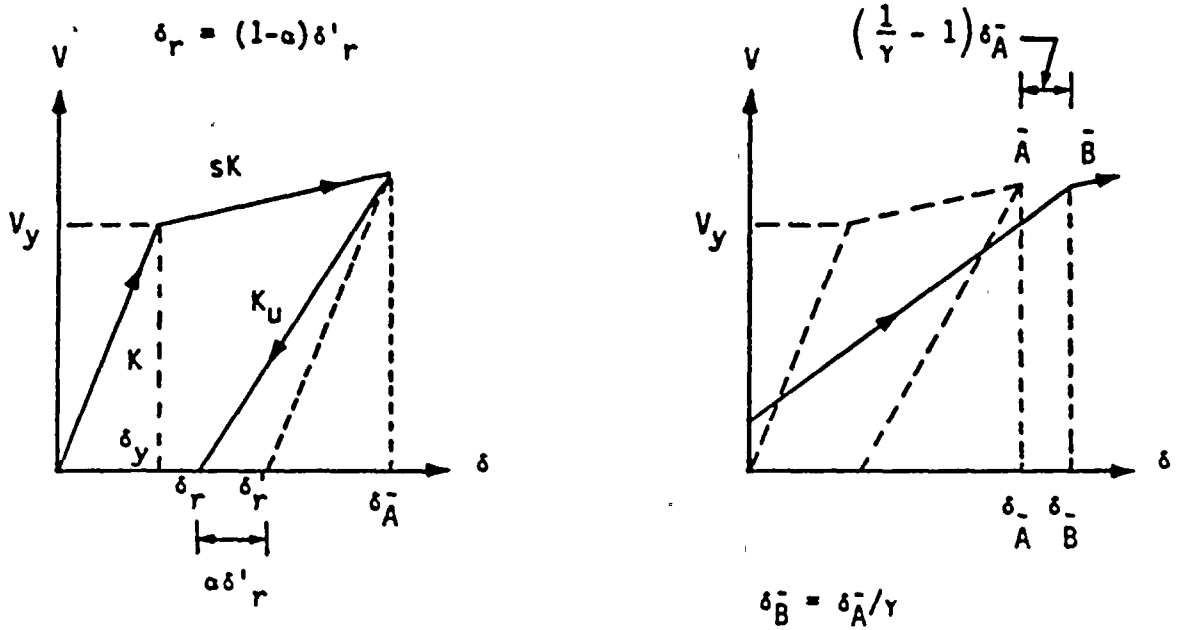


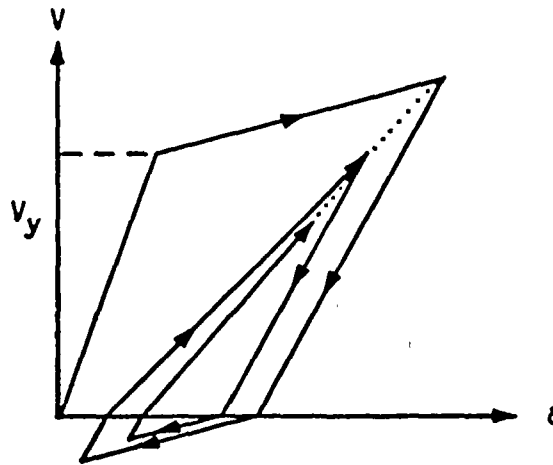
Figure 2-6. Shear Deformation Hysteretic Behavior





(a) UNLOADING STIFFNESS  
PARAMETER  $\alpha$

(b) STIFFNESS DEGRADATION  
PARAMETER  $\gamma$



(c) SHAKEDOWN BEHAVIOR

Figure 2-7. Characteristics of the Hysteresis Model and Identification of Model Parameters



2-52

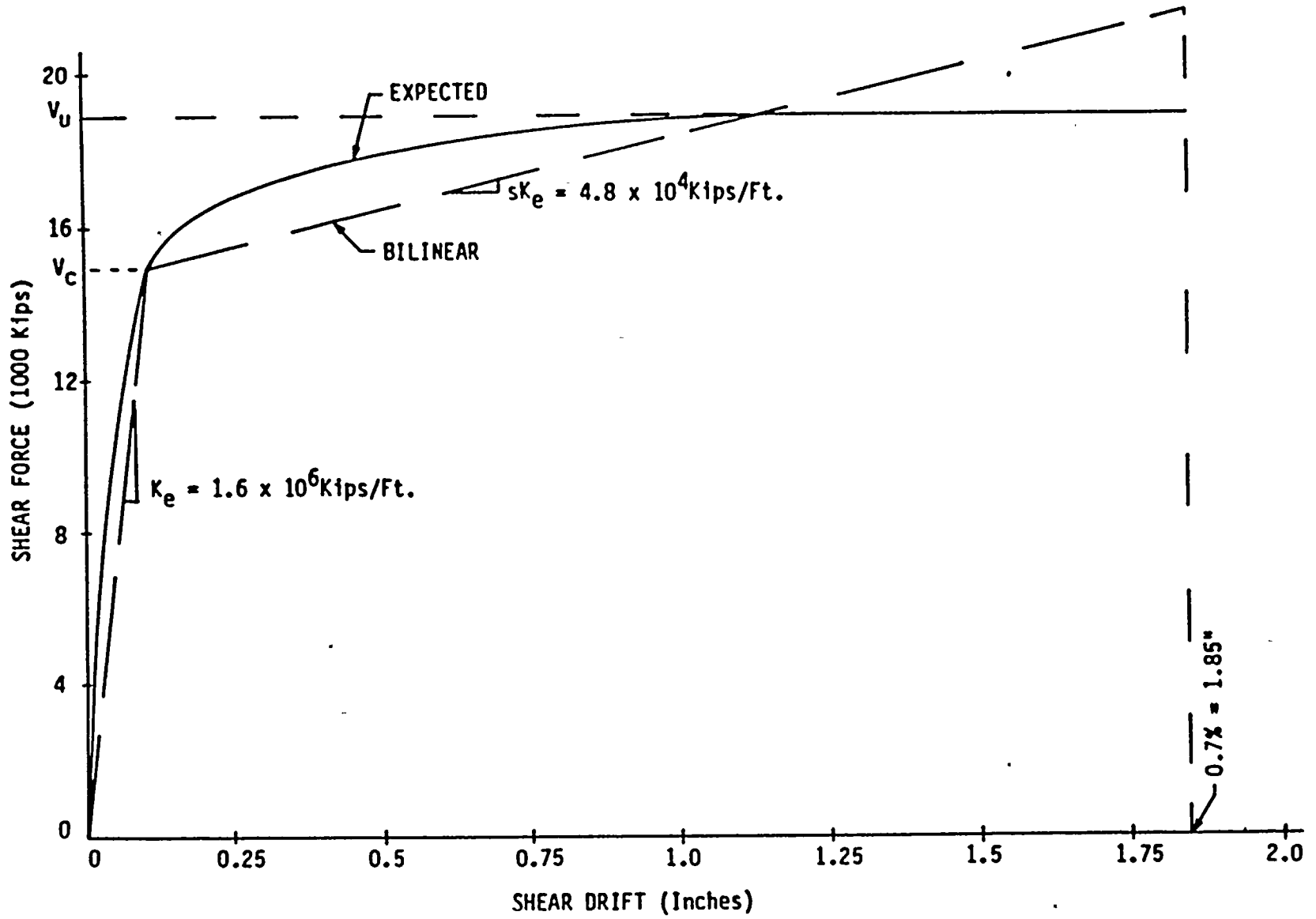


Figure 2-8. Shear Force - Drift Relationship for Lowest Element of Wall 31



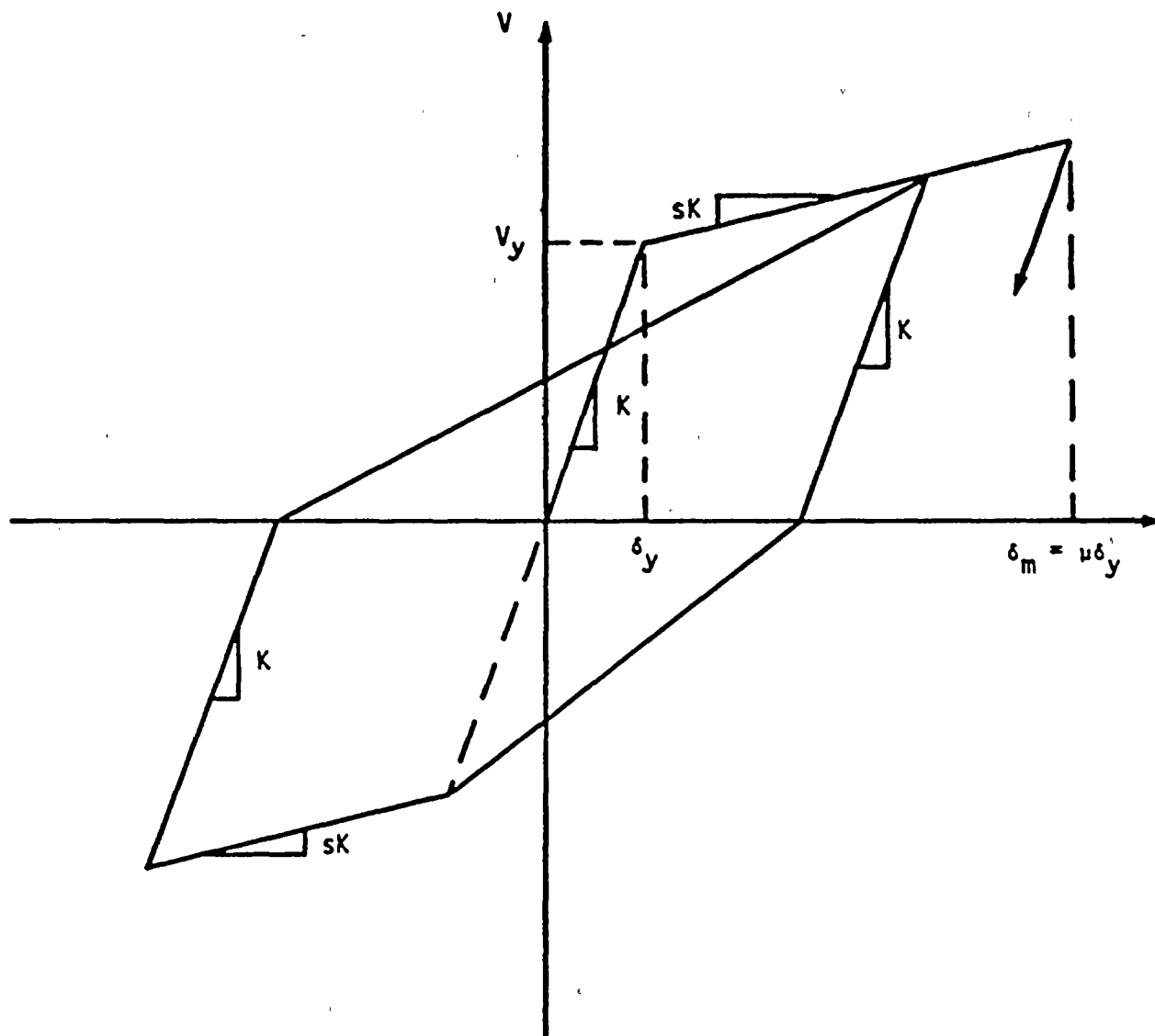


Figure 2-9. Standard Takeda Model for Flexural Deformation Hysteretic Behavior



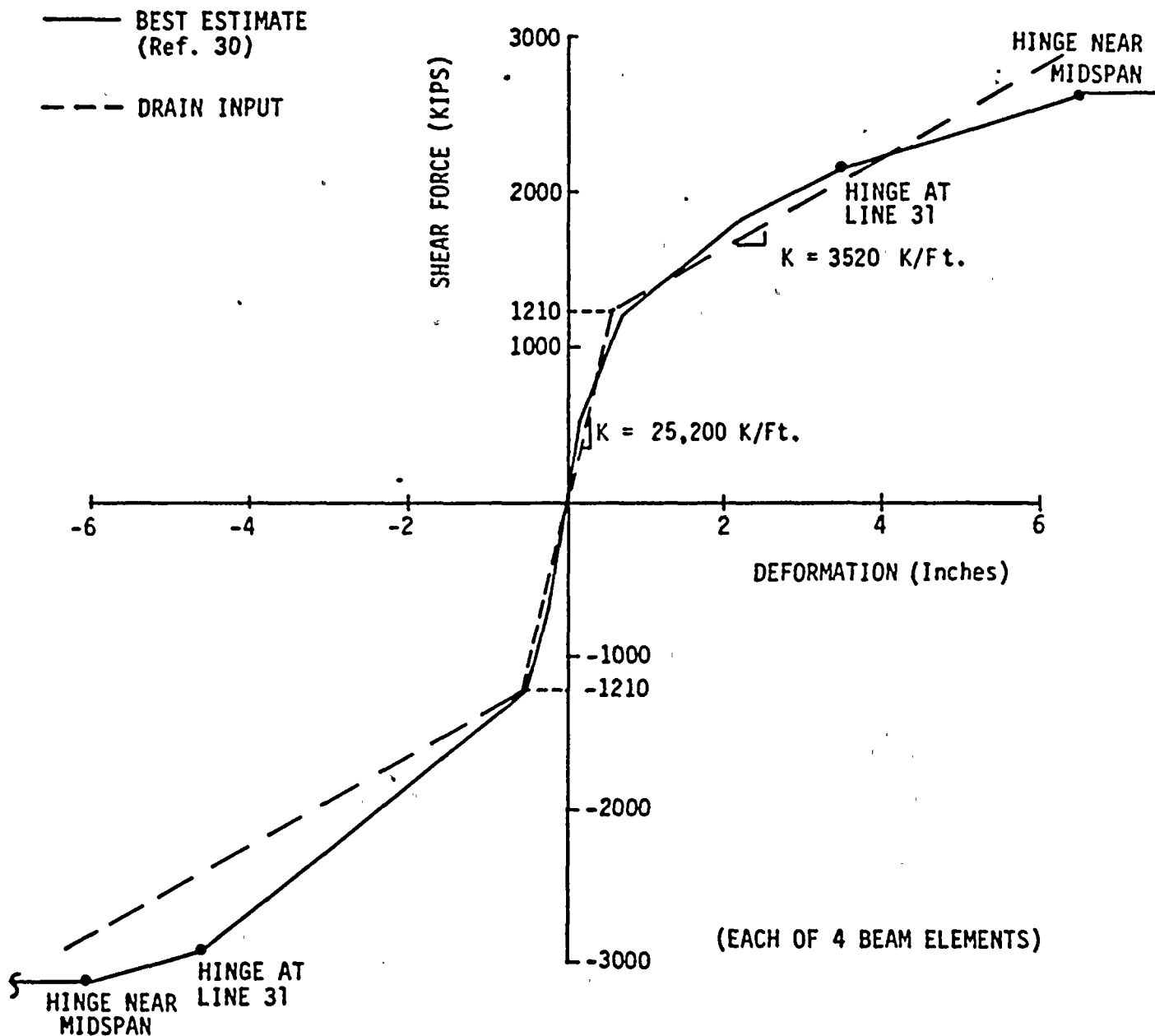


Figure 2-10: Shear-Deformation Curve for Each Beam-like Portion of the Operating Diaphragm at the Midspan



2-55

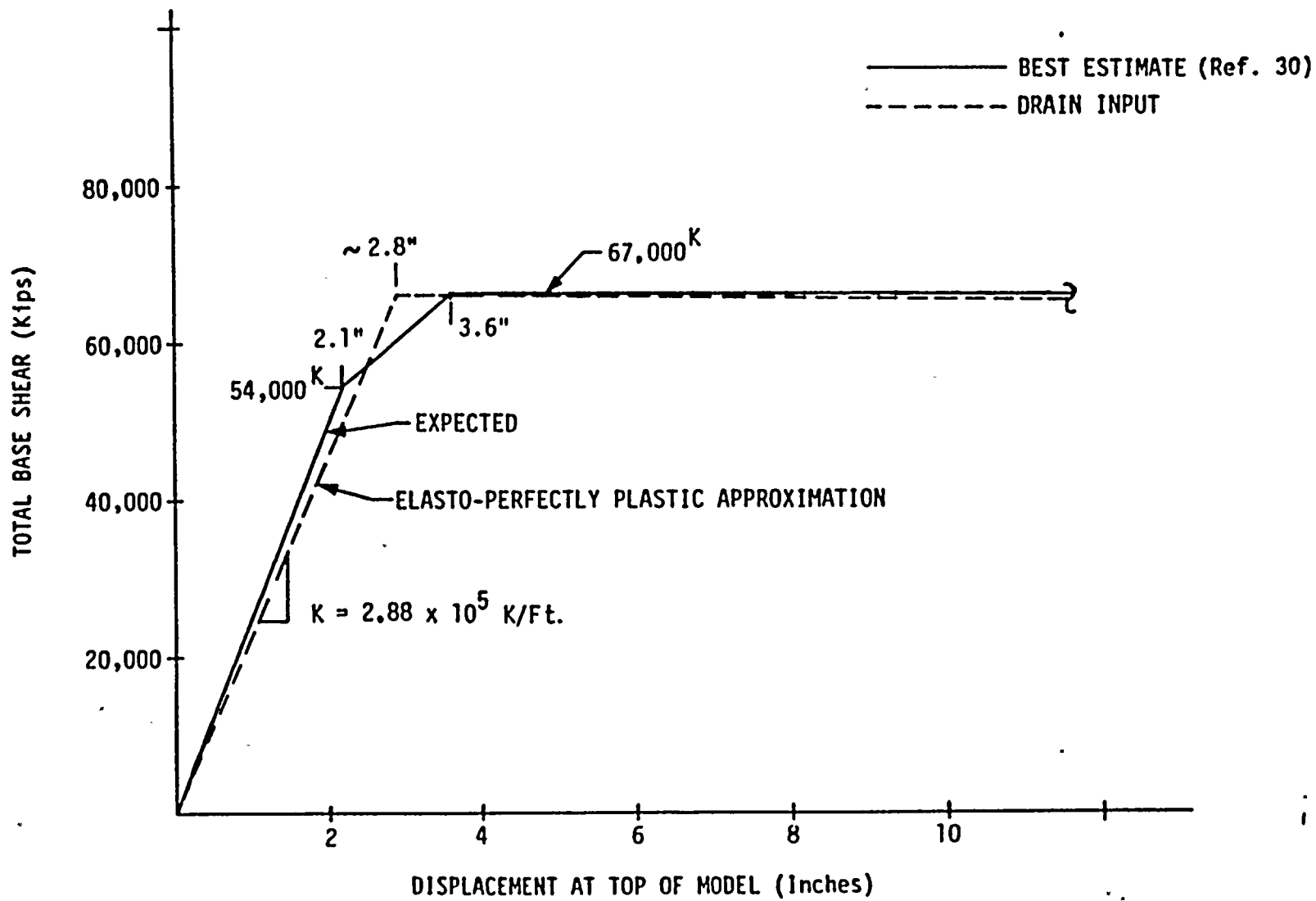


Figure 2-11. Shear-Deformation Curve for the Turbine Pedestal



Table 2-1. Turbine Building Nonlinear Model Node Coordinates

NODE NO.	X-COORDINATE (Ft.)	Y-COORDINATE (Ft.)
1	0.	0.
2	.19	0.
3	19.19	0.
4	19.38	0.
5	38.38	0.
6	38.55	0.
7	55.55	0.
8*	55.55	49.42
9*	55.55	-49.42
10	189.16	49.42
11	189.16	-49.42
12	189.16	0.
13**	322.77	49.42
14**	322.77	-49.42
15	244.16	0.
16	322.77	0.
17	343.77	0.
18	343.98	0.
19	355.98	0.
20	356.10	0.
21	378.10	0.
22	378.32	0.

\* Slaved to Node 7

\*\* Slaved to Node 16



Table 2-2. Turbine Building Nonlinear Model Nodal Masses

NODE NO.	WEIGHT (Kips)	COMMENT
3	1,573	WALL 19 AND FLOOR AT EL 104
5	832	WALL 19 AND FLOOR AT EL 123
7	4,219	WALL 19 AND OPERATING FLOOR*
10	2,250	OPERATING FLOOR*
11	2,250	OPERATING FLOOR*
12	25,000	TURBINE PEDESTAL*
16	6,331	WALL 31 AND OPERATING FLOOR*
18	2,130	WALL 31 AND FLOOR AT EL 119
20	2,460	WALL 31 AND FLOOR AT EL 107

\* Reference 30



Table 2-3. Median Capacities of Shear Wall Elements

CONCRETE SHEAR WALL	SHEAR CAPACITIES		FLEXURAL CAPACITIES	
	CONCRETE ONLY $V_C$ (Kips)	ULTIMATE $V_U$ (Kips)	YIELD MOMENT $M_U$ (Kip-Ft.)	EQUIVALENT YIELD SHEAR $V_M$ (Kips)
WALL 19				
EL 140 - EL 123	10,600	12,800	$0.23 \times 10^6$	13,700
EL 123 - EL 104	11,000	13,300	$0.39 \times 10^6$	11,200
EL 104 - EL 85	9,200	13,500	$0.71 \times 10^6$	14,100
WALL 31				
EL 140 - EL 119	13,200	16,600	$0.64 \times 10^6$	30,700
EL 119 - EL 107	17,000	21,700	$0.72 \times 10^6$	24,800
EL 107 - EL 85	15,000	19,200	$1.05 \times 10^6$	22,300



Table 2-4. Effective Shear Wall Elastic Shear and Flexural Stiffness Used

CONCRETE SHEAR WALL	EFFECTIVE SHEAR STIFFNESS (Kips/Ft.)	EFFECTIVE FLEXURAL STIFFNESS (Kips/Ft.)
WALL 19  EL 140 - EL 123  EL 123 - EL 104  EL 104 - EL 85	  $1.14 \times 10^6$  $1.22 \times 10^6$  $2.25 \times 10^6$	  $6.13 \times 10^7$  $7.55 \times 10^7$  $5.05 \times 10^7$
WALL 31  EL 140 - EL 119  EL 119 - EL 107  EL 107 - EL 85	  $1.71 \times 10^6$  $3.10 \times 10^6$  $1.60 \times 10^6$	  $24.2 \times 10^7$  $99.0 \times 10^7$  $16.0 \times 10^7$



Table 2-5. Ratio of Total Drifts to Essentially Shear-Only-Drifts  
(Based on Table 2-4 Stiffnesses) and Equivalent Total-Drift  
Stiffness Knockdown Factor

WALL	SEGMENT	RATIO TOTAL-DRIFT TO ESSENTIALLY SHEAR- ONLY-DRIFT $R_T/S$	EQUIVALENT TOTAL- DRIFT STIFFNESS KNOCK- DOWN FACTOR $F_T$
19	EL 140	1.37	0.68
	EL 123	1.32	0.66
	EL 104	1.21	0.60
31	EL 140	1.10	0.55
	EL 119	1.06	0.53
	EL 107	1.04	0.52



content capable of producing both high spectral acceleration in excess of 2.1g in the 8.6 to 9.5 Hz frequency range and high spectral accelerations in excess of Equation 5-32 in the 1.7 to 2.8 Hz frequency range. Possibly the single parameter  $\bar{S}_a$  would have performed better as a descriptor of damage potential if it had been averaged over the broader 1.7 to 9.5 Hz frequency range rather than over 3 to 8.5 Hz.



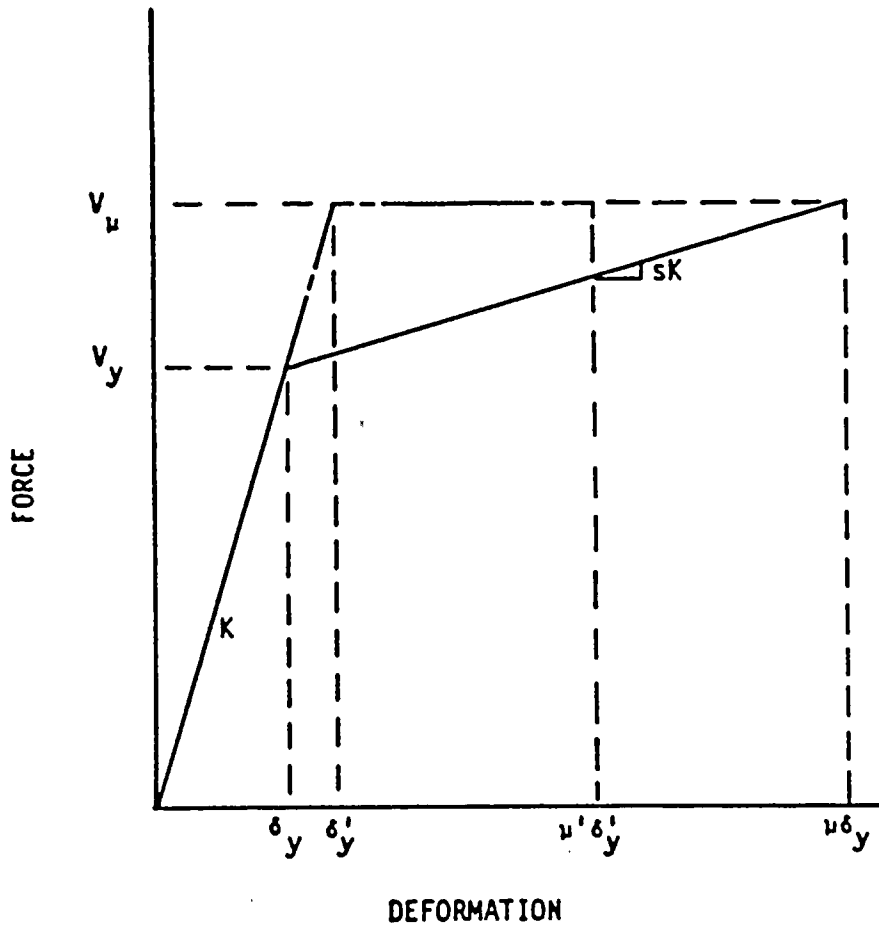


Figure 5-1. Bilinear Force - Deflection Relationship Versus Pseudo Elasto-Perfectly Plastic Relationship of Equal Area and Equal Capacity  $V_u$



5-33

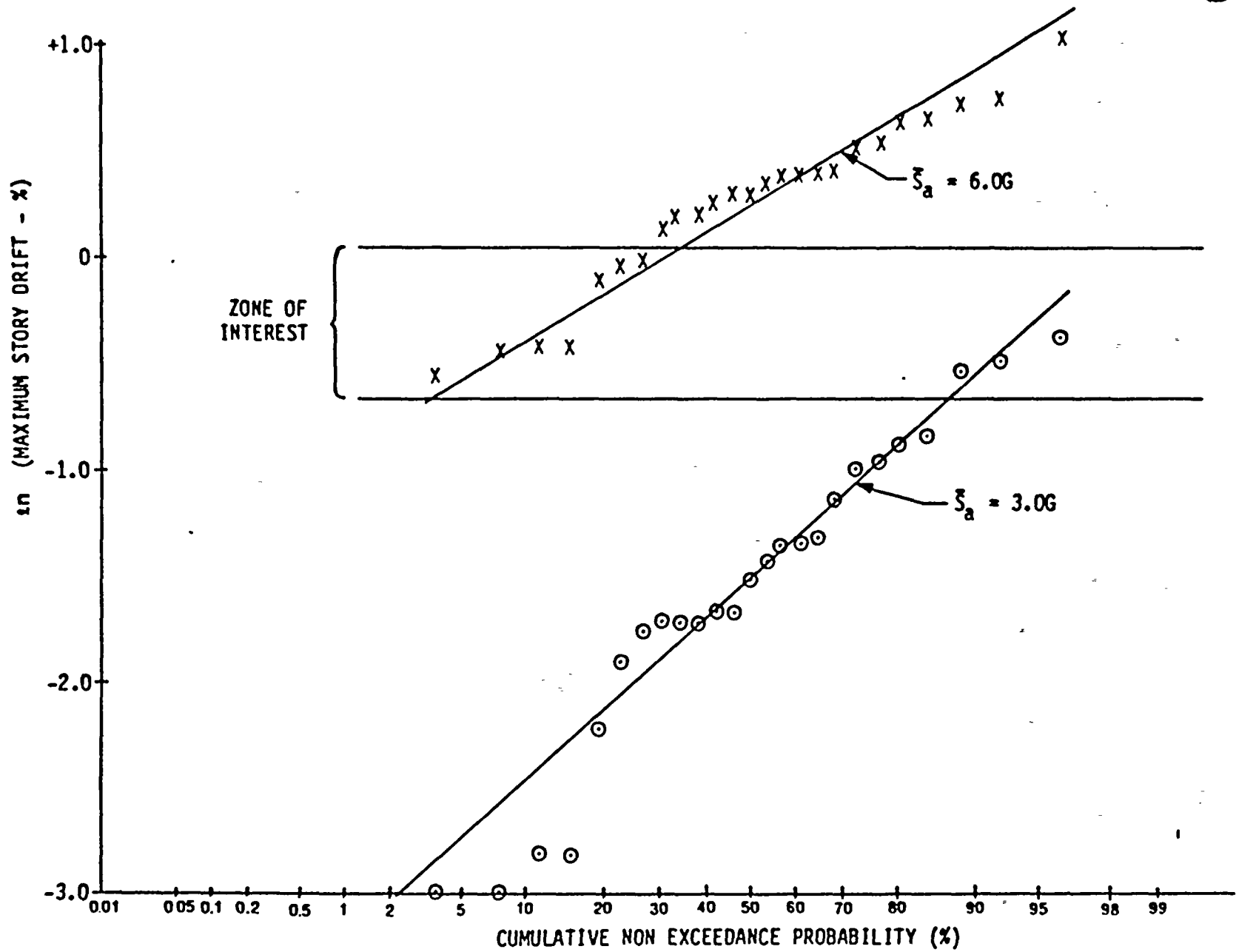


Figure 5-2. Cumulative Probability Plots of Natural Logarithm of Drifts



Table 5-1. Nonlinear Results for Median Structural Model at  $\bar{S}_a = 3.0G$ 

TRIAL NO.	WALL 19		WALL 31		OPERATING FLOOR DRIFT (Inches)	TURBINE PEDESTAL DRIFT (Inches)	PEDESTAL IMPACT CASES(1)	PROBA-BILITY OF SEVERE WALL DISTRESS(%)
	TOP DRIFT (Inches)	MAX STORY DRIFT (%)	TOP DRIFT (Inches)	MAX STORY DRIFT (%)				
1	0.58	0.18	0.60	0.18	3.06	3.22		0
2	1.01	0.35	1.30	0.42	5.15	2.47	Y	0
3	0.36	0.09	0.61	0.18	2.29	1.86		0
4	0.24	0.04	0.29	0.06	1.58	2.20		0
5	0.52	0.17	0.83	0.26	3.54	2.35	Y	0
6	0.79	0.26	0.79	0.26	4.57	2.40	Y	0
7	0.22	0.04	0.43	0.11	1.98	1.58		0
8	0.20	0.04	0.24	0.05	1.81	2.12		0
9	0.89	0.30	1.18	0.38	4.00	2.70	Y	0
10	0.64	0.20	0.70	0.22	2.71	2.45		0
11	0.54	0.16	0.74	0.24	1.70	1.37		0
12	0.36	0.10	0.52	0.17	2.84	2.24		0
13	0.59	0.18	0.58	0.18	3.78	2.81		0
14	0.28	0.06	0.25	0.05	3.18	3.43		0
15	1.39	0.43	1.81	0.61	7.03	4.80	Y	17.9
16	1.03	0.35	1.10	0.37	3.71	2.28		0
17	0.65	0.20	0.89	0.28	5.39	3.50		0
18	1.69	0.53	2.36	0.69	5.77	2.48	Y	46.0
19	0.24	0.04	0.25	0.05	2.57	3.47		0
20	1.62	0.51	2.11	0.59	5.37	3.12	Y	12.7
21	0.25	0.03	0.48	0.15	1.66	1.86		0
22	0.41	0.11	0.62	0.19	3.47	3.07	Y	0
23	0.65	0.21	0.97	0.32	4.18	3.76	Y	0
24	1.13	0.43	0.90	0.29	2.95	1.88		0
25	0.23	0.04	0.62	0.19	3.84	3.88		0

$$\Sigma = 76.6$$

$$P_F = \frac{\Sigma}{25} = \frac{76.6}{25} = 3.1\%$$

- (1) Y indicates that turbine pedestal did impact the Operating Floor. For all other cases, no impact occurred.



Table 5-2. Nonlinear Results for Median Structural Model at  $\bar{S}_a = 6.0G$ 

TRIAL NO.	WALL 19		WALL 31		OPERATING FLOOR DRIFT (Inches)	TURBINE PEDESTAL DRIFT (Inches)	PEDESTAL IMPACT CASES(1)	PROBA-BILITY OF SEVERE WALL DISTRESS(%)
	TOP DRIFT (Inches)	MAX STORY DRIFT (%)	TOP DRIFT (Inches)	MAX STORY DRIFT (%)				
1	4.8	0.89	5.9	1.46	8.8	6.1		100
2	6.4	0.97	7.7	2.05	14.0*	10.6		100
3	2.1	0.59	4.2	0.97	7.4	4.0		99
4	2.4	0.66	3.1	0.90	7.3	4.6		95
5	3.2	0.84	5.8	1.20	8.6	5.2		100
6	4.6	0.82	6.3	1.50	11.5*	8.1		100
7	1.5	0.48	2.0	0.65	4.4	3.1		31
8	1.3	0.43	1.9	0.64	3.6	3.5	N	27
9	7.2	1.16	9.1	1.89	13.1*	9.7		100
10	2.8	0.71	4.0	1.13	7.3	5.4		100
11	1.5	0.48	1.8	0.57	3.9	2.8	N	9
12	3.6	0.81	5.9	1.45	9.3*	5.9		100
13	3.8	0.74	5.6	1.41	10.7*	7.3		100
14	3.0	0.73	4.2	1.21	8.8*	6.3		100
15	6.6	1.05	9.4	2.08	11.8*	9.9		100
16	6.6	1.00	8.2	1.67	11.8*	8.4		100
17	6.1	1.09	8.1	1.72	10.3	8.3		100
18	10.1	1.82	12.2	2.76	18.5*	15.1		100
19	1.6	0.55	2.8	0.95	5.6	5.3	N	98
20	7.7	1.23	8.8	1.91	14.2*	10.8		100
21	1.7	0.55	2.0	0.65	4.9	4.0		31
22	4.3	0.77	5.3	1.33	10.0*	6.6		100
23	3.8	0.82	5.2	1.45	9.6*	6.2		100
24	4.2	0.81	5.2	1.33	7.9	5.0		100
25	2.2	0.68	5.0	1.28	8.0	6.8		100

 $\Sigma = 2190$ 

$$P_F = \frac{\Sigma}{25} = \frac{2190}{25} = 87.6\%$$

\* Relative diaphragm drift exceeds the limits of applicability of the bilinear force-deflection relationship used for the operating floor so that diaphragm drifts are likely to be underpredicted and wall drifts are likely to be overpredicted to some extent for these cases.

(1) N indicates that the Turbine Pedestal did not impact the Operating Floor. For all other cases there was impact.



Table 5-3. Elastic Deformed Shape at Yield Versus Inelastic Deformed Shapes at Several Different Drift Levels for Wall 31

CASE	EL 107 DRIFT		EL 119 DRIFT	EL 140 DRIFT	$\nu_s$	$\nu$	$\xi_a$ (6)
	%	(Inches)	(Inches)	(Inches)			
ELASTIC YIELD	0.043	0.11	0.16	0.25	1.0	1.0	2.05
3.0G MEDIAN	0.22	0.58	0.63	0.72	5.1	3.3	3.0
--	0.40	1.06	1.14	1.27	9.3	6.0	--
--	0.70	1.85	2.10	2.56	16.4	11.5	--
6.0G MEDIAN	1.33	3.5	4.1	5.3	31.1	23.2	6.0



Table 5-4. Estimated  $F_u$  Values From Spectral Averaging Method for Various Maximum Story Drifts in Wall 31

MAXIMUM STORY DRIFT (%)	$\nu$	$f_s/f$	B	$f_u/f$	$f'_{ea}/f$	$\beta'_{ea}$	$f_s$ (Hz)	$f_u$ (Hz)	$\overline{S_a (f_u - f_s, \beta'_{ea})}$ (G)	$F_u$	PRE-DICTED $\overline{S_a}$ (G)	RATIO PREDICTED TO ACTUAL $\overline{S_a}$
0.043	1.0	1.0	0	1.0	1.0	7%	8.6	8.6	1.75	1.0	2.05	1.0
0.22	3.3	.569	0.7	.698	.634	9.5%	4.9	5.7	1.78	1.31	2.67	0.89
0.40	6.0	.438	0.7	.606	.522	9.3%	3.8	5.2	1.81	1.58	3.23	N.A.
0.70	11.5	.338	0.7	.537	.438	8.5%	2.9	4.6	1.83	2.10	4.30	N.A.
1.33	23.2	.269	0.7	.488	.379	7.6%	2.3	4.2	1.88	3.07	6.27	1.05

5-37



Table 5-5. Estimated  $F_u$  Values from Various Methods at Differing Maximum Story Drifts for Wall 31

MAXIMUM STORY DRIFT (%)	$\nu$	ACTUAL $\bar{S}_a$ (G)	1 SPECTRAL AVERAGING		2 RIDDELL-NEWMARK		3 MODIFIED RIDDELL-NEWMARK		4 EFFECTIVE RIDDELL-NEWMARK		AVERAGE 1 & 4 $\bar{S}_a$ (G)
			$F_u$ EQ.(5-15)	$\bar{S}_a$ (G)	$F_u$ EQ.(5-18)	$\bar{S}_a$ (G)	$F_u$ EQ.(5-24)	$\bar{S}_a$ (G)	$F_{ue}$ EQ.(5-25)	$\bar{S}_a$ (G)	
0.22	3.3	3.0	1.31	2.67	1.92	3.93	2.03	4.16	1.65	3.37	3.02
0.40	6.0	NA	1.58	3.23	2.05	4.19	2.31	4.72	1.84	3.77	3.50
0.70	11.5	4.6*	2.10	4.30	2.20	4.50	2.77	5.68	2.19	4.48	4.39
1.33	23.2	6.0	3.07	6.27	3.46	7.07	3.66	7.49	2.86	5.86	6.07

\* Approximate Estimate Based on Equation (5-4)



## 6. NONLINEAR ANALYSES WITH UNCERTAIN STRUCTURE PROPERTIES

### 6.1 Results

Using the randomly selected structure damping, stiffness, and strength modification factors shown in Table 2-7, a total of 150 nonlinear time-history analyses were performed (50 each at  $\bar{S}_a = 3.0, 4.0, \text{ and } 6.0g$ ). At each  $\bar{S}_a$  level, each of the 25 input time-histories were used twice. Thus, these analyses incorporate uncertainty in structure properties as well as randomness variability of the input motion. Table 6-1 tabulates the maximum story drift as a percentage of the wall segment height for both Walls 19 and 31. In nearly every case, these maximum story drifts occurred in the lowest segment of each wall. For each trial, the composite probability of severe wall distress is estimated based upon the median drift limit of 0.7% and composite variability,  $\beta_c$ , of 0.335 discussed in Section 2.1.3. The overall composite probability of severe wall distress is computed using Equation 5-1 for each  $\bar{S}_a$  level. Those trials in which turbine pedestal and operating floor impact occurred are also indicated. Lastly, Table 6-1 indicates those cases where the relative drifts of the operating floor exceeded the limits of Equation 2-14 related to the applicability of the operating floor bilinear force-deflection relationship. No such exceedances occurred at  $\bar{S}_a = 3.0g$ . Only two such trials exceeded the Equation 2-14 limit at  $\bar{S}_a = 4.0g$  and



even though the computed maximum story drifts may be slightly high for those two trials, the overall probability of failure reported at  $\bar{S}_a = 4.0g$  is not judged to have been influenced. However, the Equation 2-14 limit was exceeded for 22 of the 50 trials (44%) at  $\bar{S}_a = 6.0g$ . For those 22 trials, the computed maximum story drifts of the shear walls are likely to be slightly high because the too stiff modeling of the operating floor transmits somewhat excessive shear load into these walls. The effect is that the overall probability of severe distress reported at  $\bar{S}_a = 6.0g$  is likely to be slightly high. This effect leads to a slight conservatism in the computed median  $\bar{S}_a$  capacity. However, the error is judged to be small because no such effect occurs at either the  $\bar{S}_a = 3.0$  or  $4.0 g$  levels.

Table 6-2 summarizes both the median and 90% bounds on drifts at various locations for  $\bar{S}_a = 3.0, 4.0,$  and  $6.0g$  with uncertain structure properties and compares those values with the corresponding values for median structure properties.

Similar to the cases using median centered structure properties, the cases with uncertain structure properties demonstrate that, in most cases, Wall 31 develops larger maximum story drifts than does Wall 19. For 82% of the trials, Wall 31 had the larger maximum story drifts. Although this percentage is down some from the randomness-only trials of



Section 5, the trend is still sufficiently clear to indicate that severe damage is more likely to occur in Wall 31 than in Wall 19.

The uncertain structural properties cases confirm the observation of Section 5 that operating floor impact into the turbine pedestal is very unlikely unless the operating floor drifts more than the gap size of 3.375 inches (i.e., the operating floor and turbine pedestal tend to be in-phase and their drifts do not add, but subtract to some extent).

At  $\bar{S}_a = 3.0g$ , impacts only occurred in 36% of the trials even though the median operating floor drift was 3.1-inches and had 90% bounds of 1.19 to 6.92 inches. The percentage of trials with impacts increased to 58% and 84% at  $\bar{S}_a = 4.0$  and  $6.0g$ , respectively. At each  $\bar{S}_a$  the percentage of impact cases using uncertain properties remains essentially the same as that obtained using median structure properties. Thus, uncertainty of structure properties did not change impact percentages.

At  $\bar{S}_a = 3.0g$ , uncertain structural properties increased the median level and very significantly increased the 95% non-exceedance probability (NEP) level while only slightly reducing the 5% NEP level for both maximum story drifts and overall wall drifts. When the story drift associated with severe wall damage was also treated as uncertain, the probability of severe wall distress increased significantly to 11.1% from the 3.1% probability obtained for median structure properties. The



same trend was not observed with regard to operating floor drifts. Uncertain structure properties lowered the median, significantly lowered the 5% NEP and only slightly increased the 95% NEP operating floor drifts. It is believed that this reverse tendency occurs because of the low median natural frequency of 4.0 Hz for the operating floor. With lower strength or lower stiffness properties, the operating floor is driven out of the power of the majority of the ground motion records and so drifts do not tend to increase with these lower strength or lower stiffness properties as one would otherwise expect. On the other hand, with increased stiffness or strength properties, drifts are also reduced. Therefore, a change from the median in either direction tends to reduce drifts for many of the input records.

At  $\bar{S}_a = 6.0g$ , the shear walls tended to soften so much that their effective frequency was in the same regime as that of the operating floor. Thus, at  $\bar{S}_a = 6.0g$ , uncertainty in structural properties has roughly the same effect on the shear wall drifts as seen for the operating floor at both  $\bar{S}_a = 3.0$  and  $6.0g$  (i.e., median and 5% NEP drifts are reduced, and 95% NEP drifts do not increase significantly and are generally reduced from those obtained with the median structure model). When uncertainty in story drifts associated with severe wall damage are also included, the probability of severe wall distress is significantly reduced to 76.7% from the 87.6% obtained considering randomness only.



For use in an SPRA study, the probabilities of severe wall distress shown in Table 6-1 together with the probabilities in Tables 5-1 and 5-2 for randomness-only cases were fit with a lognormal distribution. The resulting estimated median  $\bar{S}_a^v$ , and logarithmic standard deviations for randomness,  $\beta_R$ , composite variability,  $\beta_C$ , and uncertainty,  $\beta_U$ , are:

Turbine Building Fragility Estimate

$$\begin{aligned}
 \text{Median } \bar{S}_a^v &= 4.59g \\
 \beta_C &= 0.37 \\
 \beta_R &= 0.23 \\
 \beta_U &= 0.29 \\
 \text{HCLPF } \bar{S}_a &= 1.95g
 \end{aligned}
 \tag{6-1}$$

Also shown is the High-Confidence-Low-Probability-of-Failure (HCLPF) estimate of  $\bar{S}_a$  associated with about a 95% confidence of less than about a 5% probability of severe shear wall distress. This HCLPF capacity is computed from:

$$\text{HCLPF } \bar{S}_a = \bar{S}_a^v e^{-1.65(\beta_R + \beta_U)}
 \tag{6-2}$$

and is appropriate for comparison with median input spectra.



Assuming a lognormal distribution with the parameters defined by Equation 6-1 leads to the following probability of severe wall distress estimates:

$\bar{S}_a$ (G)	RANDOMNESS ONLY MEDIAN $P_F$ (%)	RANDOMNESS + UNCERTAINTY COMPOSITE $P_F$ (%)
3.0	3.2 (3.1)	12.5 (11.1)
4.0	27.7	35.5 (37.2)
6.0	87.8 (87.6)	76.5 (76.7)

This table also shows, in parentheses, the probabilities of severe wall distress actually estimated from the multiple nonlinear time-history analyses. The fit is considered acceptable.



## 6.2 Prediction of Fragility Including Uncertainty from Elastic Results

The median  $\bar{S}_a^v$  of 4.39g predicted in Section 5.2 from extrapolating the results of a median centered elastic response spectrum analysis conservatively underpredicts  $\bar{S}_a^v = 4.59g$  in Equation 6-1 from the multiple nonlinear analyses by less than 5%. Similarly, the  $\beta_R = 0.23$  predicted in Section 5.2 without the nonlinear analyses accurately estimates the  $\beta_R = 0.23$  value from Equation 6-1. Thus, for the Turbine Building perfectly adequate or slightly conservative estimates of  $\bar{S}_a^v$  and  $\beta_R$  were obtained by extrapolating the results of a single median centered elastic response spectrum analysis. However, it remains to estimate the uncertainty variability,  $\beta_U$ .

The logarithmic standard deviation on uncertainty,  $\beta_U$ , is made up of the uncertainty on strength or capacity  $\beta_{U_C}$ , the uncertainty effect due to frequency shifting,  $\beta_{U_f}$ , resulting from the uncertainty in stiffness,  $\beta_{U_{STIFF}}$ , and the uncertainty in inelastic energy absorption,  $\beta_{U_I}$ , due to uncertainty in the drift limits,  $\beta_{U_D}$ , associated with severe shear wall distress. Thus, assuming the properties of independent lognormally distributed variables:

$$\beta_U = [(\beta_{U_C})^2 + (\beta_{U_f})^2 + (\beta_{U_I})^2]^{1/2} \quad (6-3)$$



Note that Equation 6-3 does not contain any term associated with uncertainty in elastic damping level. When a structure goes substantially nonlinear, the level of elastic damping used in the analysis becomes very unimportant. Energy dissipation is primarily in the nonlinear hysteretic loops and not by elastic damping. When  $\bar{S}_a$  is computed using Equation 5-6 for significantly nonlinear structures, the influence of substantial variability in elastic damping on  $\bar{S}_a$  becomes negligible irrespective of whether the Spectral Averaging method or the Riddell-Newmark method described in Section 5.2 is used to compute  $F_u$ . One may ignore variability in elastic damping when substantial nonlinear behavior is involved. This judgement was borne out by the nonlinear time-history results which showed that computed maximum story drifts were uncorrelated with the level of elastic damping used, at least within the 3% to 13% elastic damping range, as will be shown in Section 6.5.

The strength variability  $\beta_{U_C} = 0.25$ , defined in Section 2.6 and used to establish the uncertain structure properties for the nonlinear analysis models, is used directly in Equation 6-3.

The inelastic energy absorption uncertainty factor,  $\beta_{U_I}$ , is determined by estimating  $\bar{S}_a$  at both the median and a lower drift level. A drift limit of 0.4% is estimated to lie  $1.87 \beta_{U_D}$  below the median drift limit of 0.7% based upon  $\beta_{U_D} = 0.30$  as defined in Section 2.6. Table 5-5 pre-



sents estimated  $\bar{S}_a$  values of 4.39g and 3.50g for drift limits of 0.7% and 0.4%, respectively. Thus:

$$\beta_{U_I} = \frac{\ln\left(\frac{4.39}{3.50}\right)}{1.87} = 0.12 \quad (6-4)$$

The frequency shift effect factor,  $\beta_{U_f}$ , is similarly estimated starting with  $\beta_{U_{STIFF}} = 0.50$  from Section 2.6. Based on this  $\beta_{U_{STIFF}}$ , a stiffness reduction factor of 0.44 is estimated to lie 1.65  $\beta_{U_{STIFF}}$  below the median. Such a stiffness reduction factor leads to an elastic modal frequency of 5.7 Hz for the mode predominantly influencing Wall 31. Using the methods described in Section 5.2, a revised  $\bar{S}_a^v$  is computed for this reduced stiffness case at a median drift limit of 0.7% and for the median spectrum shape of Figure 3-27. Following this approach for the reduced stiffness case, the estimated system ductility is 5.0 for a drift limit of 0.7%. With this system ductility, the value of  $\bar{S}_a^v$  is estimated to be 3.23g by the Spectral Averaging method and 3.53g by the Effective Riddell-Newmark method. Averaging these two results together leads to  $\bar{S}_a^v = 3.38g$  versus  $\bar{S}_a = 4.39g$  for median stiffness properties. Then:

$$\beta_{U_f} = \frac{\ln\left(\frac{4.39}{3.38}\right)}{1.65} = 0.16 \quad (6-5)$$



Combining  $\beta_{U_C}$ ,  $\beta_{U_f}$ , and  $\beta_{U_I}$  by Equation 6-3,  $\beta_U = 0.32$  is obtained which is about 33% greater than the value of  $\beta_U$  given by Equation 6-1 based upon the multiple nonlinear analyses. A summary of comparative results is shown in Table 6-3. It is noted that the median capacity is only about 5% low, but the HCLPF capacity is about 10% low when estimated by the extrapolated elastic approach described herein and recommended for use on other structures.

### 6.3 Other Sources of Variability and Conservatism

Three sources of variability and conservatism were not treated in the nonlinear time history analyses. These are:

1. Modeling Uncertainty: Only a single mathematical model was used. Structure properties were varied, but the model was not varied. The model which was used is judged to be median-centered. It is further judged that modeling uncertainty is about  $\beta_{U_M} = 0.15$ , which is equivalent to stating that the 95% NEP responses near the base of the shear walls could have been as much as 1.28 times those reported herein if differing models had been used.



2. Earthquake Component Variation: Within this study the fragility of the east-west shear walls were defined in terms of  $\bar{S}_a$  associated with the east-west direction of ground motion. However, in the SPRA, the seismic hazard is defined in terms of the average horizontal component,  $\bar{S}_a$ . The east-west directional component is expected to have the same median value as the average horizontal component (i.e.,  $\bar{S}_A^v = \bar{S}_A$ ). However, the randomness variability,  $\beta_{R_{DIR}}$ , for the  $\bar{S}_a$  of the east-west component given an  $\bar{S}_a$  is estimated to be about 0.12. Thus, the 95% NEP bounds on  $\bar{S}_a$  is  $1.22 \bar{S}_a$ .
3. Ground Motion Incoherence: At any instant in time, the ground acceleration is not the same at every location under the Turbine Building foundation. The LTSP soil-structure interaction analysis considered this aspect for Diablo Canyon and it was estimated that east-west shear wall responses are reduced by a median factor of  $F_{GMI}^v = 1.06$  with estimated randomness  $\beta_{R_{GMI}} = 0.02$  and uncertainty  $\beta_{U_{GMI}} = 0.06$ . These  $\beta$  values result in 95% confidence that there is less than 5% probability that  $F_{GMI}$  is less than 0.93 which very conservatively suggests a possible increase in response of 8%.



Table 6-4 includes the effects of these three additional parameters on the fragility estimate for the Turbine Building. The median capacity is raised by 6% to 4.87g and the HCLPF capacity is lowered by 6% to 1.84g.

#### 6.4 Influence of Ground Motion Characterization on Shear Wall Drift When Structure Parameter Variation is Incorporated

Section 5.3 described the ground motion characteristics which result in the larger shear wall drifts when  $\bar{S}_a = 3.0g$  for the case of median structure properties. These same ground motion characterizations also correspond to the larger drift cases when structure property variations are included. However, structure property variation does increase the possible drift levels when ground motions approach or exceed the limits of Equations 5-32 and 5-33.

A maximum story drift limit of 0.4% is estimated to correspond to about a 5% composite probability of severe shear wall distress. Thus, there would be high confidence of a low probability of failure if there was high confidence that a maximum story drift limit of 0.4% would not be reached when the Turbine Building was subjected to ground motion input. At  $\bar{S}_a = 3.0g$ , 15 cases out of 50 (30%) produced maximum story drifts in excess of 0.4%. Eleven of these cases were for ground motion records which significantly exceeded the limits of Equations 5-32 and



5-33. The other four cases were Trial 13 (Record 13), Trial 22 (Record 22), Trial 25 (Record 25), and Trial 26 (Record 1). These four cases are discussed further.

Trial 13 produced a maximum story drift of 0.71%. Record 13 scaled to  $\bar{S}_a = 3.0g$  easily exceeds the higher frequency limit of Equation 5-33, but produces lower frequency spectral acceleration only 79% as high as the limit of Equation 5-32. Therefore, purely from a ground motion standpoint, the high maximum story drift from Trial 13 is a surprise. However, it will be shown in the next section that high drifts also correlate strongly with trials that had low shear wall stiffness and low shear wall strength. For Trial 13, the shear wall stiffnesses were only 60% of their median values while the shear wall strengths were only 72% of their median values (Table 2-7). This unfavorable combination of both low shear wall stiffness (approximately  $-1.0 \beta$ ) and low strength (approximately  $-1.3 \beta$ ) has an expected probability of only about 1.5%. Therefore Trial 13 represents a very unfavorable extreme condition and thus, it is not surprising that Trial 13 produced a high drift despite the fact that Record 13 has spectral acceleration of only 79% of the limits of Equation 5-32.

Trials 22 and 25 produced maximum story drifts of 0.52% and 0.43%, respectively. Both Records 22 and 25 scaled to  $\bar{S}_a = 3.0g$  produced



spectral accelerations well in excess of the low frequency limits of Equation 5-32 but their high frequency spectral accelerations were only 97% and 85% of the limits of Equation 5-33, respectively. The shear walls in these two trials had about median stiffnesses, but low strengths of 86% and 69% of the median levels, respectively. Such lower strengths coupled with the ground motion records barely passing the limit of Equation 5-33 accounts for the story drifts in excess of 0.4%.

Trial 26 produced a maximum story drift of 0.41%. Record 1, which is associated with this trial, has substantial high frequency spectral acceleration well above the limit of Equation 5-33, and has a low frequency spectral acceleration equal to 85% of the limit of Equation 5-32. Trial 26 had essentially median shear wall strengths, but had shear wall stiffnesses only 57% of their median levels. This low stiffness easily accounts for the 0.41% drift from Record 1.

Based on the exceptions of these four trials, the spectral limits of Equations 5-32 and 5-33 are lowered by approximately a factor of 1.3 to fully cover the possibility of reasonable combinations of lower than median stiffnesses and strengths for the shear walls. With this reduction, there is high confidence that maximum story drifts in excess of 0.4% will not result so long as the 5% damped spectral accelerations do not exceed both of these limits.



Therefore, even considering a reasonable range of uncertain structure properties, there is high confidence of a low probability of failure of the Turbine Building shear walls so long as either of the following limits are met:

HCLPF Limits

High Frequency Limit

$$\text{Max } S_{a5\%} \leq 1.6g \text{ in the 8.6 to 9.5 Hz frequency range} \quad (6-6)$$

Low Frequency Limit

$$\text{Max } S_{a5\%} \leq 2.8g \text{ in the 2.4 to 2.8 Hz frequency range} \\ \text{and} \quad (6-7)$$

$$\text{Max } S_{a5\%} \leq 2.25g \text{ in the 1.7 to 2.0 Hz frequency range}$$

The possibility of severe distress to the shear walls requires both of these two limits to be exceeded.



### 6.5 Influence of Structure Property Variability on Shear Wall Drift

To study the influence of structure property variability on maximum shear wall drift, plots of maximum story drift versus structure property value were made for each of the structure parameter values tabulated in Table 2-7 for the 50  $\bar{S}_a = 3.0g$  trials. These plots indicate that the maximum story drifts associated with  $\bar{S}_a = 3.0g$  correlated to some extent with the Shear Wall Stiffness and Shear Wall Strength Ratios shown in Table 2-7. They also showed that shear wall maximum story drifts did not correlate at all with the Operating Floor and Turbine Pedestal Stiffness or Strength Ratios, nor do they correlate with the elastic system Damping value used. All of these results are consistent with prior expectations. These drift versus structure parameter plots are presented in Figures 6-1 through 6-7.

Figure 6-2 illustrates that the 8 trials with maximum story drifts in excess of 0.5% were all associated with Shear Wall Stiffness Ratios less than 1.25. Conversely, for the five trials with Shear Wall Stiffness Ratios greater than 2.2, the maximum story drift never exceeded 0.33% irrespective of the ground motion record used. Three of these five trials (Trials 6, 23, and 45) used ground motion records which had spectral accelerations exceeding the limits of Equations 5-32 and 5-33 and thus exceeded the limits of Equations 6-6 and 6-7 by more than a factor



of 1.3. These ground motions were capable of producing much larger drifts and in fact did so for the other trial which used each of these same records. The low drift in these five cases is primarily due to the high Shear Wall Stiffness Ratio used in these trials.

Figure 6-3 illustrates that the eight trials with maximum story drifts in excess of 0.5% also correspond to Shear Wall Strength Ratios less than 1.0. Conversely, the 12 trials with Shear Wall Strength Ratios in excess of 1.16 all produced maximum story drifts less than 0.37%. Nine of those twelve trials (Trials 5, 9, 23, 24, 27, 30, 34, 45, and 49) used ground motion records which had spectral accelerations exceeding the limits of Equations 6-6 and 6-7 by more than a factor of 1.3 and yet did not produce substantial drifts. Drifts at a given  $\bar{S}_a$  level are even more sensitive to the Shear Wall Strength Ratio than to the Shear Wall Stiffness Ratio.

It can be concluded that to get shear wall drifts in excess of 0.5%, all three of the following conditions must exist:

1. Both of the ground motion spectral acceleration limits of Equations 6-6 and 6-7 must be exceeded, and
2. The Shear Wall Stiffness Ratio must be less than 1.25, and



3. The Shear Wall Strength Ratio must be less than 1.0.

If any one of these three conditions were missing, maximum story drifts were less than 0.5%. The most important of these conditions is the first condition on ground motion level. Unless this condition is exceeded, drifts were limited to 0.4% irrespective of the Shear Wall Stiffness and Strength Ratios. For this reason, Figures 6-2 and 6-3 show large scatter in correlating drifts with stiffness or strength.



61-9

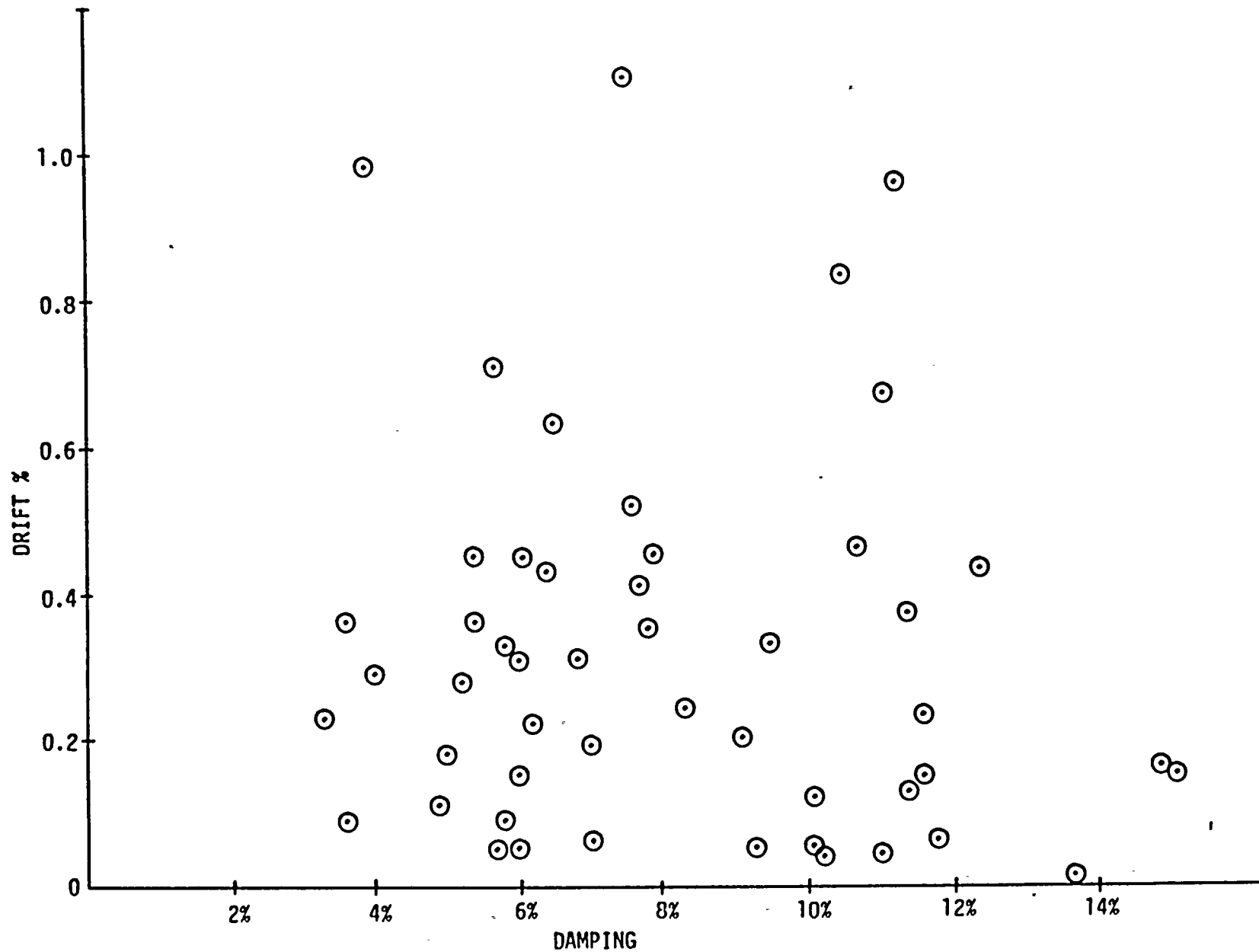


Figure 6-1. Maximum Story Drift for  $S_a = 3.0g$  Versus Damping



6-20

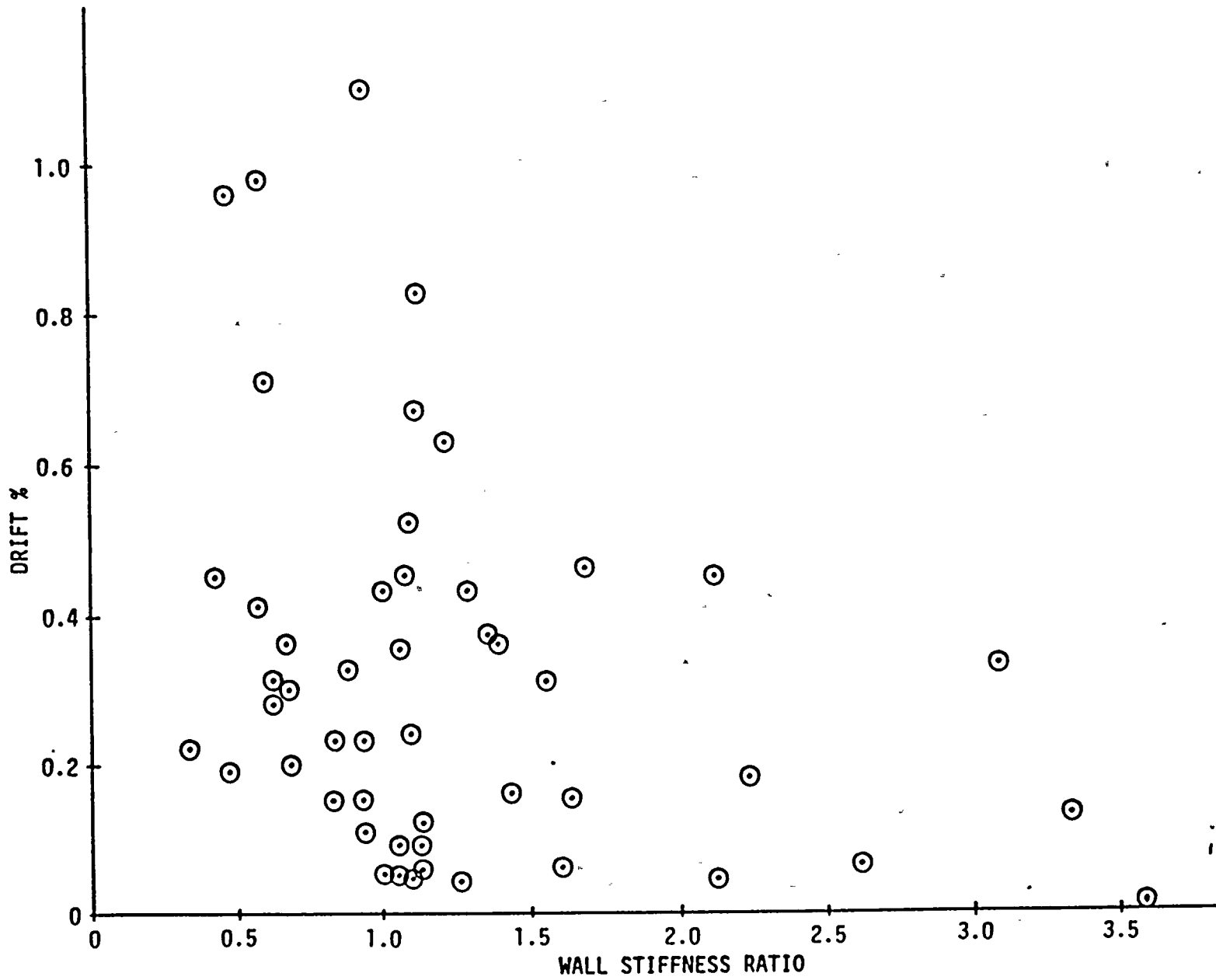


Figure 6-2. Maximum Story Drift for  $\bar{S}_a = 3.0g$  Versus Shear Wall Stiffness Ratio



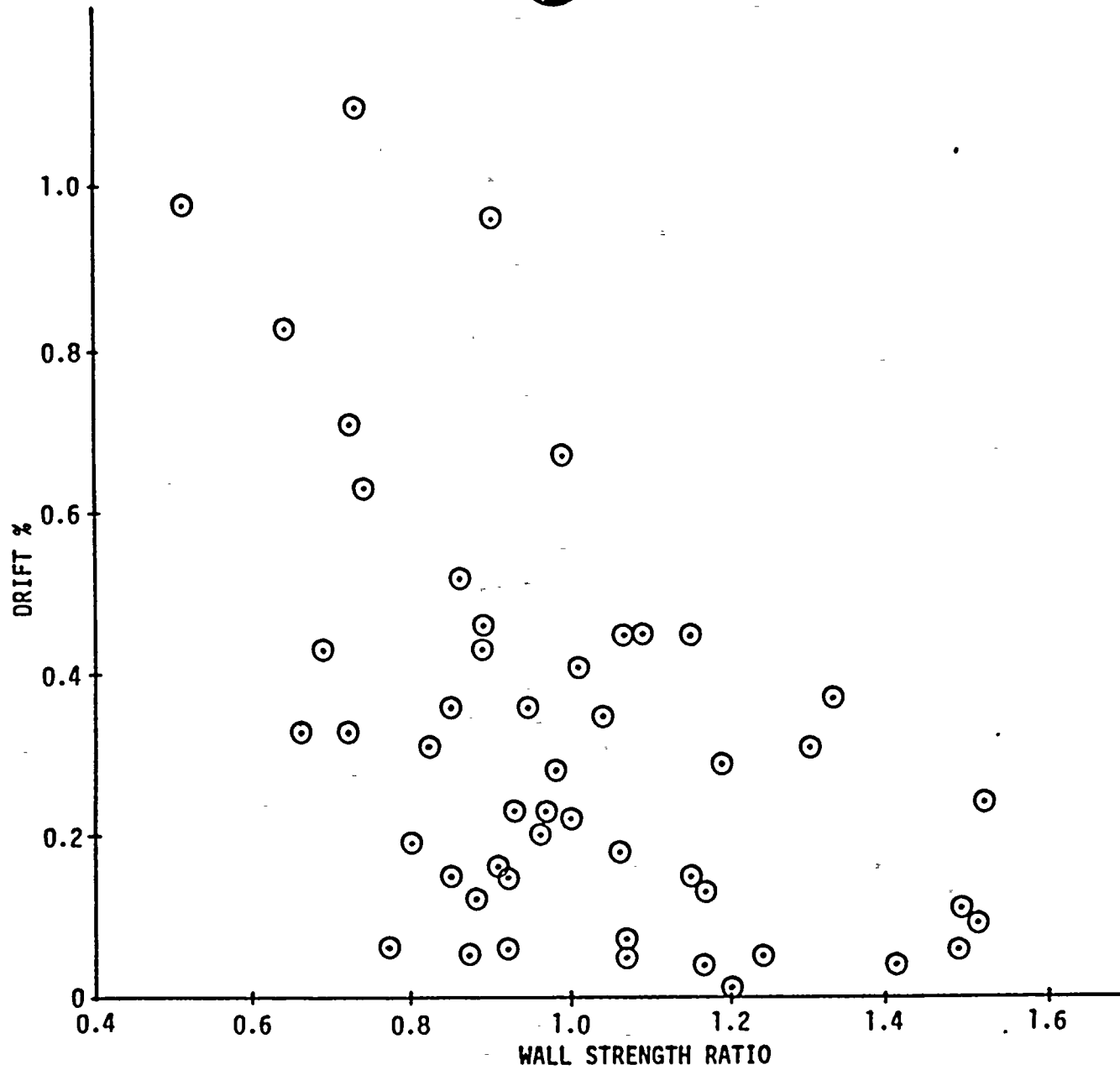


Figure 6-3. Maximum Story Drift for  $S_a = 3.0g$  Versus Shear Wall Strength Ratio



6-22

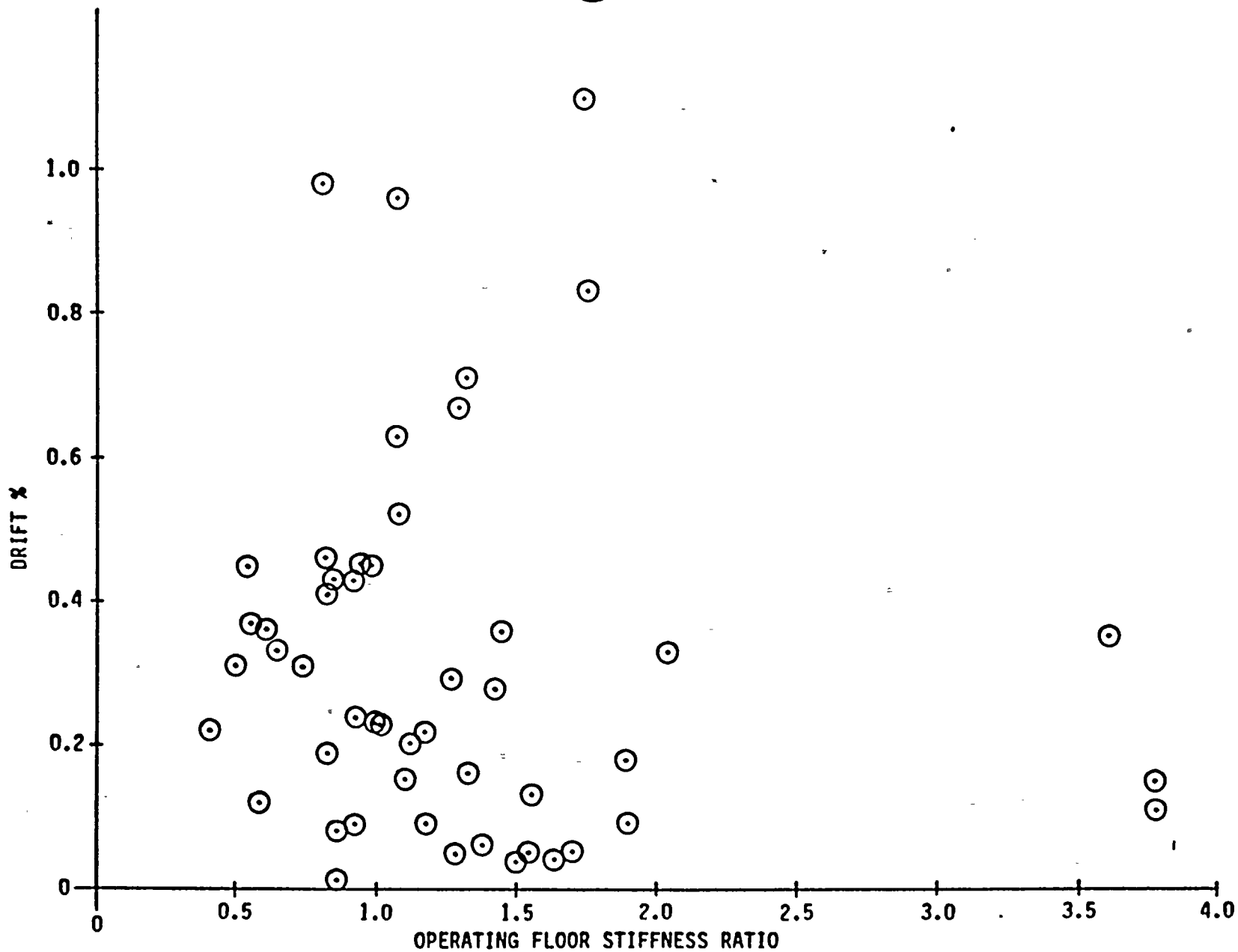


Figure 6-4. Maximum Story Drift for  $\bar{S}_a = 3.0g$  Versus Operating Floor Stiffness Ratio



6-23

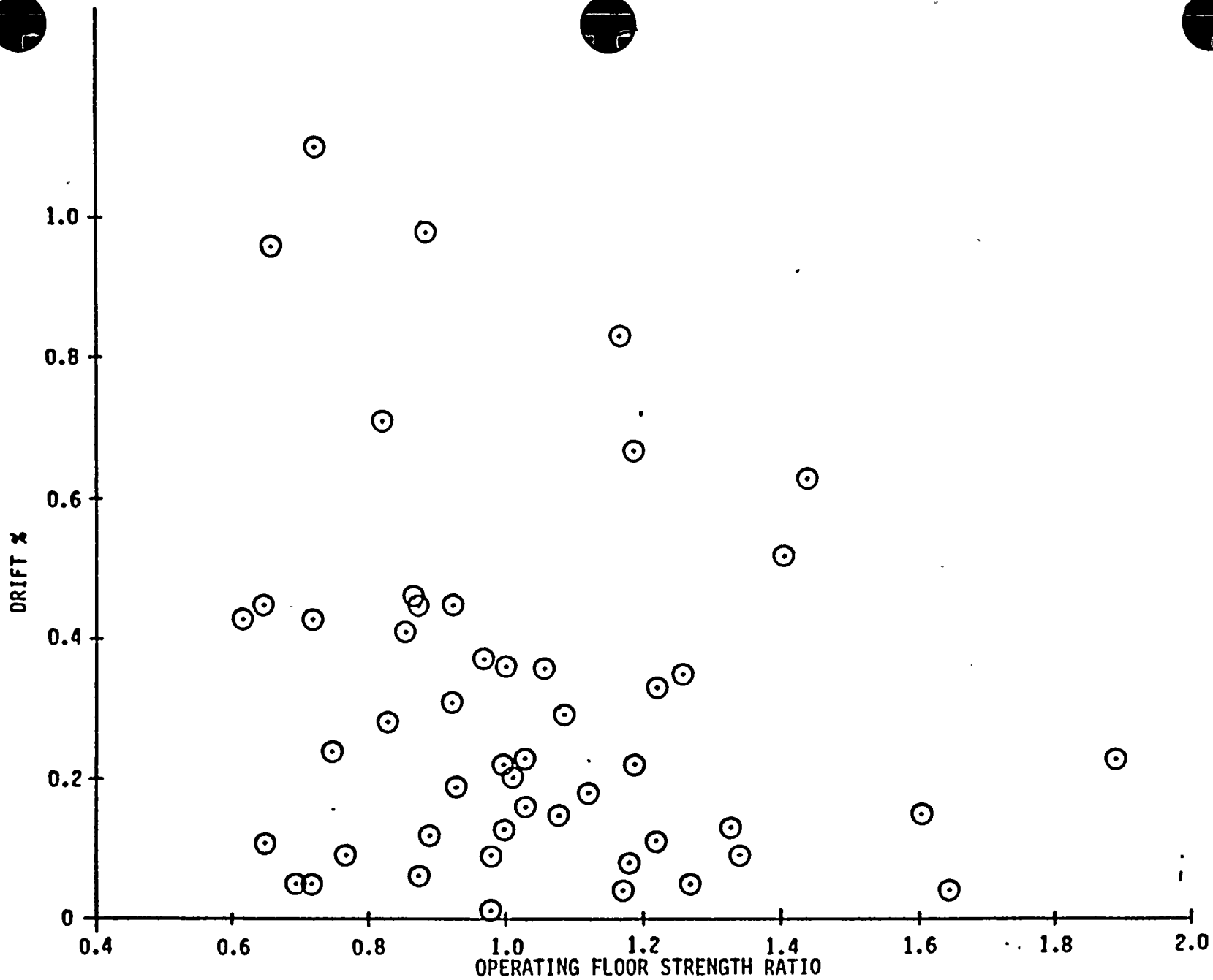


Figure 6-5. Maximum Story Drift for  $\bar{S}_a = 3.0g$  Versus Operating Floor Strength Ratio



6-24

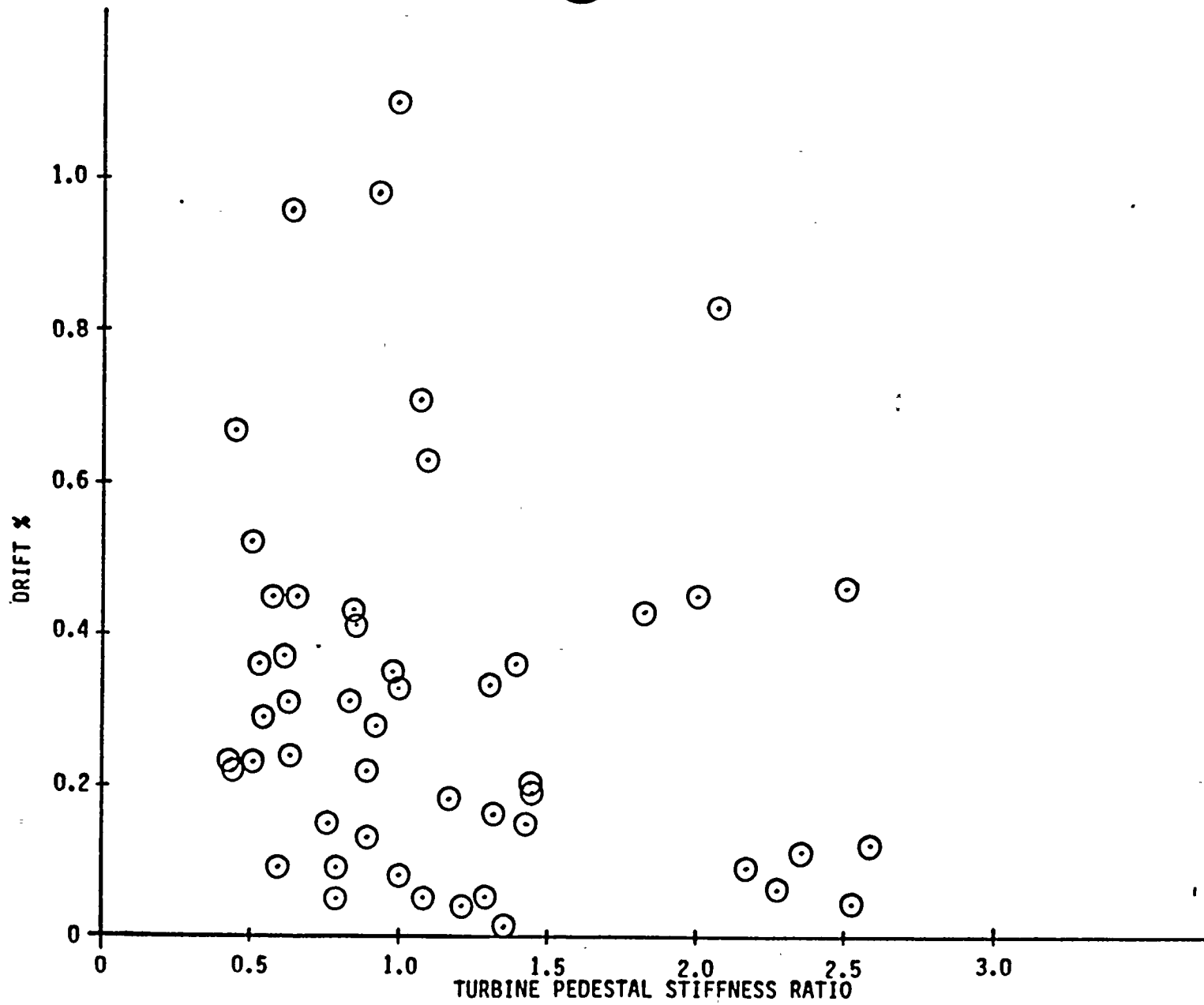


Figure 6-6. Maximum Story Drift for  $\bar{S}_a = 3.0g$  Versus Turbine Pedestal Stiffness Ratio



6-25

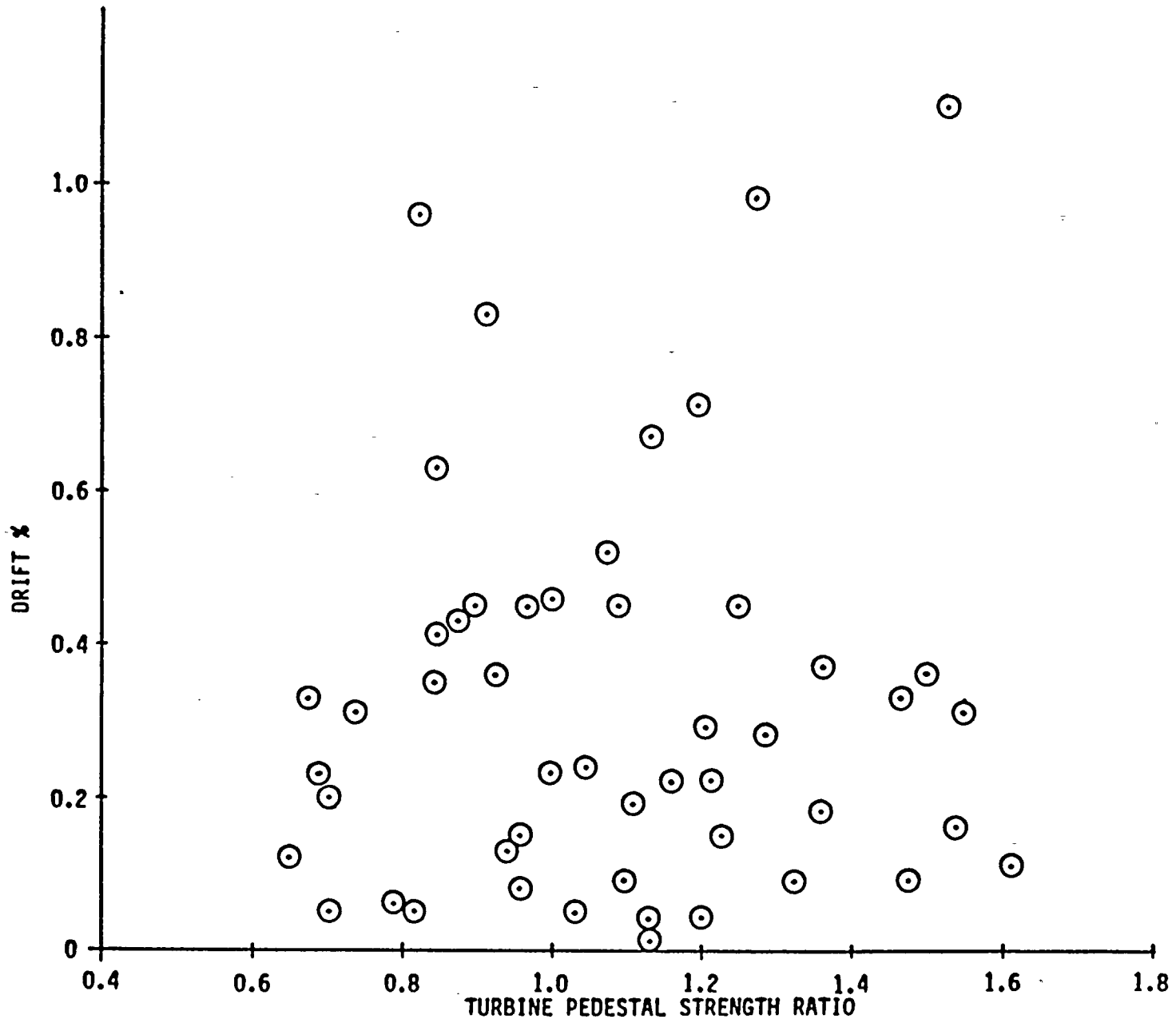


Figure 6-7. Maximum Story Drift for  $\bar{S}_a = 3.0g$  Versus Turbine Pedestal Strength Ratio



Table 6-1. Nonlinear Results for Uncertain Structural Properties

TRIAL NO.	$\Sigma_a = 3.0G$				$\Sigma_a = 4.0G$				$\Sigma_a = 6.0G$			
	MAX STORY DRIFT(X)		PROB. SEVERE DISTRESS (X)	PEDESTAL IMPACT (1)	MAX STORY DRIFT(X)		PROB. SEVERE DISTRESS (X)	PEDESTAL IMPACT (1)	MAX STORY DRIFT(X)		PROB. SEVERE DISTRESS (X)	PEDESTAL IMPACT (1)
	WALL 19	WALL 31			WALL 19	WALL 31			WALL 19	WALL 31		
1	0.19	0.15	0	Y	0.29	0.64	39.4	Y	0.94	1.27	96.2*	Y
2	0.45	0.37	9.3		1.10	0.65	91.1	Y	1.76	1.62	99.7*	Y
3	0.19	0.23	0		0.40	0.46	10.6	Y	1.23	0.99	95.4	Y
4	0.04	0.05	0		0.18	0.25	0		0.63	0.86	72.9	Y
5	0.02	0.04	0		0.06	0.11	0		0.37	0.60	67.4	Y
6	0.19	0.33	1.3	Y	0.47	0.52	18.7	Y	1.68	0.92	99.5*	Y
7	0.03	0.09	0		0.16	0.29	0.4		0.42	0.66	57.1	
8	0.02	0.05	0		0.05	0.09	0		0.27	0.44	8.2	
9	0.06	0.31	0.8	Y	0.24	0.40	4.7	Y	1.15	1.09	93.1*	Y
10	0.03	0.06	0		0.06	0.20	0		0.47	0.66	42.9	Y
11	0.22	0.19	0		0.75	0.35	58.3		0.72	0.86	72.9	Y
12	0.14	0.16	0		0.29	0.44	8.2		0.53	0.97	83.4	Y
13	0.42	0.71	51.6	Y	0.67	1.24	95.6	Y	1.20	1.97	99.9*	Y
14	0.09	0.06	0		0.28	0.40	4.7	Y	0.53	0.90	77.3	Y
15	0.72	0.96	82.6		1.18	1.84	99.8		1.97	2.81	100.0	Y
16	0.45	0.63	37.8		0.87	0.99	84.8	Y	1.44	1.51	98.9	Y
17	0.51	0.83	69.5	Y	0.73	0.96	82.6	Y	1.11	1.42	98.3	Y
18	0.45	0.26	9.3	Y	0.38	0.79	63.7*	Y	1.46	1.15	98.6*	Y
19	0.02	0.04	0		0.20	0.17	0		0.45	0.71	51.6	Y
20	0.40	0.46	10.6	Y	0.45	0.70	50.0	Y	0.80	1.21	94.8*	Y
21	0.24	0.31	0.8		0.45	0.45	9.3	Y	0.69	1.02	86.9	Y
22	0.33	0.52	18.7	Y	0.58	0.74	56.8	Y	0.84	1.25	95.8	Y
23	0.01	0.01	0		0.02	0.03	0		0.24	0.35	2.0	Y
24	0.05	0.24	0		0.32	0.36	2.3	Y	0.86	0.78	72.9*	Y
25	0.31	0.43	7.4	Y	0.49	0.82	68.1	Y	0.71	1.15	93.1	Y
26	0.17	0.41	5.6		0.69	0.85	71.9	Y	1.36	1.76	99.7	Y
27	0.37	0.17	2.9		0.30	0.40	4.7	Y	0.57	0.76	59.9	Y
28	0.18	0.20	0		0.43	0.46	10.6		0.79	1.12	65.5	Y
29	0.05	0.18	0		0.06	0.13	0		0.35	0.43	7.4	Y
30	0.06	0.11	0		0.25	0.27	0.2*		0.87	1.07	89.8*	Y
31	0.14	0.45	9.3	Y	0.79	1.37	97.7	Y	1.71	2.54	100.0*	Y
32	0.03	0.12	0		0.17	0.29	0.4		0.41	0.62	35.9	
33	0.33	0.30	1.3		0.40	0.51	17.1		0.50	0.66	42.9	
34	0.08	0.09	0	Y	0.35	0.40	4.7	Y	0.80	1.11	91.6*	Y
35	0.12	0.15	0		0.27	0.39	4.0		0.70	0.67	50.0	
36	0.19	0.23	0		0.30	0.35	2.0		0.51	0.61	34.1	
37	0.16	0.28	0.3		0.51	0.90	77.3	Y	1.31	1.99	99.9*	Y
38	0.25	0.36	2.4	Y	0.51	0.99	84.8	Y	2.11	1.90	100.0*	Y
39	0.04	0.05	0		0.13	0.27	0.2		0.91	1.17	93.7*	Y
40	0.75	1.10	91.1	Y	1.20	1.70	99.6	Y	1.70	2.20	100.0*	Y
41	0.31	0.43	7.4	Y	0.53	0.90	77.3	Y	1.03	1.41	98.2*	Y
42	0.67	0.98	84.1	Y	1.50	1.72	99.6	Y	2.86	3.14	100.00*	Y
43	0.41	0.67	44.8	Y	0.74	1.20	94.6	Y	1.69	2.30	100.00*	Y
44	0.08	0.06	0		0.14	0.20	0		0.35	0.46	10.6	Y
45	0.11	0.13	0		0.22	0.39	4.0		0.51	0.67	44.8*	
46	0.06	0.15	0		0.22	0.32	1.0		0.57	0.76	59.9	
47	0.35	0.25	1.9		0.80	0.92	79.4	Y	1.23	1.42	98.3*	Y
48	0.15	0.36	2.4		0.51	0.79	63.7	Y	0.59	1.15	93.1*	Y
49	0.27	0.29	0.4	Y	0.58	0.51	28.8	Y	1.14	1.73	99.7*	Y
50	0.11	0.22	0	Y	0.43	1.04	88.1	Y	1.49	2.00	100.0	Y

$\Sigma = 553.6$

$\Sigma = 1860.8$

$\Sigma = 3833.8$

$P_f = 553.6/50 = 11.1\%$

$P_f = 1860.8/50 = 37.2\%$

$P_f = 3833.8/50 = 76.7\%$

(1) Y indicates that Turbine Pedestal did impact the operating floor. For all other cases, no impact occurred.

\* Relative diaphragm drift exceeds the limits of applicability of the bilinear force-deflection relationship used for the operating floor so that wall drifts and probability of severe wall distress are likely to be overpredicted to some extent for these cases.



Table 6-2. Comparison of Median and 90% Bounds on Drifts for  $\bar{S}_a = 3.0, 4.0,$   
and 6.0G With and Without Uncertainty on Structure Properties\*

RESPONSE QUANTITY	$\bar{S}_a = 3.0G$		$\bar{S}_a = 4.0G$		$\bar{S}_a = 6.0G$	
	MEDIAN	5% - 95% BOUNDS	MEDIAN	5% - 95% BOUNDS	MEDIAN	5% - 95% BOUNDS
MAX STORY DRIFT (%)	0.26 (0.22)	0.04 - 0.97 (0.05 - 0.67)	0.48	0.10 - 1.71	1.15 (1.33)	0.44 - 2.68 (0.59 - 2.56)
TOP WALL 31 DRIFT (Inches)	0.79 (0.70)	0.20 - 4.12 (0.24 - 2.28)	1.45	0.40 - 7.06	4.2 (5.3)	1.5 - 11.1 (1.8 - 11.8)
OPERATING FLOOR DRIFTS (Inches)	3.10 (3.47)	1.19 - 6.92 (1.60 - 6.65)	4.68	1.87 - 8.96	8.3 (8.8)	3.5 - 16.8 (3.8 - 17.2)

\*Values in parenthesis are for randomness only without uncertainty of structure properties.  
Other values include uncertainty in structure properties.



Table 6-3. Comparison of Fragility Estimates from Extrapolating Results of a Single Median-Centered Elastic Analysis With Results from Multiple Nonlinear Time-History Analyses

PARAMETER	MULTIPLE NONLINEAR ANALYSES	EXTRAPOLATED ELASTIC ANALYSIS
MEDIAN $\bar{S}_a^v$	4.59G	4.39G
RANDOMNESS $\beta_R$	0.23	0.22
UNCERTAINTY $\beta_U$	0.29	0.32
HCLPF $\bar{S}_a$	1.95G	1.77G



Table 6-4. Turbine Building Fragility Estimate Incorporating Additional Variable Parameters

	MEDIAN $\bar{S}_a$ (G) v or F	RANDOMNESS $\sigma_R$	UNCERTAINTY $\sigma_U$	HCLPF $\bar{S}_a$ (G)
NONLINEAR TIME HISTORY RESULTS	4.59G	0.23	0.29	1.95G
MODELLING	1.0	--	0.15	--
DIRECTIONAL EFFECTS	1.0	0.12	--	--
INCOHERENCE OF GROUND MOTION	1.06	0.02	0.06	--
FRAGILITY ESTIMATE	4.87G	0.26	0.33	1.84G



## 7. CONCLUSIONS

### 7.1 Overview of Study

This report has described the results of multiple nonlinear time-history analyses of the primary east-west shear walls of the Diablo Canyon Unit 2 Turbine Building subjected to earthquake ground motion. Plan and schematic elevation views of the Turbine Building with emphasis on these primary east-west shear walls (Walls 19 and 31) are shown in Figures 2-1 and 2-2. The simplified mathematical model used for all nonlinear analyses is shown in Figure 2-3. This model consists of the two shear walls subdivided into three segments (stories) each, the operating floor (E1 140 feet) represented by two beam elements, and the turbine pedestal with a 3.375 inch separation gap between the pedestal and the operating floor beam elements. Model properties including nodal coordinates, masses, element capacities, and stiffnesses are summarized in Tables 2-1 through 2-4, respectively. Elastic modal characteristics of the model are summarized in Table 2-6. Severely pinched and stiffness degrading shear wall hysteretic force-deflection models representing the measured behavior shown in Figure 2-5 were used in this study. The development of the concrete shear wall model and its properties are described in Section 2.



The purposes of the probabilistically based evaluation of the Turbine Building using multiple nonlinear time-history analyses were to:

1. Provide improved probabilistic capacity (fragility) estimates for severe overall distress of the Turbine Building for use in the Seismic-Probabilistic-Risk-Assessment (SPRA) being performed as part of the Long-Term-Seismic-Program (LTSP).
2. Compare the fragility estimate based upon multiple nonlinear analyses with the estimates extrapolated from a single median-centered elastic response spectrum analysis obtained using the standard separation-of-variables fragility evaluation method (References 1 and 2) and recommend improvements to the standard method for use in Diablo Canyon.

As a by-product, this study also provided an improved understanding of the relationship between Turbine Building severe shear wall distress and various earthquake ground motion characteristics.

Fragility estimates for severe distress of the Turbine Building primary east-west shear walls are defined in terms of a single ground motion parameter. The parameter selected was the average 5% damped spectral acceleration,  $\bar{S}_a$ , over the 3 Hz to 8.5 Hz frequency range for the east-



west horizontal component of ground motion. The 25 modified earthquake ground motion time histories listed in Table 3-1 and described in Section 3 were constant amplitude (frequency-independent) scaled to the same  $\bar{S}_a$  value. The average 3 to 8.5 Hz spectral acceleration,  $\bar{S}_a$ , was judged to represent a good ground motion descriptor for the purpose of describing the seismic fragility and convolving the seismic hazard and seismic fragility estimates in the SPRA. All other ground motion characteristics were treated as random variables which contribute to the randomness of the capacity estimate about its median value,  $\frac{V}{\bar{S}_a}$ . It was assumed that the random variability of ground motion characteristics relative to a constant  $\bar{S}_a$  could be defined by the 25 selected time-histories. Figures 3-1 through 3-25 present the 5% damped response spectra for these 25 time-histories, each scaled to  $\bar{S}_a = 3.0g$ . Figure 3-27 presents the mean, median, 84% non-exceedance-probability (NEP), and upper-bound spectra for the ensemble of 25 scaled records for  $\bar{S}_a = 2.25g$ . Within the 3.5 to 10 Hz frequency range, the ratio of 84% NEP to median spectral acceleration is nearly constant at approximately 1.24. The median ratio of  $\bar{S}_a$  to zero period acceleration is 2.16. Additional discussion on the characteristics of these 25 records and the basis for their selection is contained in Section 3.

In addition to the randomness variability of the ground motion characteristics, variability of the structure properties were also



considered in this study. The elastic damping ratio and both the stiffness and strength of each element type (shear walls, operating floor, and turbine pedestal) were each treated as uncertain independent random variables. Severe shear wall distress was expressed in terms of maximum story drift defined as a percentage of the corresponding wall segment height. The maximum story drift limit was treated as a random variable with both randomness and uncertainty. The random variables were assumed to be lognormally distributed with the median values and randomness, uncertainty, and composite logarithmic standard deviations shown below:

VARIABLE	MEDIAN	LOGARITHMIC STANDARD DEVIATION		
		RANDOM	UNCERTAINTY	COMPOSITE
DAMPING	7%	0	0.35	0.35
STIFFNESS FACTOR	1.0	0	0.50	0.50
STRENGTH FACTOR	1.0	0	0.25	0.25
SHEAR WALL DRIFT LIMIT	0.7%	0.15	0.30	0.335

Treatment of uncertainty and randomness variability is described in greater detail in Section 2.6.



First, an elastic response spectrum analysis was performed using the median response spectrum scaled to  $\bar{S}_a = 2.25g$  shown in Figure 3-27 and median structure properties. The results of this analysis are presented in Table 4-1. Based upon this analysis, it was concluded that the lower segment of both Wall 19 and Wall 31 will slightly yield in shear at  $\bar{S}_a = 2.25g$  because the elastic demand to yield capacity (D/C) ratios slightly exceed unity. Based on the median ground spectrum shape and median structure properties, inelastic behavior is expected to initiate at about  $\bar{S}_a = 1.90g$  and  $2.05g$  for the lower segment of Walls 19 and 31, respectively. However, at  $\bar{S}_a = 2.25g$ , with median properties, yielding in the shear walls will be slight and limited to the lowest segment of each wall. With median properties the turbine pedestal is expected to remain elastic up to  $\bar{S}_a = 3.30g$ . The median drift of the turbine pedestal is estimated to be about 1.9 inches at  $\bar{S}_a = 2.25g$ . With median properties, the operating floor is expected to go inelastic at about  $\bar{S}_a = 0.90g$  deforming along the second slope of Figure 2-10. At  $\bar{S}_a = 2.25g$ , the operating floor drift is estimated to be about 2.0 inches. Using a square-root-sum-of-the-squares (SRSS) combination of median estimated pedestal and operating floor drifts, at  $\bar{S}_a = 2.25g$  the gap closure between the pedestal and operating floor was estimated to be about 2.75 inches which was less than the available gap of 3.375 inches. Thus, at  $\bar{S}_a = 2.25g$ , it is not expected that the turbine pedestal will impact the operating floor for the median spectrum shape case. However, by



extrapolation, impacts would be expected to occur for  $\bar{S}_a = 3.0g$ . Such was not confirmed by the nonlinear analysis results, however, since only a small fraction of the nonlinear  $\bar{S}_a = 3.0g$  trials resulted in impact. These elastic analysis results are described in greater detail in Section 4.

Based upon the median-centered elastic analysis at  $\bar{S}_a = 2.25g$ , it was judged that ground motions would have to be scaled to extremely unlikely levels to achieve sufficient shear wall story drifts (0.5% to 1.0% of any segment or story height) for severe shear wall distress to be reasonably likely. Therefore, a total of 200 nonlinear time-history analyses were performed for ground motion in the  $\bar{S}_a = 3.0g$  to  $6.0g$  range (75 analyses each at  $\bar{S}_a = 3.0g$  and  $6.0g$ , and 50 analyses at  $\bar{S}_a = 4.0g$ ) with each of the 25 time histories being used eight times. The nonlinear trials can be thought of as 200 deterministic analyses with varying structural properties and ground motion characteristics. Thus, the results can be cast into either a probabilistic or deterministic framework. This report emphasizes use of the results in developing probabilistic capacity (fragility) estimates for the SPRA; however, discussion of the deterministic implications is also included. For deterministic consideration, the 75 analyses at  $\bar{S}_a = 3.0g$  are the most interesting and will be emphasized. Noting that the highest horizontal ground motion average spectral accelerations ever recorded from actual



earthquakes were only 2.27g and 2.48g for the Tabas records (Records 3 and 4 in Table 3-1) and 2.00g and 1.89g for the Pacoima Dam records (Records 5 and 6 in Table 3-1), average spectral accelerations,  $\bar{S}_a$  greater than 3.0g are sufficiently inconceivable to be of any interest in deterministic studies, and therefore are only considered in a SPRA framework.

The 25 modified time-histories scaled to  $\bar{S}_a = 3.0g$  and  $6.0g$  were applied to the nonlinear structure model using median strength, stiffness, and damping properties. Shear wall, operating floor, and turbine pedestal drifts computed from each of these analyses are summarized in Tables 5-1 and 5-2 for  $\bar{S}_a = 3.0g$  and  $6.0g$ , respectively. The results are discussed in Section 5 and summarized in subsequent subsections of this Conclusion Section.

Next, a set of 50 nonlinear structure model properties were randomly selected using the previously defined lognormally distributed structure property random variables. The 50 trial sets of properties used are tabulated in Table 2-7. For each trial, the median stiffnesses and strengths of the shear walls, operating floor, and turbine pedestal were multiplied by probabilistic defined stiffness and strength ratios. Stiffness and strength ratios were independently defined for each element type (shear walls, operating floors, and turbine pedestals).



Thus, for example in trial 6 the shear wall stiffnesses are a factor of 3.1 times as great as their median stiffnesses while their strengths are only 66% as great as their median strengths. In this same Trial 6, the operating floor stiffness is only 66% of its median value while its strength is 132% of its median value. Elastic damping was also varied for each trial and the values used are also shown in Table 2-7. For Trial 6, damping was 5.8%, but ranged from 3.3% to 15% over the 50 trials.

The 25 earthquake ground motion records were used twice at each  $\bar{S}_a$  level in combination with the 50 sets of nonlinear structure properties. All records were used once, in order, for the first 25 trials, and then were repeated in the same order for the next 25 trials. Thus, Record 1 was used in Trials 1 and 26; Record 10 in Trials 10 and 35; etc. The 50 sets of structural properties and the time-history record order were retained for the nonlinear analyses performed at  $\bar{S}_a = 3.0g, 4.0g,$  and  $6.0g$ . Maximum shear wall story drift results for each of these 150 analyses (50 trials each at  $\bar{S}_a = 3.0g, 4.0g,$  and  $6.0g$ ) are presented in Table 6-1, discussed in Section 6, and summarized in subsequent subsections of this Conclusion Section.

Accordingly, three sets of 25 deterministic nonlinear analyses were performed using each of the 25 time-histories as input at  $\bar{S}_a = 3.0g$ .



One analysis set was performed using median structural properties while the other two analysis sets were performed using the variable properties specified in Table 2-7. The specified properties cover the full credible range of structure stiffness, strength, and damping. Thus, the deterministic analyses at  $\bar{S}_a = 3.0g$  with varied ground motion and varied properties were used to understand the sensitivity of the turbine building shear wall drifts to ground motion characteristics and variation in structure properties. Thus, deterministic capacity estimates are made which fully incorporate ground motion and structure property variation sensitivities.

7.2 Primarily Deterministic Observation on the Influence of Structure Property and Ground Motion Variation on Shear Wall Drifts

The nonlinear analysis results are summarized in Tables 5-1, 5-2, 6-1, and 6-2 and Figures 5-2 and 6-2 through 6-7 and discussed in Sections 5.1, 5.3, 6.1, 6.4 and 6.5 of this report. These clearly indicate that for constant  $\bar{S}_a$ , the maximum shear wall drifts are highly variable. Therefore, by itself  $\bar{S}_a$  does not serve as an accurate estimator of the maximum shear wall drift. No other single ground motion parameter is likely to do much better, although it is possible that averaging the spectral acceleration over a broader frequency range from about 1.7 Hz to 9.5 Hz may have been an improvement to averaging over the 3 to 8.5 Hz



range. The largest source of drift variation for a constant  $\bar{S}_a$  comes from the variation in ground motion characteristics of different records having the same  $\bar{S}_a$ .

The variation in maximum shear wall story drift due to variation in ground motion characteristics only is illustrated by the 25 nonlinear analyses performed both at  $\bar{S}_a = 3.0g$  and  $\bar{S}_a = 6.0g$  with median (non-varying) structure properties. Figure 5-2 and the parenthetical results in Table 6-2 illustrate the drift variation due to the variation in ground motion characteristics only. At  $\bar{S}_a = 3.0g$ , 3 of the 25 trials (12%) produced maximum story drifts in the range of 0.5% to 0.7% of the story height, while at  $\bar{S}_a = 6.0g$ , 7 of the 25 trials (28%) produced maximum story drifts in the 0.5% to 1.0% range.

The range of 0.5% to 1.0% maximum story drifts are of the greatest interest because at story drifts below 0.5% severe shear wall damage is reasonably unlikely, while above 1.0% severe shear wall damage is reasonably likely. Yet 3 out of 25 ground motion records anchored at  $\bar{S}_a = 3.0g$  produced drifts within this range while 7 out of 25 ground motion records anchored at  $\bar{S}_a = 6.0g$  also produced drifts which did not exceed this range. Thus, within the  $\bar{S}_a$  range of 3.0 to 6.0g there is substantial randomness to the expected performance of the Turbine Building shear walls. Some records anchored at  $\bar{S}_a = 3.0g$  are potentially capable of producing severe distress to the shear walls,



while other records anchored at  $\bar{S}_a = 6.0g$  might not produce severe distress.

Table 6-2 shows that even with median structure properties, the 90% bounds (5% to 95%) on maximum story drift at  $\bar{S}_a = 3.0g$ , ranges from 0.05% to 0.67%, while at  $\bar{S}_a = 6.0g$  the 90% bounds on maximum story drift ranges from 0.59% to 2.56%. With median structure properties, only 11 of the 25 ground motion records produced maximum story drifts in excess of 0.25% at  $\bar{S}_a = 3.0g$ . It is inconceivable that maximum story drifts as low as 0.25% could produce severe shear wall distress. Thus, at  $\bar{S}_a = 3.0g$ , 56% (14 out of 25) of the records are incapable of even conceivably producing severe damage to the turbine building shear walls when median strength and stiffness properties are used. On the other hand, at  $\bar{S}_a = 3.0g$ , 12% (3 out of 25) of the records produced damage probabilities ranging from 12 to 46% of severely damaging the Turbine Building shear walls even when median structure properties are used. Clearly it is important to better understand the ground motion characteristics which produce large shear wall drifts in the Turbine Building.

Even though the Turbine Building shear wall drifts for a specified  $\bar{S}_a$  level are primarily influenced by ground motion characteristics, uncertainty in structural properties also play an important, but clearly lesser, role on the variability of the computed drifts. As shown in



Table 6-2, the 90% bounds on shear wall drifts increase when structure properties are randomly varied within their range of uncertainty. For instance, at  $\bar{S}_a = 3.0g$  the 90% bounds (5% to 95%) on maximum story drift as a percentage of story height increases from 0.05% to 0.67% with median structure properties to 0.04% to 0.97% when structure property variation is included. With structure property variation, still 50% (25 out of 50) of the trials produced maximum story drifts less than 0.25% at  $\bar{S}_a = 3.0g$  and so are incapable of even conceivably producing severe damage to the Turbine Building shear walls. Only 16% (8 out of 50) of the trials produced maximum story drifts in excess of 0.5%. Thus, the percentage of trials which produced drifts capable of severely damaging the Turbine Building shear walls is only slightly greater when uncertain structure property variation is considered. The substantially largest source of variability of shear wall drifts comes from ground motion variation and not from uncertainty in structure properties. Therefore, differences of opinion over structural strength, stiffness, and damping properties are relatively unimportant compared to variability in ground motion characteristics.

The nonlinear trials reported in Section 6 which include structure property variation indicate that the variation of certain structure properties influence maximum shear wall drift while the variation of others do not seem to have any discernible influence on maximum drift.



Strengths were varied from less than 60% to over 160% of their median values, while stiffnesses were varied from less than 40% to over 300% of their median values. Figures 6-4 through 6-7 illustrate that no discernible trend exists between maximum story drift and the strength or stiffness properties used for either the operating floor or the turbine pedestal. However, as would be expected, the strength and stiffness properties of the shear walls did influence the calculated maximum story drifts, as shown in Figures 6-2 and 6-3.

For  $\bar{S}_a = 3.0g$ , Figure 6-2 illustrates that the 8 trials with maximum story drifts in excess of 0.5% were all associated with shear wall stiffness ratios less than 1.25. Conversely, for the five trials with shear wall stiffness factors greater than 2.2, the maximum story drift never exceeded 0.33% irrespective of the ground motion record used. Similarly, Figure 6-3 illustrates that the eight trials with maximum story drifts in excess of 0.5% also correspond to shear wall strength ratios less than 1.0. Conversely, the 12 trials with shear wall strength ratios in excess of 1.16 all produced maximum story drifts less than 0.37%.

Thus, irrespective of the ground motion record, maximum story drifts in excess of 0.5% only occurred at  $\bar{S}_a = 3.0g$  when:



1. The shear wall stiffness ratio was less than 1.25, and
2. The shear wall strength ratio was less than 1.0.

However, even more importantly, large story drifts in excess of 0.4% only occurred when certain ground motion characteristics (described later) were exceeded. Therefore, all three conditions (ground motion characteristics exceeding certain limits, lower than median strength shear walls, and lesser stiffness shear walls) had to be met for maximum story drifts to exceed 0.5%, and thus for severe damage to the Turbine Building shear walls to be likely, from a ground motion with  $\bar{S}_a = 3.0g$ .

Figure 6-1 illustrates that the elastic damping levels selected for the nonlinear analyses (ranging from 3% to 12%) had no discernible influence on the maximum story drifts reached. Essentially, elastic damping is an unimportant structural parameter at least so far as maximum drift is concerned for structures which drift substantially into the inelastic range. Energy dissipation within such structures is dominated by the hysteretic loop within the nonlinear force-deflection relationship used in the nonlinear analysis and elastic damping becomes rather irrelevant.



As noted earlier, the most dominant variable influencing the maximum story drift reached for a given  $\bar{S}_a$  level pertained to certain detailed characteristics of the ground motion. Specifically, it was found that to produce large story drifts within the shear walls, the ground motion must have broad frequency content. High spectral acceleration was required within the elastic frequency range of the shear walls (i.e., within the 8.6 to 9.5 Hz frequency range) in order to initiate substantial inelastic drift. In addition, high spectral acceleration was also required in the 1.7 to 2.8 Hz frequency range in order to drive the shear walls to drift levels associated with the onset of severe distress.

In no case did the maximum story drift exceed 0.4%, even when structure properties were varied within the broad ranges considered in this study, unless the 5% damped spectral accelerations of the ground motion exceeded both of the following limits.

#### HCLPF Limits

##### High Frequency Limit

$$\text{Max. } S_{a_{5\%}} \leq 1.6g \text{ within 8.6 to 9.5 Hz Range}$$

and

(7-1)



Low Frequency Limit

$$\text{Max } S_{a5\%} \leq 2.8g \text{ within } 2.4 \text{ to } 2.8 \text{ Hz Range}$$

or

$$\text{Max } S_{a5\%} \leq 2.25g \text{ within } 1.7 \text{ to } 2.0 \text{ Hz Range}$$

Thus, there is high-confidence-of-a-low-probability-of-failure (HCLPF) of the Turbine Building shear walls unless both the above high frequency and low frequency limits are not met.

With median structure properties, it was necessary to exceed these limits by at least a factor of 1.3 to produce maximum story drifts in excess of 0.25%. Thus, with median structure properties, 1.3 times these limits would preclude any possibility of severe shear wall distress. The above limits incorporate the unlikely combination of both substantially lower than median shear wall stiffness and lower than median shear wall strength.

The combination of having to exceed both limits of Equation 7-1 provides the most appropriate explicit deterministic description of the HCLPF ground motion level for the Turbine Building. A HCLPF statement can be



more accurately made by requiring the exceedance of both the high and low frequency limits of Equation 7-1 as opposed to defining the HCLPF capacity in terms of a single ground motion parameter such as  $\bar{S}_a$ . However, for use in the SPRA, the Turbine Building probabilistic capacity (fragility) and HCLPF capacity are defined in terms of  $\bar{S}_a$  for ease of convolving the seismic fragility and the seismic hazard estimates and for ease of combining the Turbine Building capacity estimate with capacity estimates of the other important structures and components. This process introduces greater uncertainty and thus a lower and more conservative HCLPF capacity estimate when the single parameter  $\bar{S}_a$  is used.

It should be noted that of the original, unmodified ground motion records used in this study (Table 3-1), only the Pacoima Dam records (Records 5 and 6) exceed the limits of Equation 7-1. None of the other unmodified records have exceeded these limits. The seismic risk to the Turbine Building shear walls comes primarily from hypothetically postulated horizontal earthquake-induced ground motion components with spectral amplitudes substantially greater than have ever been recorded anywhere in the world.



The unmodified Tabas records (Records 3 and 4 in Table 3-1) had the highest  $\bar{S}_a$  of 2.27 g and 2.48 g, respectively. Thus, in terms of  $\bar{S}_a$  alone, these records might appear to be potentially damaging. However, the Tabas records require upward scaling by factors of 1.67 and 1.23 for Records 3, and 4, respectively, before the HCLPF limits of Equation 7-1 are reached. The six (6) nonlinear analyses using these records scaled to  $\bar{S}_a = 3.0g$ , resulted in maximum story drifts ranging from 0.04% to 0.23% (no potential for damage). Even when scaled to  $\bar{S}_a = 4.0g$ , the Tabas records produced maximum story drifts ranging from 0.13% to 0.46% (some potential for severe damage). Thus, it would seem that the Tabas records would have to be scaled upward to average spectral accelerations of between 3.0 and 4.0g before becoming even potentially severely damaging to the Turbine Building shear walls. This would suggest that the HCLPF limits of Equation 7-1 might be too conservative.

The unmodified Pacoima Dam Records (Records 5 and 6 in Table 3-1) had the second highest  $\bar{S}_a$  of 2.00g and 1.89g, respectively. Both unmodified records exceed the HCLPF limits of Equation 7-1 by less than 10% and these were the only two unmodified records which exceeded those limits. Even so, when the Pacoima Dam records were scaled upward by a factor of approximately 1.5 to produce  $\bar{S}_a = 3.0g$ , the six (6) nonlinear trials using these records produced maximum story drifts ranging from 0.04% to 0.45%. Thus, it appears that the Pacoima Dam records must be scaled



upward by a factor approaching 1.5 before they exhibit a reasonable likelihood of severely damaging the Turbine Building shear walls. Thus, the HCLPF limits of Equation 7-1 appear to be too conservative for the Pacoima Dam records.

The unmodified Gazli records (Records 1 and 2) require upward scaling by factors of 2.0 and 1.28, respectively, before reaching the HCLPF limits of Equation 7-1. When scaled upward by approximately 2.3 to produce  $\bar{S}_a = 3.0g$ , the 6 trials using these two records produced drifts ranging from 0.18% to 0.45%. Thus, it would appear that the Gazli records must be scaled upward by at least a factor of 2.0 to have a reasonable likelihood of severely damaging the turbine building. Thus, the HCLPF limits of Equation 7-1 also appear to be somewhat too conservative for the Gazli records.

All of the other unmodified actual records require upward scaling by more than a factor of 2.0 before even reaching the HCLPF limits of Equation 7-1. As recorded, these records can't conceivably be severely damaging to the turbine building unless they are scaled upward by a factor close to at least 2.0. As noted in Section 3, Records 7 through 25 (note that Records 22 through 25 are synthetic records) were all scaled substantially upward in amplitude to achieve  $\bar{S}_a = 3.0g$ . In addition, Records 10 through 17 were frequency modified, for the reasons



discussed in Section 3, in order to more closely approximate ground motion at the Diablo Canyon site subjected to a magnitude of 6.5 to 7.5 earthquake on the Hosgri fault.

At  $\bar{S}_a = 3.0g$ , Records 15, 17, 18, and 20 consistently produced the highest shear wall story drifts. None of these records was directly applicable for the Diablo Canyon conditions. Records 18 and 20 were recorded at too great a distance, Record 17 was associated with too low a magnitude, and Record 15 was associated with both too low a magnitude and too great a distance. Both records 15 and 17 required frequency-dependent scaling which enhanced low frequency content. It should be noted that the four highest drifts from the 50 trials at  $\bar{S}_a = 3.0g$  with uncertain structural properties came from the four trials which used Records 15 and 17. This result was significantly influenced by the enhancement of low frequency content in these two records.

Inclusion of Records 15, 17, 18, and 20 had a very substantial influence on the probabilities of severe shear wall distress estimated at  $\bar{S}_a = 3.0$  and 4.0g. At  $\bar{S}_a = 3.0g$  including all 25 equally weighted records, it was estimated that the composite probability of severe shear wall distress was about 11%. If Records 15, 17, 18, and 20 had been deleted, this probability would have been reduced by a factor of about 2.75 to about 4%. If only the trials which used Records 1 through 6 had been



considered, the probability of severe shear wall distress would have been further reduced to about 2.4%. If only the trials which used Tabas and Pacoima Dam (Records 3 through 6) had been considered, the probability of severe shear wall distress would have been reduced to about 1.3%. Thus, the inclusion and equal weighting of all 25 records rather than just using the four most directly applicable records from Tabas and Pacoima Dam appears to have increased the reported probability of failure at  $\bar{S}_a = 3.0g$  by a factor of as much as 8.5.

Similarly, the deterministic HCLPF limits of Equation 7-1 are most heavily influenced by the nonlinear analyses which used Records 13, 15, and 17. Again, all three of these records required frequency modification and substantial upward scaling to more closely approximate ground motion at the Diablo Canyon site subjected to magnitude 6.5 to 7.5 earthquakes on the Hosgri fault. If trials which used these three records were deleted, the deterministic HCLPF limits of Equation 7-1 could be increased resulting in a less conservative bias for the Gazli, Tabas and Pacoima Dam records (Records 1 through 6).

In summary, the results reported in this study are very substantially influenced in a conservatively biased manner by the decision to include and equally weight all 25 records listed in Table 3-1 with each scaled to the same  $\bar{S}_a$ . This statement is particularly true for the



probabilistic results used in the SPRA, but is also true to a lesser extent for the HCLPF limits of Equation 7-1.

7.3 Observation on Potential for Impact Between Turbine Pedestal and Operating Floor

It was found that the turbine pedestal and operating floor consistently tended to move at least partially in-phase even though they had slightly different elastic natural frequencies (3.1 Hz for the turbine pedestal, and 4.0 Hz for the operating floor when median stiffness properties were used). The potential for impact is consistently severely overpredicted when operating floor and turbine pedestal drifts are combined probabilistically using the SRSS combination rule. In fact, in no case did impacts occur unless the operating floor drift alone exceeded the available gap of 3.375 inches. For trials in which the ratio of operating floor drift to gap size ranged between 1.0 and 1.67, impacts occurred in only about two-thirds of the cases. Thus, until operating floor drifts exceeded 1.67 times the gap size, impact was not certain. Basically, turbine pedestal drift reduced the possibility of impacts. The operating floor tends to drift more than the turbine pedestal and in the same direction as the turbine pedestal. When impacts did occur, the turbine pedestal tended to restrain the operating floor from further drifts, rather than additionally loading the operating floor. These analyses produce no evidence that the presence of the very heavy turbine



pedestal could result in additional distress to the shear walls due to impact with the operating floor. On the contrary, if the pedestal impact has any influence on the shear walls, there is some evidence that the turbine pedestal might actually help restrain the shear walls from excessive drifts to a slight extent.

At  $\bar{S}_a = 3.0g$ , operating floor impact with the turbine pedestal occurred in 36% of the trials. These percentages increased to 58% and 84% at  $\bar{S}_a = 4.0g$  and  $6.0g$ , respectively. Based upon an extrapolation of operating floor and turbine pedestal drifts down to  $\bar{S}_a = 2.25g$ , it is estimated that at  $\bar{S}_a = 2.25g$  impacts would occur for Trials 31, 40, 42, and 43 and possibly for Trials 22 and 25. On this basis, it is estimated that there is about an 8% to 12% probability of impact at  $\bar{S}_a = 2.25g$ . In other words, at  $\bar{S}_a = 2.25g$ , impact is unlikely, but possible. The consequences of such impact are judged to be negligible even if it occurs.

#### 7.4 Probabilistic Capacity (Fragility) Estimates Resulting From Nonlinear Analyses

The maximum story drifts tabulated in Tables 5-1, 5-2, and 6-1 from each of the nonlinear analyses were compared with the lognormally distributed shear wall drift limits tabulated in Section 7-1 and discussed in Section 2.1.3. Using these probabilistically defined shear wall drift



limits, the probability of severe wall distress was computed for each of the nonlinear analyses. These computed probabilities are also tabulated in Tables 5-1, 5-2 and 6-1.

The nonlinear analysis based maximum story drifts for the median structural model trials tabulated in Tables 5-1 and 5-2 include only randomness introduced by ground motion variability. These maximum story drifts were compared to the probabilistic shear wall drift limits which included an estimate of only randomness variability (i.e., randomness logarithmic standard deviation,  $\beta_R = 0.15$ ). Thus, the probabilities of severe shear wall distress tabulated in Tables 5-1 and 5-2 for median structural properties include only sources of randomness variability.

The nonlinear analysis based maximum story drifts tabulated in Table 6-1 include the effects of both randomness variability of the ground motion plus uncertainty in structural properties. These maximum story drifts were compared to the probabilistic shear wall drift limits which included an estimate of both randomness and uncertainty variability in drift limits (i.e., composite logarithmic standard deviation,  $\beta_C = 0.335$ ). Using  $\beta_C$ , the probability of severe shear wall distress is estimated as:



MAXIMUM STORY DRIFT	COMPOSITE PROBABILITY OF SEVERE SHEAR WALL DISTRESS $P_F$
0.25%	0%
0.50%	16%
0.70%	50%
1.00%	84%
2.00%	100%

The basis for selecting these probabilities of severe distress versus maximum story drift is discussed in Section 2.1.3. The resultant probabilities of severe shear distress tabulated for each nonlinear trial in Table 6-1 are composite probabilities (i.e., probabilities which include both sources of randomness variability and estimates of uncertainty or ignorance).

The overall probability of severe shear wall distress,  $P_F$ , was obtained for each case studied (Randomness Only at  $\bar{S}_a = 3.0g$  and  $6.0g$ , and Randomness Plus Uncertainty at  $\bar{S}_a = 3.0g$ ,  $4.0g$ , and  $6.0g$ ) by summing the individual  $P_F$  estimates for each trial and dividing this sum by the number of trials in accordance with Equation 5-1. The overall



probability estimates for each case studied are also presented in Tables 5-1, 5-2 and 6-1. These results were then fit by a "best-fit" lognormally distributed fragility estimate using linear regression (least square error fitting). The result is a lognormally distributed fragility estimate defined in terms of the median  $\bar{S}_a^v$ , and logarithmic standard deviations for randomness,  $\beta_R$ , composite,  $\beta_C$ , and uncertainty,  $\beta_U$ , variability. Also, the High-Confidence-Low-Probability-of-Failure (HCLPF) estimate of  $\bar{S}_a$  appropriate for comparison with median input spectra was back-calculated using Equation 6-2. The resulting estimates are:

#### Turbine Building Fragility Estimate

$$\text{Median } \bar{S}_a^v = 4.59g$$

$$\beta_C = 0.37$$

$$\beta_R = 0.23$$

$$\beta_U = 0.29$$

$$\text{HCLPF } \bar{S}_a = 1.95g$$

Based upon a lognormal distribution with the parameters defined above the probability of severe wall distress is estimated as follows:



$\bar{S}_a$ (G)	RANDOMNESS ONLY	RANDOMNESS + UNCERTAINTY
	MEDIAN $P_F$ (%)	COMPOSITE $P_F$ (%)
3.0	3.2 (3.1)	12.5 (11.1)
4.0	27.7	35.5 (37.2)
6.0	87.8 (87.6)	76.5 (76.7)

This table also shows in parentheses the probabilities of severe wall distress actually estimated from the multiple nonlinear time-history analyses. The fit is considered acceptable. However, three sources of variability and conservatism were not treated in the nonlinear time history analyses and must be included using the normal separation-of-variables approach. These are:

1. Modelling Uncertainty
2. Earthquake Component Variation
3. Ground Motion Incoherence

These sources of additional variability and conservatism are discussed and their effects are judgmentally estimated in Section 6.3. Their effect on the estimated fragility parameters are given in Table 6-4.



Their combined effect is estimated to increase the median  $\bar{S}_a^v$  to 4.87g (6% increase) and to reduce the HCLPF  $\bar{S}_a$  to 1.84g (6% reduction) due to increased randomness and uncertainty variability. The final fragility estimate defined in Table 6-4 which incorporates these additional effects was used in the SPRA.

It should be clearly noted again that the probabilistic drift estimates, estimates of probability of severe shear wall distress at any  $\bar{S}_a$ , and the resultant fragility estimate summarized in Table 6-4 are all heavily influenced by the selection and equal weighting of the 25 time histories used in this study. As noted in Section 7.2, the estimated  $P_F$  of 11.1% at  $\bar{S}_a = 3.0g$  for combined Randomness and Uncertainty would be reduced to 1.3% (more than an eight-fold reduction) if only trials which used the Pacoima Dam and Tabas records were considered. Furthermore, the  $P_F$  of 3.1% at  $\bar{S}_a = 3.0g$  for Randomness only would be reduced to zero if trials using Records 15, 18, and 20 were ignored. Inclusion of Records 15 and 17, and to a lesser extent Records 13, 18, and 20 resulted in a slight reduction in the estimated median  $\bar{S}_a^v$ , a moderate increase in  $\beta_R$ , and a substantial increase in  $\beta_U$ . The net result is a substantial reduction in the estimated HCLPF  $\bar{S}_a$  capacity. All of these records required substantial upward scaling to produce  $\bar{S}_a = 3.0g$ . In addition, Records 13, 15, and 17 required frequency-dependent modification to make them more appropriate for the



Diablo Canyon site. It is possible that the results using Records 3 through 6 should be substantially more heavily weighted while the results from Records 7 through 25 are less heavily weighted; this is particularly so for Records 10 through 17 which were frequency modified. If such weighting had been done, the Turbine Building HCLPF  $\bar{S}_a$  capacity given in Table 6-4 would have been substantially increased. The fragility estimate presented in Table 6-4 may be conservatively biased because of the equal weighting of all ground motion records. In particular, both  $\beta_R$  and  $\beta_U$  may be too large.

#### 7.5 Prediction of Fragility From a Single Median Centered Elastic Analysis

Nonlinear time-history analysis results are not usually available from which to estimate the fragility. In such cases, the median fragility is normally estimated from an elastic analysis using the median input spectrum shape. Logarithmic standard deviations  $\beta_R$ ,  $\beta_U$ , and  $\beta_C$  are estimated by first estimating the logarithmic variances ( $\beta^2$ ) associated with each parameter influencing the fragility (capacity). Treating each parameter influencing the fragility as a separate independent random variable, the logarithmic variances are summed to obtain the overall  $\beta_R^2$ ,  $\beta_U^2$ , and  $\beta_C^2$  estimates. This process is called the separation-of-variables approach to estimation of fragility and is described in References 1 and 2. This is the approach which has been used to develop



fragilities for most SPRA studies and is the approach used to estimate the fragilities of the other important Diablo Canyon civil structures. Therefore, the adequacy of this approach to approximate the fragility estimates obtained from multiple nonlinear analyses was studied and the results are presented in Sections 5.2 and 6.2.

It was found that so long as the Inelastic Energy Absorption Capability factor,  $F_{\mu}$ , is estimated by the procedures defined in Section 5.2, the fragility estimated from multiple nonlinear analyses can be slightly conservatively approximated by a separation-of-variables extrapolation of a single median-centered elastic response spectrum analysis using the median input spectrum shape. Table 6-3 presents a comparison of the fragility parameters,  $\bar{S}_a^v$ ,  $\beta_R$ ,  $\beta_U$ , and HCLPF  $\bar{S}_a$  estimated by extrapolating a single elastic analysis versus those obtained from the multiple nonlinear time history analyses. It is shown in Table 6-3 that the extrapolated elastic analysis median  $\bar{S}_a^v$  is about 5% too low, the uncertainty  $\beta_U$  is about 10% too large, and the HCLPF  $\bar{S}_a$  which results is about 10% too low. This slight conservatism is a minor penalty when compared to the great simplification introduced by being able to extrapolate the results of a single median-centered elastic analysis.

The key to making an inelastic fragility estimate from a median-centered elastic analysis is to obtain a realistic estimate of the Inelastic



Energy Absorption Capability,  $F_u$ . It was found that the Spectral Averaging Method defined in NUREG/CR-3805, Volume 1 (Reference 4), provided an excellent estimate of  $F_u$  over a broad range of maximum story drifts from 0.22% to 1.33% as shown in Table 5-5. It was also found that the more commonly used Riddell-Newmark Method (Reference 6) provided too liberal of an estimate for  $F_u$  for this nonlinear Turbine Building model. This same conclusion was reached in Reference 4 for other cases as well. However, when modified into an Effective Riddell-Newmark Method as described in Section 5.2, the method provided equally good estimates of  $F_u$  as did the Spectral Averaging Method, and is easier to use.

Details on the Spectral Averaging Method and the Effective Riddell-Newmark Method for estimating  $F_u$  are presented in Section 5.2. Details on estimating  $\beta_R$  by the separation-of-variables approach are also contained in Section 5.2, while details on estimating  $\beta_U$  are contained in Section 6.2.

It is concluded that the fragility results obtained from the nonlinear analyses presented herein provide reasonable validation of the separation-of-variables approach used to estimate fragilities of other civil structures in the Diablo Canyon SPRA. It is recognized that this conclusion requires that a reasonable estimate of the nonlinear deformed shape is made.



## 8. REFERENCES

1. Kennedy, R.P., et al., "Probabilistic Seismic Safety Study of an Existing Nuclear Power Plant", Nuclear Engineering and Design, Vol. 59, No. 2, pp. 315-318, August 1980.
2. Kennedy, R.P., and M.K. Ravindra, "Seismic Fragilities for Nuclear Power Plant Risk Studies", Nuclear Engineering and Design, Vol. 79, No. 1, pp. 47-68, May 1984.
3. Newmark, N.M., R.P. Kennedy, and S.A. Short, "Final Report Evaluation of a Typical PWR Reactor Building Subjected to a High Acceleration, Short Duration Earthquake", Nathan M. Newmark Consulting Engineering Services and Engineering Decision Analysis Company, Inc., August, 1979.
4. Kennedy, R.P., S.A. Short, K.L. Merz, F.J. Tokarz, I.M. Idriss, M.S. Power, and K. Sadigh, "Engineering Characterization of Ground Motion, Task I: Effects of Characteristics of Free-Field Motion on Structural Response", NUREG/CR-3805, Vol. 1, Prepared for U.S. Nuclear Regulatory Commission, May, 1984.
5. Kennedy, R.P., R.H. Kincaid, and S.A. Short, "Engineering Characterization of Ground Motion, Task II: Effects of Ground Motion Characteristics on Structural Response Considering Localized Structural Nonlinearities and Soil-Structure Interaction Effects", NUREG/CR-3805, Vol. 2, Prepared for U.S. Nuclear Regulatory Commission, March, 1985.
6. Riddell, R. and N.M. Newmark, "Statistical Analysis of the Response of Nonlinear Systems Subjected to Earthquake", SRS 468, Department of Civil Engineering, University of Illinois, August, 1979.
7. Barda, F., J.M. Hanson, and W.G. Corley, "Shear Strength of Low-Rise Walls with Boundary Elements", ACI Symposium, Reinforced Concrete Structures in Seismic Zones, SP-53, ACI, Detroit, Michigan, 1976.
8. Shiga, T., A. Shibata, and J. Tabahashi, "Experimental Study on Dynamic Properties of Reinforced Concrete Shear Walls", 5th World Conference on Earthquake Engineering, Rome, Italy, 1973.
9. Cardenas, A.E., et al., "Design Provisions for Shear Walls", ACI Journal, Vol. 70, No. 3, March, 1973.



10. Oesterle, R.G., et al., "Earthquake Resistant Structural Walls - Tests of Isolated Walls - Phase II", Construction Technology Laboratories (Division of PCA), Skokie, Illinois, October, 1979.
11. Corley, W.G., A.E. Fiorato, and R.G. Oesterle, "Structural Walls", Significant Developments in Engineering Practice and Research, SP-72, American Concrete Institute, pp. 77-131, 1981.
12. Ferritto, J.M., "An Economic Analysis of Earthquake Design Levels", Naval Civil Engineering Laboratory, TN-1640, July, 1982 and TN-1671, July, 1983.
13. Shiga, T., "Hysteretic Behavior of Reinforced Concrete Shear Walls", Proc. US-Japan Cooperative Research, The Safety of School Buildings, Hawaii, 1975.
14. Endebrock, E.G., Preliminary Report, Category I Program, FY 83, Los Alamos National Laboratory.
15. Fiorato, A.E. and W.G. Corley, "Laboratory Tests of Earthquake-Resistant Structural Wall Systems and Elements", Workshop on Earthquake-Resistant Reinforced Concrete Building Construction, University of California, Berkeley, pp. 1388-1429, July, 1977.
16. Park, R. and T. Paulay, Reinforced Concrete Structures, John Wiley and Sons, New York, pp. 610-662, 1975.
17. Paulay, T., "Earthquake Resistant Structural Walls", Workshop on Earthquake-Resistant Reinforced Concrete Building Construction, University of California, Berkeley, pp. 1339-1365, July, 1977.
18. Alexander, C.M., A.C. Heiderbrecht, and W.K. Tso, "Cyclic Load Tests on Shear Wall Panels", Proceedings of the Fifth World Conference on Earthquake Engineering, Rome, pp. 1116-1119, 1973.
19. Wang, T.Y., V.V. Bertero, and E.P. Popov, "Hysteretic Behavior of Reinforced Concrete Framed Walls", Report No. EERC 75-23, EERC, University of California, Berkeley, 1975.
20. Bertero, V.V., et al., "Seismic Design Implications of Hysteretic Behavior of R/C Structural Walls", Proceedings of the Sixth World Conference on Earthquake Engineering, New Delhi, 1977.



21. Popov, E.P., "Update on Simulated Seismic Tests on Reinforced Concrete and Structural Steel Assemblies", Proceedings of the 1980 Annual Convention of the Structural Engineering Association of California, Monterey, pp. 15-35, October, 1980.
22. Umemura, H. and H. Tanaka, "Elasto-Plastic Dynamic Analysis of Reactor Buildings", Proceedings of the Sixth World Conference on Earthquake Engineering, New Delhi, India, pp. 8-51/8-56, 1977.
23. Umemura, H. et al., "Restoring Force Characteristics of R.C. Walls with Openings and Reinforcing Methods", Proceedings of the Seventh World Conference on Earthquake Engineering, Istanbul, pp. 209-216, 1980.
24. Uchida, T. and H. Tanaka, "Structural Test and Analysis on the Seismic Behavior of the Reinforced Concrete Reactor Building", Proceedings of the Seventh World Conference on Earthquake Engineering, Istanbul, pp. 217-224, 1980.
25. Fukada, Y., S. Hirashima, and R. Shobara, "Experimental Study on One-Thirtieth Scale Model of Reinforced Concrete Reactor Building Under Cyclic Lateral Loading", Trans. Sixth International Conference of Structural Mechanics in Reactor Technology, Volume K, paper K15/1, August, 1981.
26. Banon, H., J.M. Biggs, and H.M. Irvine, "Seismic Damage in Reinforced Concrete Frames", Journal Structural Division, ASCE, Vol. 107, ST 9, pp. 1713-1729, September, 1981.
27. Saïidi, M. and M.A. Sozen, "Simple and Complex Models for Nonlinear Seismic Response of Reinforced Concrete Structures", Civil Engineering Studies, Structural Research Series, No. 465, University of Illinois, Urbana, August, 1979.
28. Kanaan, A.E., and G.H. Powell, "DRAIN-2D, General Purpose Computer Program for the Dynamic Analysis of Inelastic Plane Structures", EERC Report No. 73-6, Earthquake Engineering Research Center, University of California, Berkeley, April, 1973 (Revised 1975).
29. Powell, G.H., "DRAIN-2D Users Guide", University of California, Berkeley, California, August, 1975.
30. Letter from Bimal Sarkar to D.A. Wesley transmitting data for nonlinear analysis of turbine building dated October 31, 1986. QA Document Number 34001.01 M-437.



Table 2-6. Elastic Modal Properties of the Turbine Building Model with Median Structure Properties

A) MODAL FREQUENCIES

MODE	NATURAL FREQUENCY (HZ)	REMARKS
1	3.1	TURBINE PEDESTAL
2	4.0	OPERATING FLOOR
3	8.6	MALL AT LINE 31
4	9.5	MALL AT LINE 19

B) MODAL SHEARS & MOMENTS

ELEMENT	MODAL SHEARS (KIPS/G)					MODAL MOMENTS (KIP-FT./G)				
	MODE 1	MODE 2	MODE 3	MODE 4	TOTAL HIGHER MODES	MODE 1	MODE 2	MODE 3	MODE 4	TOTAL HIGHER MODES
TURBINE PEDESTAL	25,000	--	--	--	--	--	--	--	--	--
MALL 19										
OPERATING FLOOR (PER BEAM)	--	1410	-20	-260	0	--	--	--	--	--
EL 123+	--	3470	-390	3870	-420	--	89,000	-7,000	65,000	-7,000
EL 104+	--	3550	-430	4360	-160	--	126,000	-15,000	148,000	-10,000
EL 85+	--	3600	-460	4740	1010	--	195,000	-24,000	238,000	9,000
MALL 31										
OPERATING FLOOR (PER BEAM)	--	1460	-310	-40	0	--	--	--	--	--
EL 119+	--	3660	8580	160	-840	--	77,000	117,000	4,000	-18,000
EL 107+	--	3870	7070	230	-380	--	123,000	201,000	6,000	-22,000
EL 85+	--	3950	8190	280	740	--	210,000	381,000	12,000	-6,000

C) MODAL DISPLACEMENTS

LOCATION	DRIFTS (Inches/G)			
	MODE 1	MODE 2	MODE 3	MODE 4
TOP OF TURBINE PEDESTAL	1.040	--	--	--
CENTER OF OPERATING FLOOR	--	0.768	-0.019	-0.015
MALL 19				
EL 140	--	0.093	-0.011	0.111
EL 123	--	0.056	-0.007	0.070
EL 104	--	0.020	-0.003	0.026
MALL 31				
EL 140	--	0.071	0.129	0.004
EL 119	--	0.044	0.090	0.003
EL 107	--	0.030	0.062	0.002



Table 2-7. Model Structural Property Values

TRIAL NO.	SYSTEM DAMPING VALUE	STIFFNESS RATIO			STRENGTH RATIO		
		SHEAR WALLS	OPERATING FLOOR	TURBINE PEDESTAL	SHEAR WALLS	OPERATING FLOOR	TURBINE PEDESTAL
1	.0601	.9343	.8421	1.4495	1.1481	.9319	1.1148
2	.0743	1.0607	.9839	.6679	1.0732	.9263	1.2484
3	.1155	.9275	1.0205	.4355	.4692	1.8888	1.0005
4	.1009	1.0914	1.7003	.7948	.8729	1.2734	1.0282
5	.1023	2.1317	1.5155	1.2248	1.4069	1.1721	1.1316
6	.0582	3.0935	.6578	1.3189	.6618	1.3248	1.4670
7	.0585	1.0504	1.1815	.5977	1.0734	.7686	1.4773
8	.0568	.9974	1.5550	1.0877	1.2396	.7181	.7032
9	.0684	1.5548	.5104	.8385	1.3007	1.2217	1.5525
10	.0648	1.1254	1.3876	2.2731	1.5946	.8750	.7939
11	.0704	1.4634	1.1817	.4356	.7953	1.0006	1.1623
12	.1493	1.4327	1.3365	1.3245	.9122	1.0389	1.5407
13	.0572	.6004	1.3288	1.0898	.7238	.8224	1.1488
14	.0927	1.5496	.4243	2.1709	.9210	1.3397	1.3248
15	.1123	.4682	1.0784	.6464	.8982	.6052	.8286
16	.0652	1.2137	1.0849	1.1087	.7419	1.4439	.8299
17	.1053	1.1349	1.7651	2.0897	.6416	1.1718	.9177
18	.0609	2.1395	.9588	.5845	1.0878	.8770	.9039
19	.1046	1.2604	1.6346	2.5241	1.1662	1.6452	1.1495
20	.1074	1.6790	.8242	2.5171	.8942	.8675	1.0032
21	.0596	.6275	.7439	.6320	.8245	.7250	.7423
22	.0760	1.0896	1.0855	.5099	.8584	1.4128	1.0756
23	.1369	3.5420	.8568	1.3599	1.2019	.9804	1.1332
24	.0831	1.0747	.4241	.6403	1.5220	.5480	1.0474
25	.1240	1.0087	.4222	1.8344	.6911	.6206	1.0911
26	.0772	.5653	.8310	.8607	1.0071	.8561	.8449
27	.1136	1.3648	.5680	.6208	1.3277	.7726	1.3637
28	.0910	.6796	1.1320	1.4513	.9571	1.0147	.7058
29	.0496	2.2246	1.8430	1.1704	1.0630	1.1235	1.3609
30	.0486	.9123	1.7765	2.3605	1.4893	.6491	1.6148
31	.0538	.4250	.5502	2.0228	1.1503	.6496	.9712
32	.1009	1.1350	.5983	2.5905	.8772	.8404	.6511
33	.0949	.8769	2.0427	.9461	.7191	1.2164	.6773
34	.0365	1.1243	1.4010	.7875	1.5064	.7779	1.0995
35	.1507	1.6197	1.7649	1.4291	.9167	1.0773	1.2275
36	.0534	.8274	.9919	.5106	.9336	1.0267	.6908
37	.0523	.6222	1.4331	.4317	.4753	.8322	1.2863
38	.0357	.6568	1.4558	1.4051	.4462	1.0556	1.5023
39	.0603	1.0507	1.2858	1.2492	1.0741	.6953	.8159
40	.0753	.9401	1.7601	1.0112	.7298	.7261	1.5294
41	.0637	1.2090	.8582	.8481	.8885	.7238	.8793
42	.0341	.5772	.8149	.9413	.5133	.8863	1.2748
43	.1107	1.1182	1.3084	.4553	.9878	1.1935	1.1383
44	.1180	2.6135	.8649	1.0102	.7662	1.1832	.4608
45	.1142	3.2185	1.5687	.8905	1.1715	.9460	.4420
46	.1162	.8227	1.1102	.7581	.8490	1.6054	.7509
47	.0783	1.0485	3.6143	.9812	1.0349	1.2617	.8452
48	.0538	1.3866	.6226	.5341	.8526	1.0044	.4262
49	.0403	.6810	1.2759	.5473	1.1852	1.0856	1.2072
50	.0616	.3445	.4155	.8854	1.1008	1.1417	1.2165



### 3. EARTHQUAKE GROUND MOTION RECORDS

The 25 earthquake ground motion time histories used in this study are tabulated in Table 3-1. The Time History number defines the order in which these time histories were used in the nonlinear analyses. The first 21 records represent actual recorded ground motions which were adjusted for the reasons shown in Table 3-1 and as described below. The last 4 records (Records 22 through 25) are simulated ground motion records generated by semi-numerical methods to simulate MS = 7.0 strike-slip earthquakes on the Hosgri fault. These records were added due to the paucity of near-source, strong motion records from rock sites for MS = 7 earthquakes with strike-slip rupture mechanisms.

The following criteria were used in selecting the 21 actual earthquake recordings for this analysis:

1. The records should be appropriate for shallow crustal earthquakes in the magnitude range from 6.5 to 7.5 with recording distances appropriate for the Hosgri fault zone.
2. The records should be appropriate for rock-site conditions.



3. The records should represent, in the aggregate, about a 50-50 mixture of thrust and strike-slip rupture mechanisms.
4. The records should be appropriate for ground motions with very high average spectral accelerations,  $\bar{S}_a$  (defined as the average 5% damped spectral acceleration in the 3 to 8.5 Hz range), of 2.0g or greater. Ground motions with  $\bar{S}_a$  less than about 2.0 g are undamaging to the Turbine Building and are thus of little interest.

Only the Tabas and Pacoima Dam Records (Records 3 through 6) met these criteria and were accepted in their unmodified original form. The Gazli Records (Records 1 and 2) had substantially too low an  $\bar{S}_a$ , but clearly met Criteria 1 and 2 and were also accepted in their unmodified original form. Unfortunately, these six records represented a thrust rupture mechanism and did not provide a broad enough characterization of ground motion at the Diablo Canyon site; therefore, the above acceptance criteria were relaxed.

Each of the other actual recordings (Records 7 through 21) required modifications to enable them to meet Criteria 1 and 2. Records 7, 8, 9, 18, 19, 20, and 21 were simply corrected for distance. This correction consisted of a frequency-independent constant upward scaling of the amplitude scale. This modification had absolutely no impact on the use



of these records since, for this study, all records were ultimately scaled by a frequency-independent constant amplitude scale factor to produce a specified  $\bar{S}_a$  value. This intermediate modification only reduced the magnitude of the final scale factor.

Records 10, 11, 12, and 13 were corrected for site conditions, Records 14 and 15 were corrected for both magnitude and distance, and Records 16 and 17 were corrected for magnitude. These corrections were frequency-dependent, non-constant amplitude corrections which modified the frequency content of the records. These modifications do influence the computed shear wall drifts for a given  $\bar{S}_a$  level. It was judged that the modified records were more appropriate for use in this study than were the unmodified records. It should be noted that only 8 of the 21 actual records required frequency-dependent modification.

After modification, all 21 empirical records met Criteria 1 and 2. Criterion 3 was met by adding the previously mentioned 4 simulated ground motion records. The  $\bar{S}_a$  values for each record after modification are given in Table 3-1. After modification Criterion 4 was only met by a few of the records; it was assumed that the records could be further modified by constant amplitude, frequency-independent upward scaling to achieve the desired values of average spectral acceleration. The fact that very few empirical time-histories were found that met Criterion 4



makes a profound statement about the lack of seismic vulnerability of the Diablo Canyon Turbine Building, which is the weakest of the Diablo Canyon essential civil structures. Seismic ground motions which have only been recorded twice anywhere in the world (Tabas and Pacoima Dam) have only a slight potential of causing measurable damage to the Turbine Building. Damage to the Turbine Building is only credible for the highly unlikely, purely hypothetical high  $\bar{S}_a$  ground motions which might be postulated for this site.

The average spectral acceleration,  $\bar{S}_a$ , does not provide a complete description of the Turbine Building damage capability of each of the records. The response spectrum shape is also an important parameter. Figures 3-1 through 3-25 present the 5% damped response spectrum for each of the 25 modified records after each record was scaled to a constant  $\bar{S}_a$  value of 3.0g. These 25 records represent a large diversity of possible spectrum shapes as illustrated in Figure 3-26. Figure 3-27 depicts the mean, median, 84% non-exceedance probability (NEP), and upper bound 5% damped spectra shapes for the case where each of the individual records were scaled to have a constant  $\bar{S}_a$  of 2.25g. One can see from Figure 3-27 that the mean and median spectra have essentially constant spectral acceleration from about 2.3 Hz to about 8.6 Hz ranging from a low of about 1.9g to a high of about 2.4g when  $\bar{S}_a = 2.25g$ . The median curve zero period acceleration is 1.04g for  $\bar{S}_a = 2.25g$ . The



ratio of 84% NEP to median spectral acceleration is approximately 1.24 between 3.5 and 10 Hz, being slightly increased at higher frequency while being substantially increased at lesser frequencies.

Each spike on the upper bound spectrum is due to a different earthquake record. For instance, the very high spike at about 14 Hz is due to Record 1 (Gazli). This high spike at 14 Hz does not contribute to Turbine Building damage because its frequency is too high. Similarly, the high spike at 3.2 Hz, due to Record 19 (Pleasant Valley Pump Station - Coalinga), does not contribute to Turbine Building damage when Record 19 is scaled up to  $\bar{S}_a \leq 4.0g$ . This spike lies within the frequency range of 3 to 8.5 Hz over which  $\bar{S}_a$  is computed and thus is accommodated in the term  $\bar{S}_a$ . Therefore, for Record 19 (Figure 3-19), scaled to  $\bar{S}_a = 3.0g$ , the spectral accelerations above 5 Hz are necessarily so low that the Turbine Building shear walls remain essentially elastic and are never driven into the frequency range of this spike. Even at  $\bar{S}_a = 4.0g$ , the shear walls do not soften sufficiently to make this spike meaningful. On the other hand, the three spikes below 2.6 Hz are each potentially damaging to the Turbine Building because these spikes lie below the 3 to 8.5 Hz frequency range for which  $\bar{S}_a$  was computed and, therefore, do not influence  $\bar{S}_a$ . As an example, the spike at 2.6 Hz is due to Record 15 (Temblor-Parkfield, Figure 3-15), which consistently led to some of the largest Turbine Building shear wall drifts at each of



the three selected  $\bar{S}_a$  values. Even at  $\bar{S}_a = 3.0g$ , this record contains sufficiently high spectral accelerations above 5 Hz to drive the Turbine Building shear wall responses down to frequencies below 3 Hz where the power of this 2.6 Hz spike becomes very important. Similarly, the 2.0 Hz spike is due to Record 18 (Pleasant Valley Pump Station - Coalinga) shown in Figure 3-18. At  $\bar{S}_a = 3.0g$ , this record contains sufficiently high spectral acceleration above 5 Hz to also drive the shear wall response frequencies down to frequencies low enough to be influenced by the 2.0 Hz spike; thus, this record was also one of the more damaging records when all records are scaled to the same  $\bar{S}_a$ . Lastly, the broad spectral acceleration peak centered at 1.3 Hz is due to Record 16 (Coyote Lake Dam - Morgan Hill) shown in Figure 3-16. This record also lead to substantial Turbine Building shear wall drifts when the ground spectrum was scaled to  $\bar{S}_a = 3.0g$  although the drifts were less than those from either Records 15 or 18.

For this study, it was assumed that each of the 25 records scaled to the same  $\bar{S}_a$  were equally probable. The results of this study concerning the probability of severe damage to the Turbine Building shear walls are sensitive to this assumption. If some of the 25 spectra shown in Figures 3-1 through 3-25 are not credible when scaled to  $\bar{S}_a = 3.0g$ , throwing these records out or assigning a higher weighting to the other more probable records could substantially influence the conclusions of



this study concerning the probability of severe Turbine Building shear wall damage.

The most interesting nonlinear analyses were those made at  $\bar{S}_a = 3.0g$  since ground motions greater than this level at the Diablo Canyon site are highly incredible considering that to date the highest  $\bar{S}_a$  ever recorded for a horizontal component is 2.5g from Tabas (Record 4). It will be shown that for  $\bar{S}_a = 3.0g$  and median structure properties, the only records which led to drifts of any segment of the shear walls in excess of 0.25% were Records 2, 5, 6, 9, 15, 16, 17, 18, 20, 23 and 24. These records all had at least one of the following two characteristics in addition to  $\bar{S}_a = 3.0g$ :

$$S_{a5\%} \geq 3.75g \text{ in the frequency range between 2.4 and 2.8 Hz}$$

or

$$S_{a5\%} \geq 3.0g \text{ in the frequency range between 1.7 and 2.0 Hz}$$

In other words, spectral acceleration in the 2.4 to 2.8 Hz range significantly exceeded  $\bar{S}_a$  or else spectral accelerations had not dropped below  $\bar{S}_a$  in the 1.7 to 2 Hz range. Two other records also had these characteristics (Records 22 and 25) but both only produced 0.19% maximum



shear wall drifts. The 12 other records did not have at least one of the characteristics shown above and none produced drifts as high as 0.25% for  $\bar{S}_a = 3.0g$ . Since a drift of 0.25% is estimated to lie at least 3 standard deviations below an estimated median drift of 0.7% corresponding to severe shear wall damage, those 12 records, when scaled to  $\bar{S}_a = 3.0g$ , are not potentially damaging to the Turbine Building with median properties. Even when uncertainty concerning structural properties was included in the nonlinear analyses, drifts for  $\bar{S}_a = 3.0g$  did not exceed 0.42% (1.5 standard deviations below 0.7%) for these 12 records with one exception. This exception was Trial 13 which used Record 13 (El Centro No. 4 -Imperial Valley) and both very low stiffnesses and strengths for the shear walls (Table 2-7). It was judged that this exception was more due to the low structural properties than due to the characteristics of the ground motion record. Thus, 13 records (52% of the data set) exhibited the potentially damaging characteristics defined above when scaled to  $\bar{S}_a = 3.0g$  and 48% did not. It is particularly interesting to note that Tabas (Records 3 and 4), which was the only record with an actual unmodified  $\bar{S}_a > 2.0g$  was not potentially damaging to the Turbine Building shear walls even when scaled up to  $\bar{S}_a = 3.0g$ . The Tabas records were particularly benign.

With median structural properties, it will be concluded that there is about a 3% probability of severe damage to the Turbine Building shear



walls at  $\bar{S}_a = 3.0g$ . This conclusion is totally due to the inclusion of Records 15 (Temblor-Parkfield), 18 (Pleasant Valley Pump Station-Coalinga), and 20 (Dayhook) in the data set. If these three records had been removed, the probability of severe damage at  $\bar{S}_a = 3.0g$  would have been reduced to essentially zero. All three of these records had 5% damped spectral acceleration in excess of 5.0g in the 2.0 to 2.6 Hz frequency range when scaled to  $\bar{S}_a = 3.0g$ . The open question is whether there really is about a 12% probability of  $S_{a5\%} > 5.0g$  in the 2.0 to 2.6 Hz frequency range when  $\bar{S}_a = 3.0g$ . If not, then the probability of severe damage to the shear walls is overstated for median structural properties by the inclusion of these three records.

With randomly selected structural properties, and  $\bar{S}_a = 3.0g$ , the highest and third highest drifts were produced by the two trials which used Record 15 (Temblor-Parkfield). Also, the second and fourth highest drifts in the shear walls were produced by the two trials which used Record 17 (Coyote Lake Dam-Morgan Hill). At  $\bar{S}_a = 3.0g$ , these four trials produced drifts ranging from 0.83% to 1.10%. None of the other 46 trials produced drifts in excess of 0.71%. It will be concluded that there is about 11% composite probability of severe damage to the Turbine Building shear walls at  $\bar{S}_a = 3.0g$  when uncertainty in structural properties are included. If the 4 trials which used Records 15 and 17 had been deleted, the composite probability would have been reduced to



only about 5%. If the 8 trials which used Records 15, 17, 18 and 20 had been removed, the composite probability would have been reduced to about 4%. If only the 8 trials which used Tabas (Records 3 and 4) and Pacoima Dam (Records 5 and 6) had been included, the composite probability of severe shear wall damage at  $\bar{S}_a = 3.0g$  would have been reduced to about 1.3%. Thus, there is more than a factor of 8 difference in the estimate of the composite probability of severe shear wall damage at  $\bar{S}_a = 3.0g$  depending upon which ground motion records are included.

Only Tabas and Pacoima Dam had  $\bar{S}_a$  greater than 1.8g for the original unscaled and unmodified records. It would have been nice to have only included records which had this characteristic. However, it is obvious that the four Tabas and Pacoima Dam Records could not possibly represent the full diversity of possible ground motion characteristics for constant values of  $\bar{S}_a$  in excess of 2.0g. From the above discussion, it is equally clear that the decision concerning which records to include has a dramatic influence on the computed probability of severe shear wall damage. Inclusion of Records 15, 17, 18 and 20 increase the reported composite probability of severe shear wall damage at  $\bar{S}_a = 3.0g$  by about a factor of 2.7. None of these records was directly applicable for the Diablo Canyon conditions. Records 18 and 20 were recorded at too great a distance. Record 17 was associated with too low a magnitude; and Record 15 was associated with both too low a magnitude



and too great a distance. Both Records 15 and 17 required frequency-dependent scaling which enhanced their low frequency content. It should again be noted that the four highest drifts from the 50 trials at  $\bar{S}_a = 3.0g$  with uncertain structural properties came from the four trials which used Records 15 and 17. This result was significantly influenced by the enhancement of low frequency content in these two records. Even so, all 25 records were included and weighted as being equally likely in order to overestimate the diversity of possible ground motion at the Diablo Canyon site. For the reasons discussed in the preceding paragraphs, this decision to equally weight all 25 records could result in a substantial conservative bias to the probabilities of severe shear wall distress reported herein. At  $\bar{S}_a = 3.0g$ , the reported probabilities of severe shear wall distress could be conservative by more than a factor of 8.



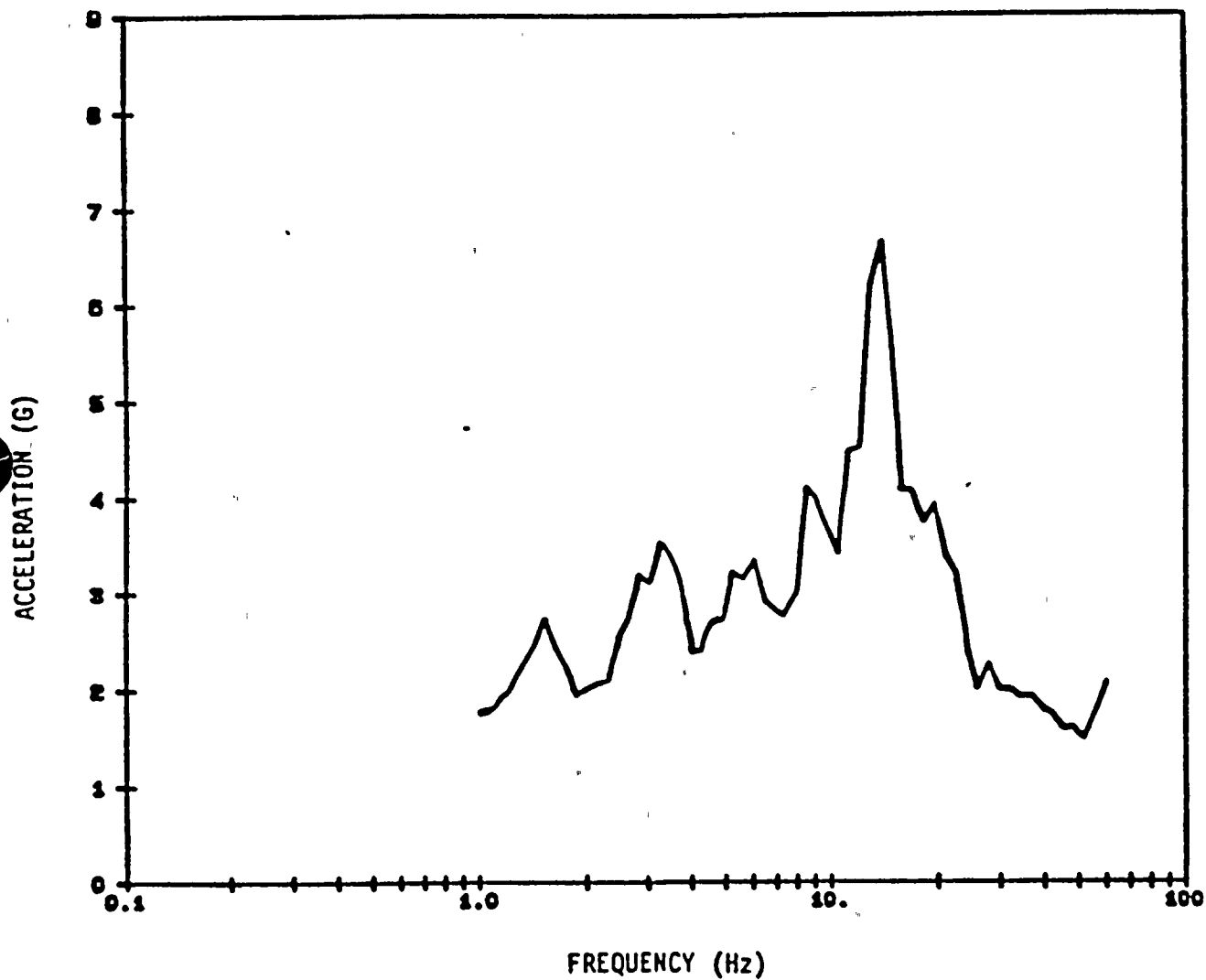


Figure 3-1. Gazli, U.S.S.R., 17 May 1976, Karakyr Point, Component North, 5% Damped Spectral Acceleration - Record 1 Scaled to  $\bar{S}_a = 3.0g$



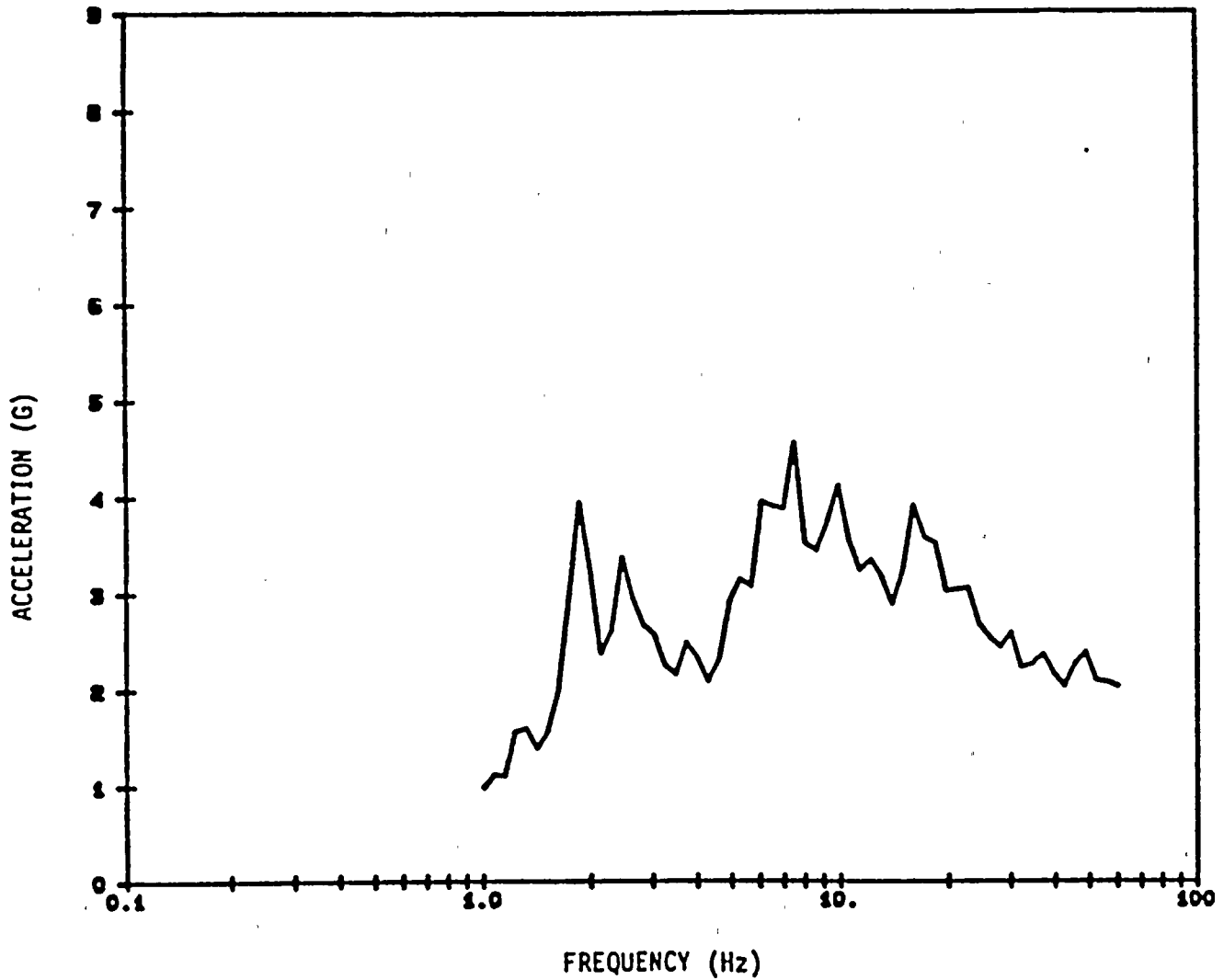


Figure 3-2. Gazli, U.S.S.R., 17 May 1976, Karakyr Point, Component East,  
5% Damped Spectral Acceleration - Record 2 Scaled to  $\bar{S}_a = 3.0g$



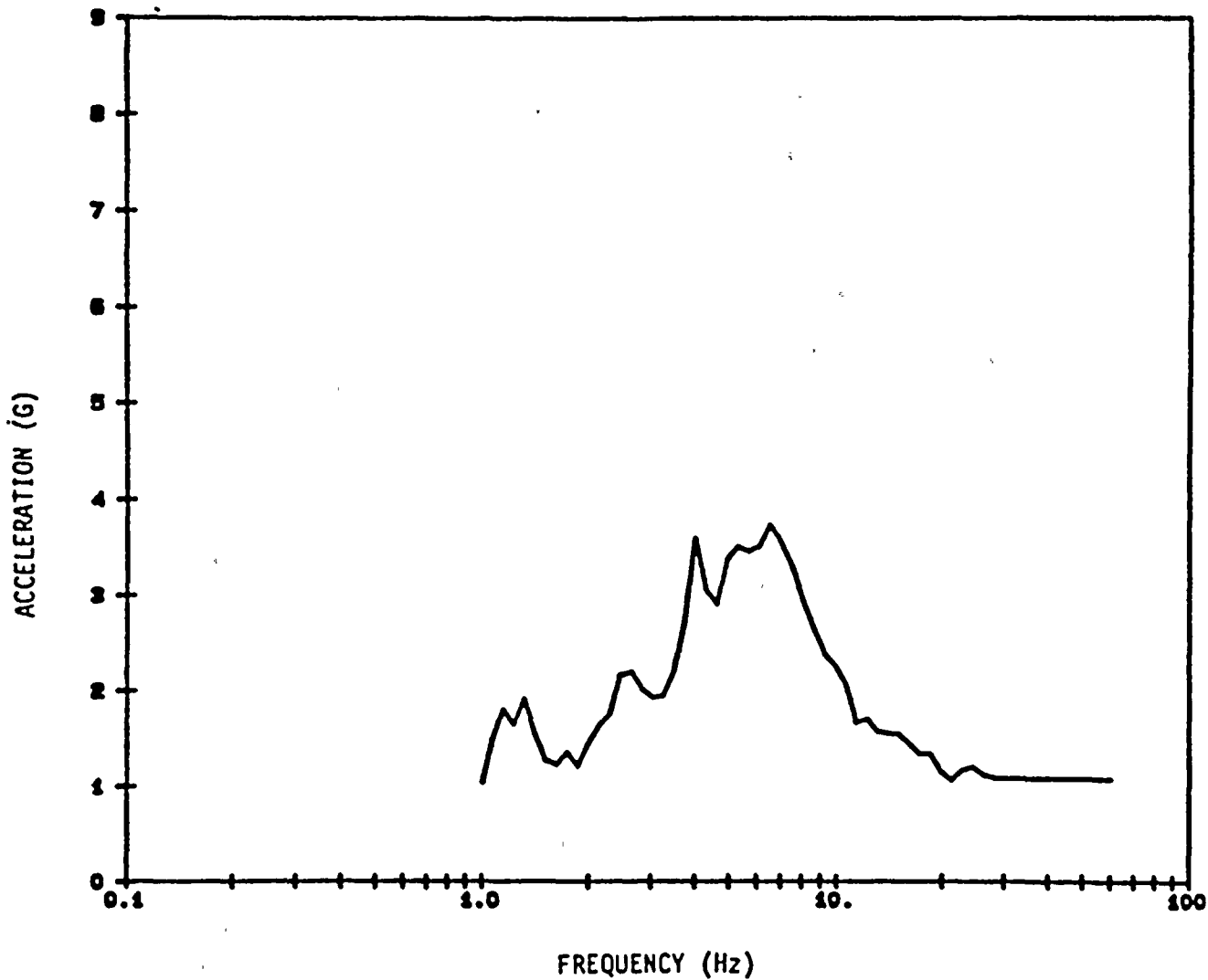


Figure 3-3. Tabas, Iran, 16 September 1978, Component N74E, 5% Damped Spectral Acceleration - Record 3 Scaled to  $\bar{S}_a = 3.0g$



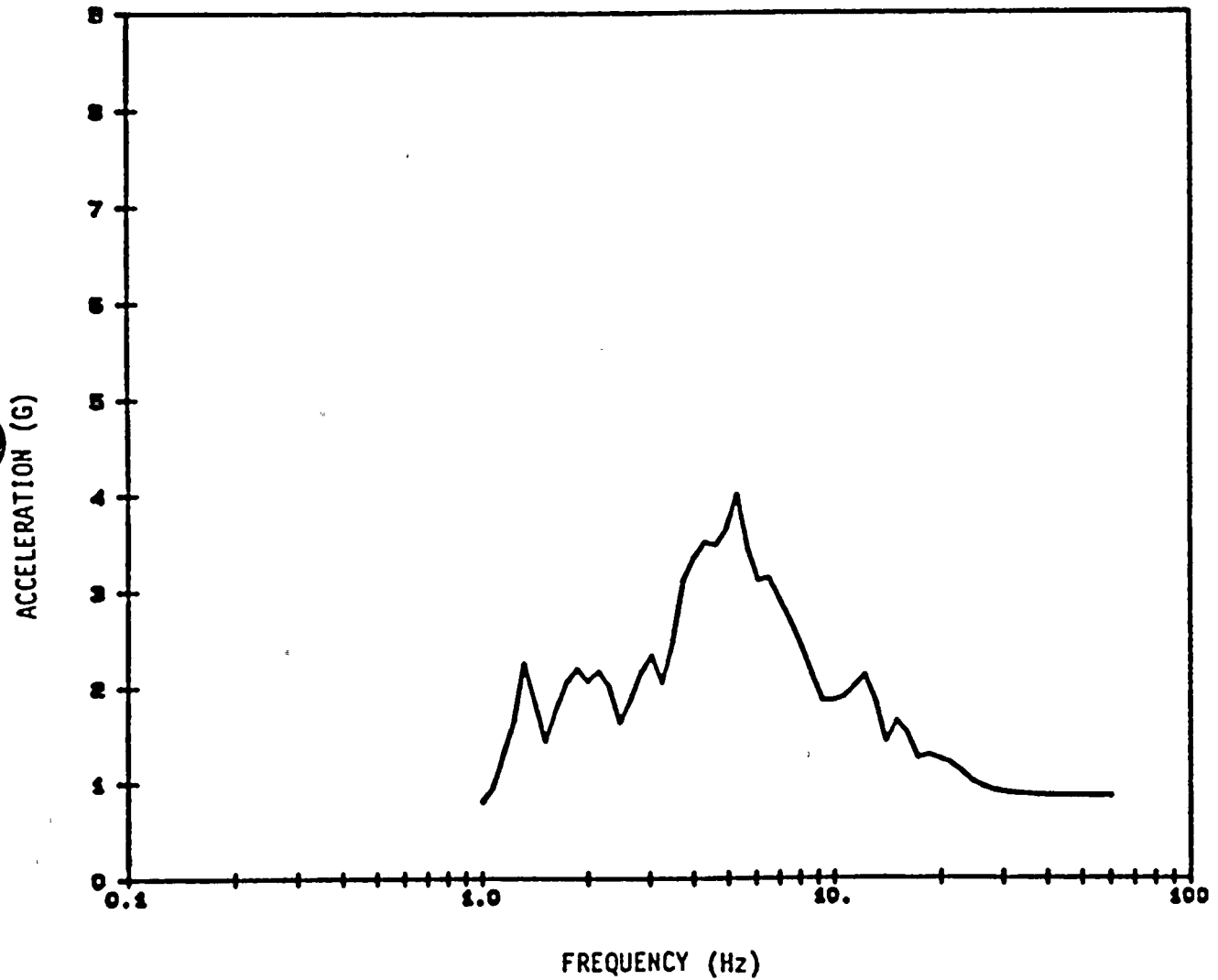


Figure 3-4. Tabas, Iran, 16 September 1978, Component N16W, 5% Damped Spectral Acceleration - Record 4 Scaled to  $\bar{S}_a = 3.0g$



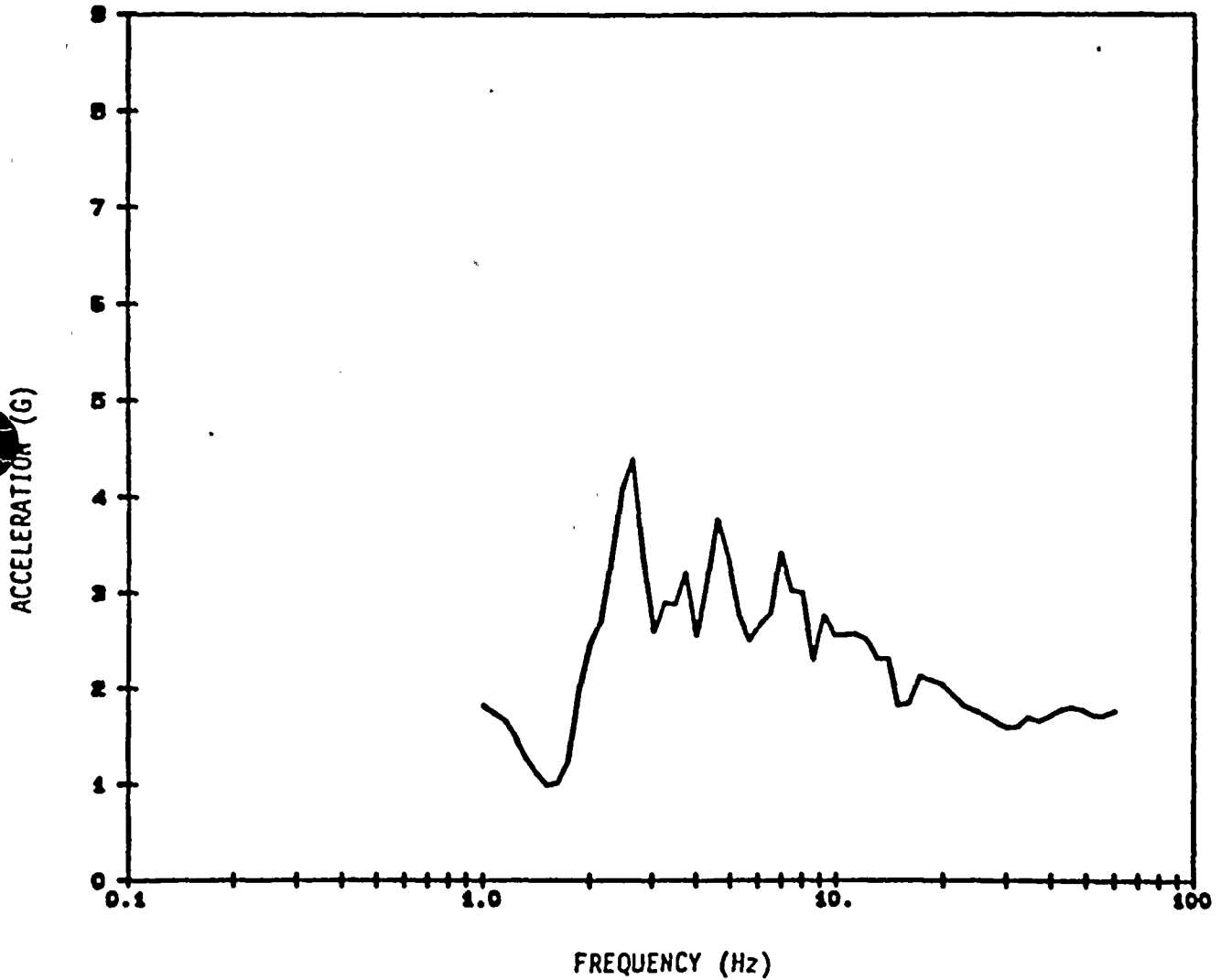


Figure 3-5. San Fernando, CA, 09 February 1971, Pacoima Dam, Component S16E, 5% Damped Spectral Acceleration - Record 5 Scaled to  $\bar{S}_a = 3.0g$



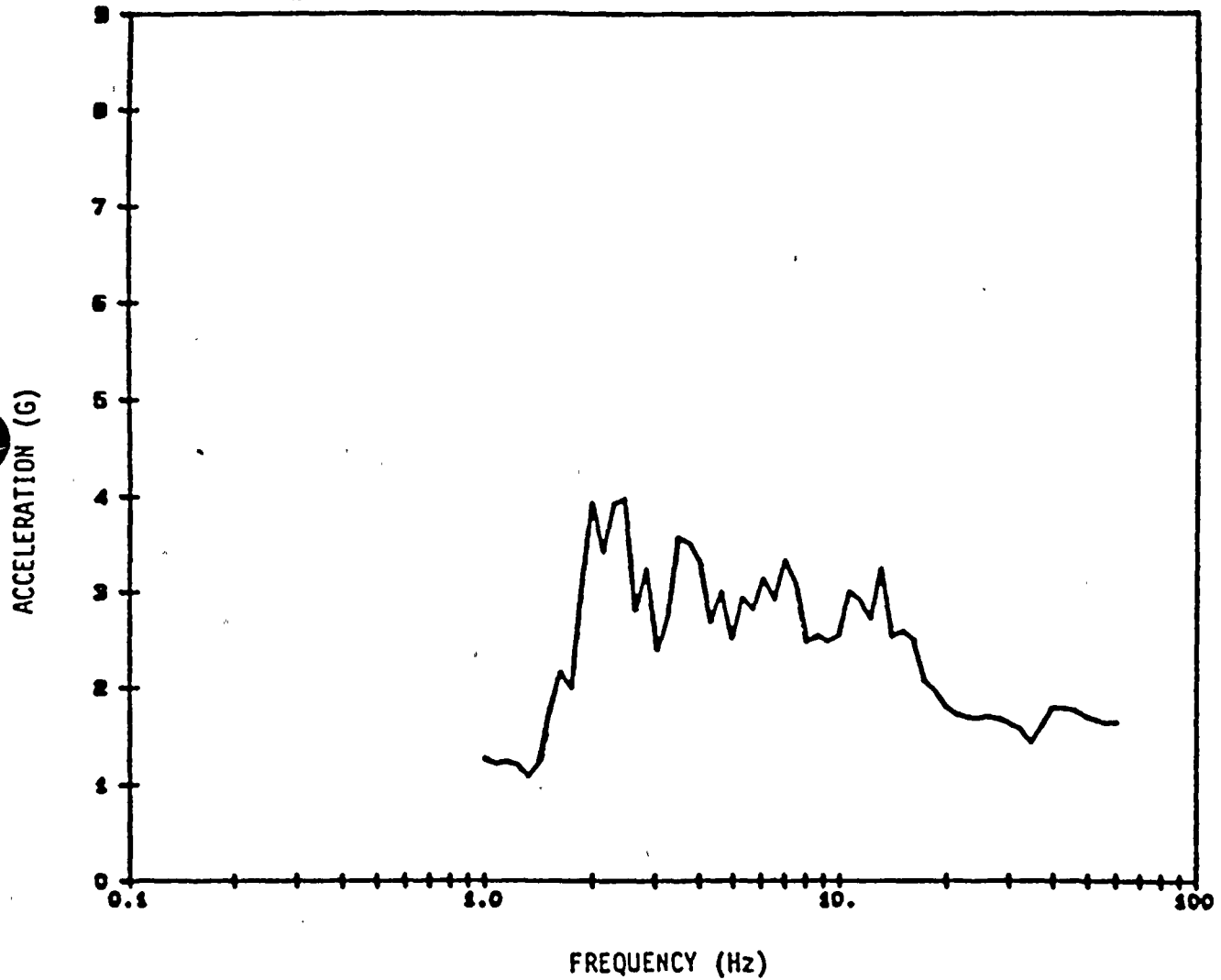


Figure 3-6. San Fernando, CA, 09 February 1971, Pacoima Dam, Component S74W, 5% Damped Spectral Acceleration - Record 6 Scaled to  $\bar{S}_a = 3.0g$



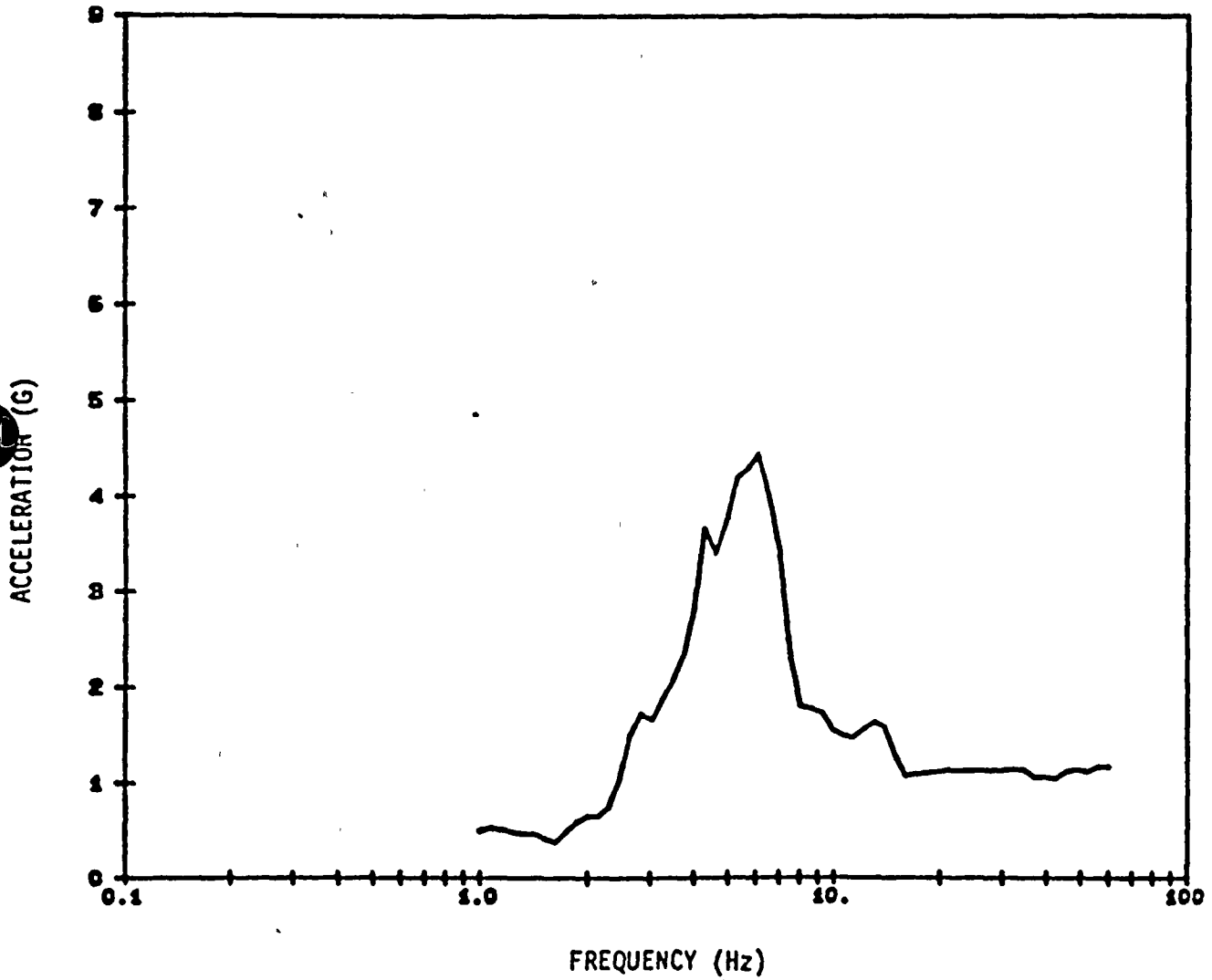


Figure 3-7. San Fernando, CA, 09 February 1971, Lake Hughes #12, Component N21E, 5% Damped Spectral Acceleration - Record 7 Scaled to  $\bar{S}_a = 3.0g$



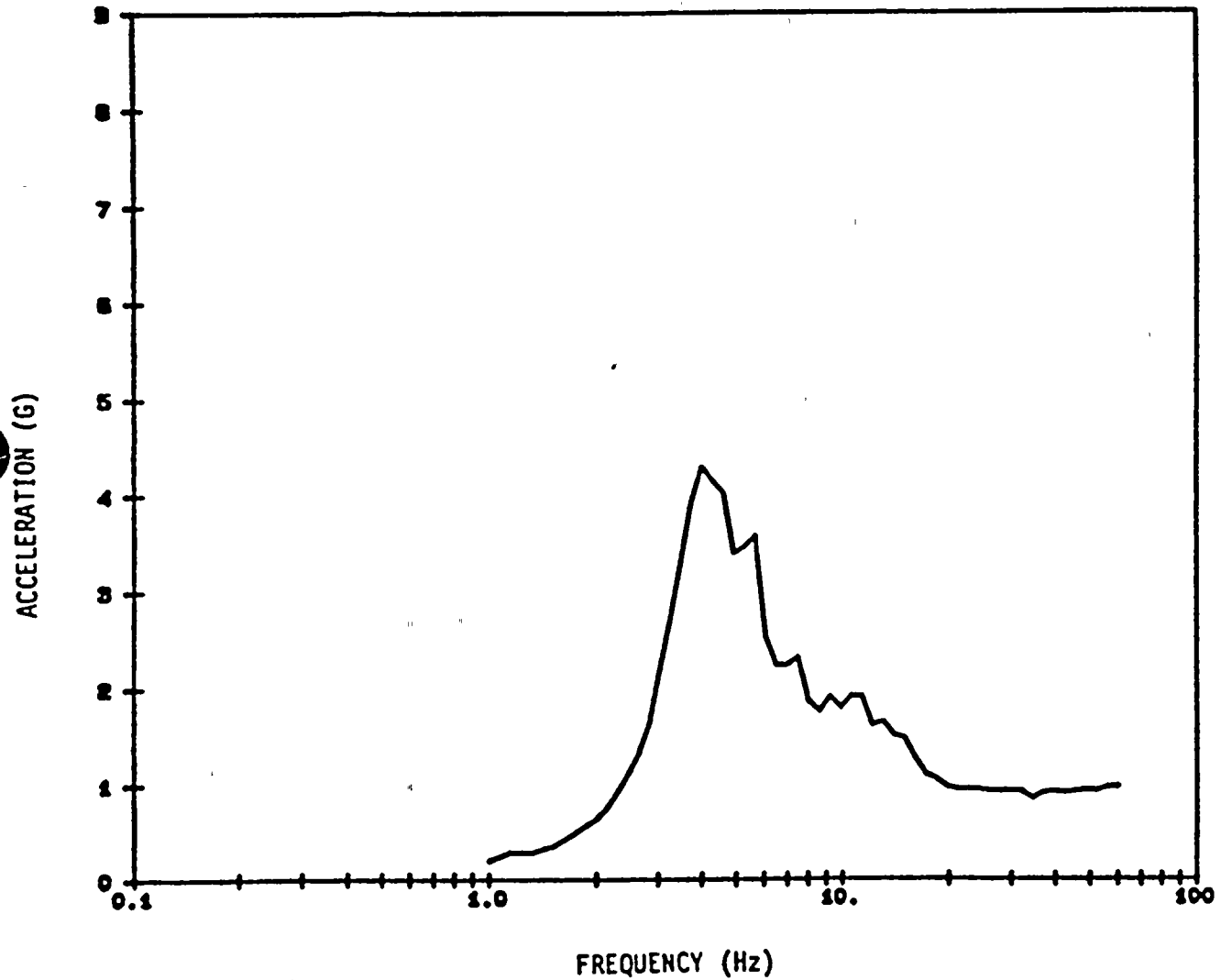


Figure 3-8. San Fernando, CA, 09 February 1971, Lake Hughes #12, Component N69W, 5% Damped Spectral Acceleration - Record 8 Scaled to  $\bar{S}_a = 3.0g$



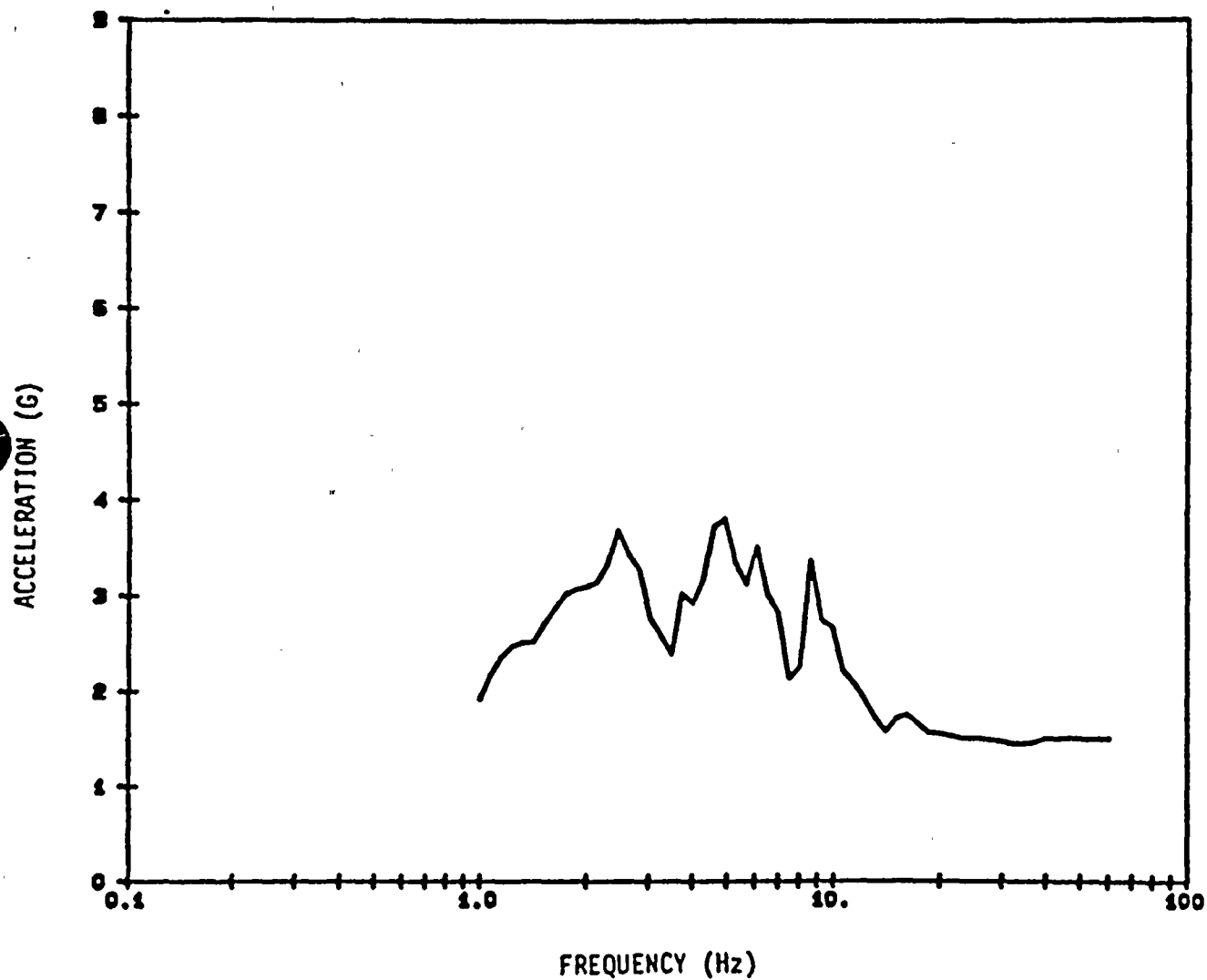


Figure 3-9. San Fernando, CA, 09 February 1971, Castaic, Component N69W, 5% Damped Spectral Acceleration - Record 9 Scaled to  $\bar{S}_a = 3.0g$



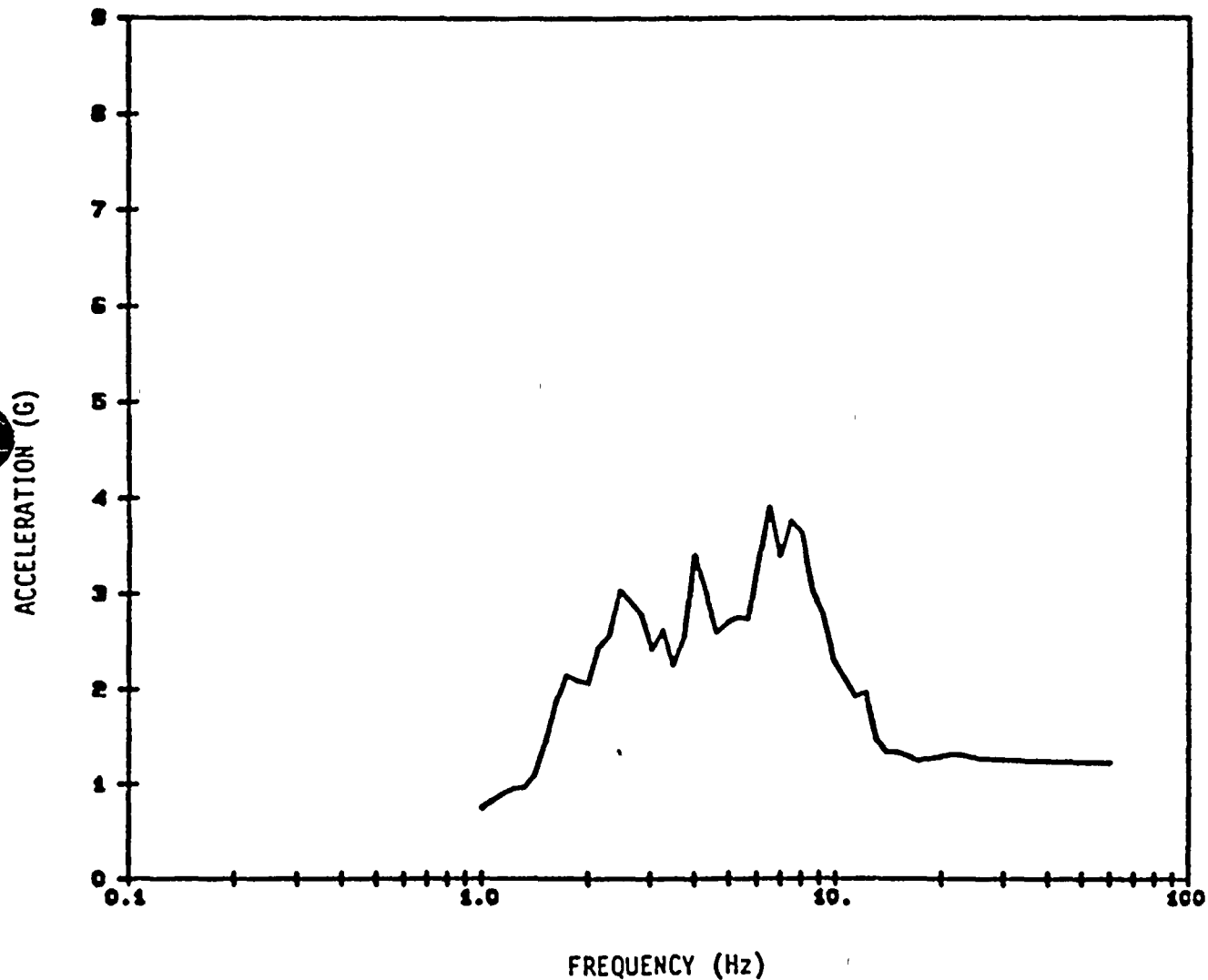


Figure 3-10. Imperial Valley, CA, 15 October 1979, El Centro, Component NOOE, 5% Damped Spectral Acceleration - Record 10 Scaled to  $\bar{S}_a = 3.0g$



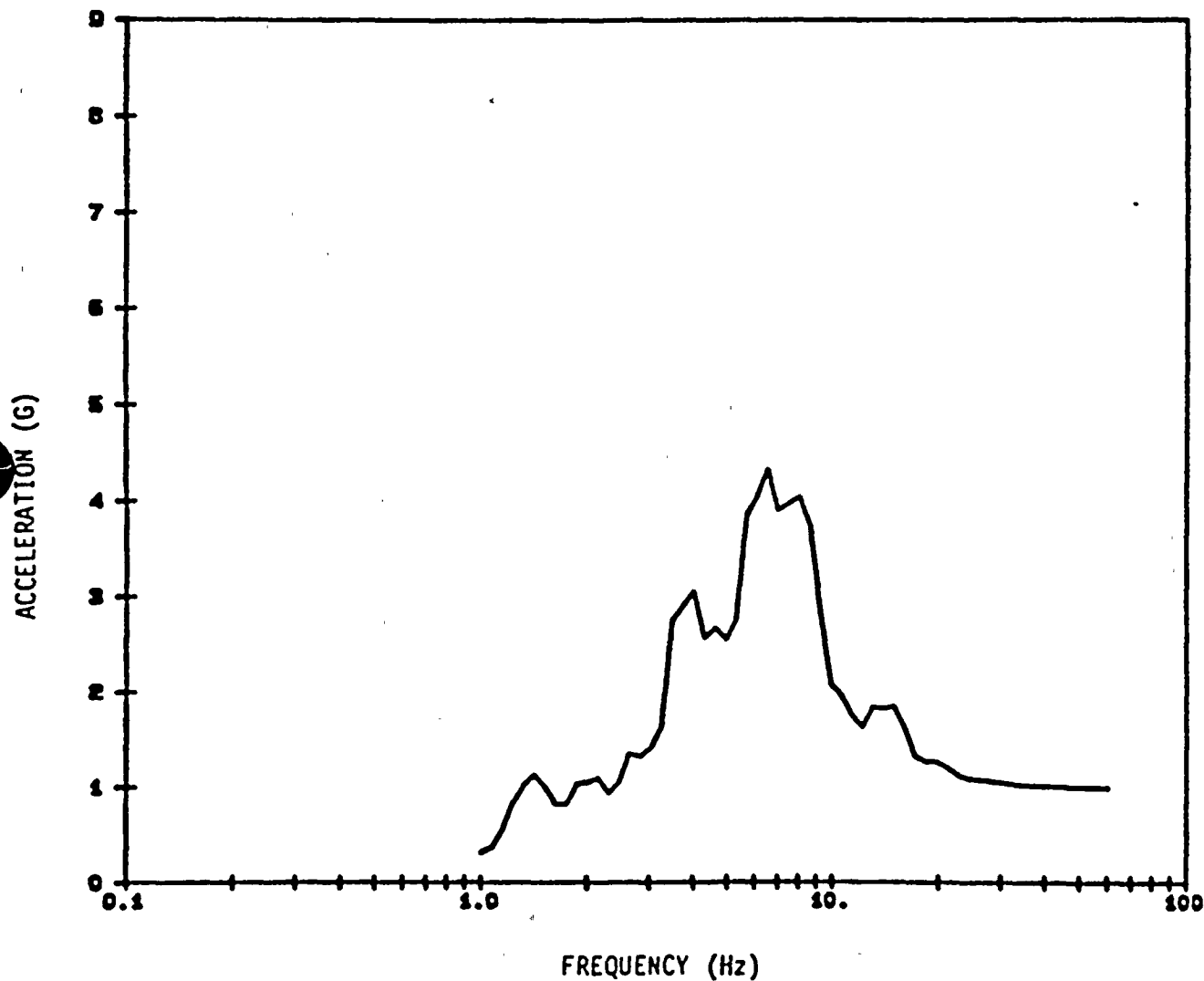


Figure 3-11. Imperial Valley, CA, 15 October 1979, El Centro, Component N90W, 5% Damped Spectral Acceleration - Record 11 Scaled to  $S_a = 3.0g$



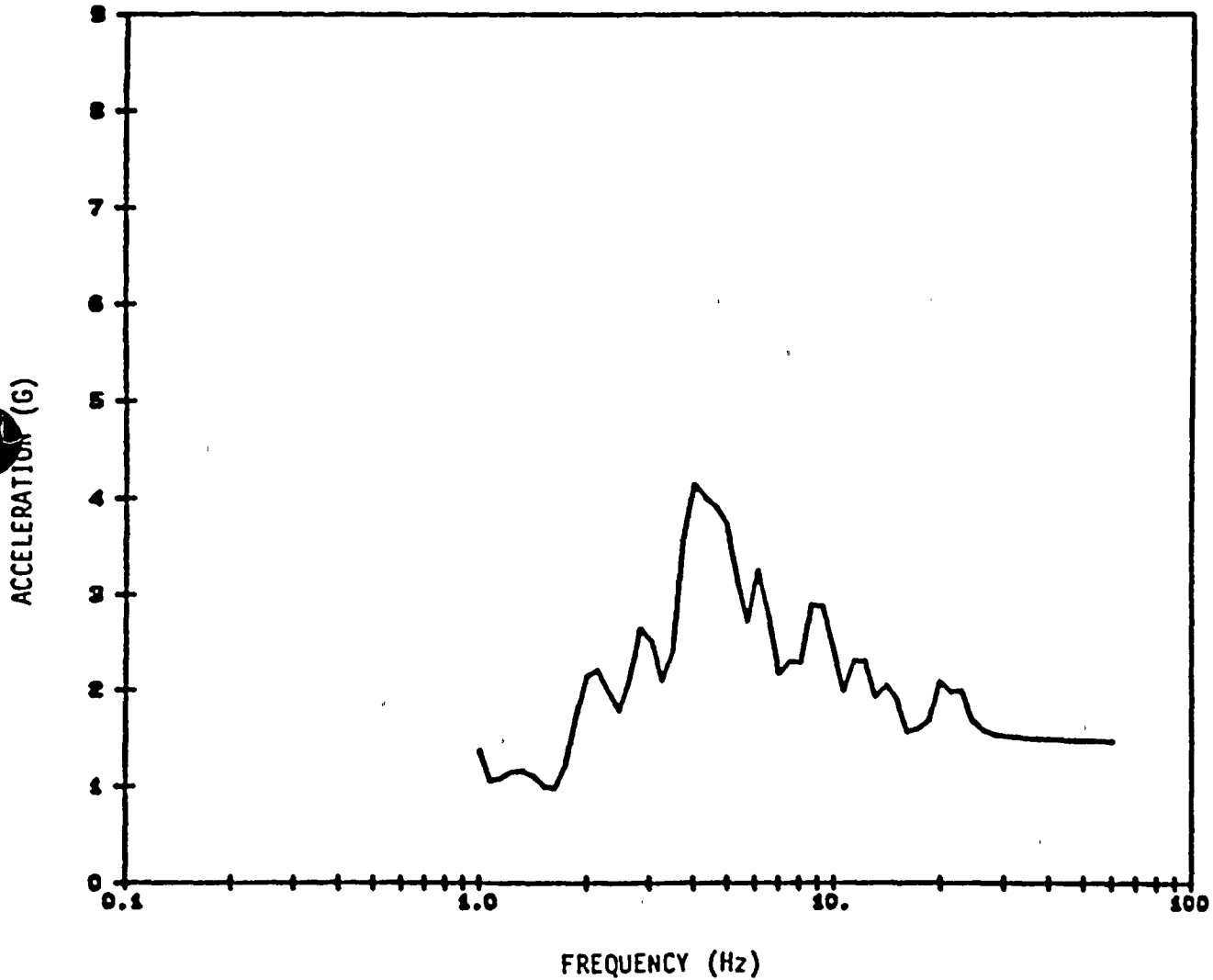


Figure 3-12. Imperial Valley, CA, 15 October 1979, El Centro #4, Component S50W, 5% Damped Spectral Acceleration - Record 12 Scaled to  $S_a = 3.0g$



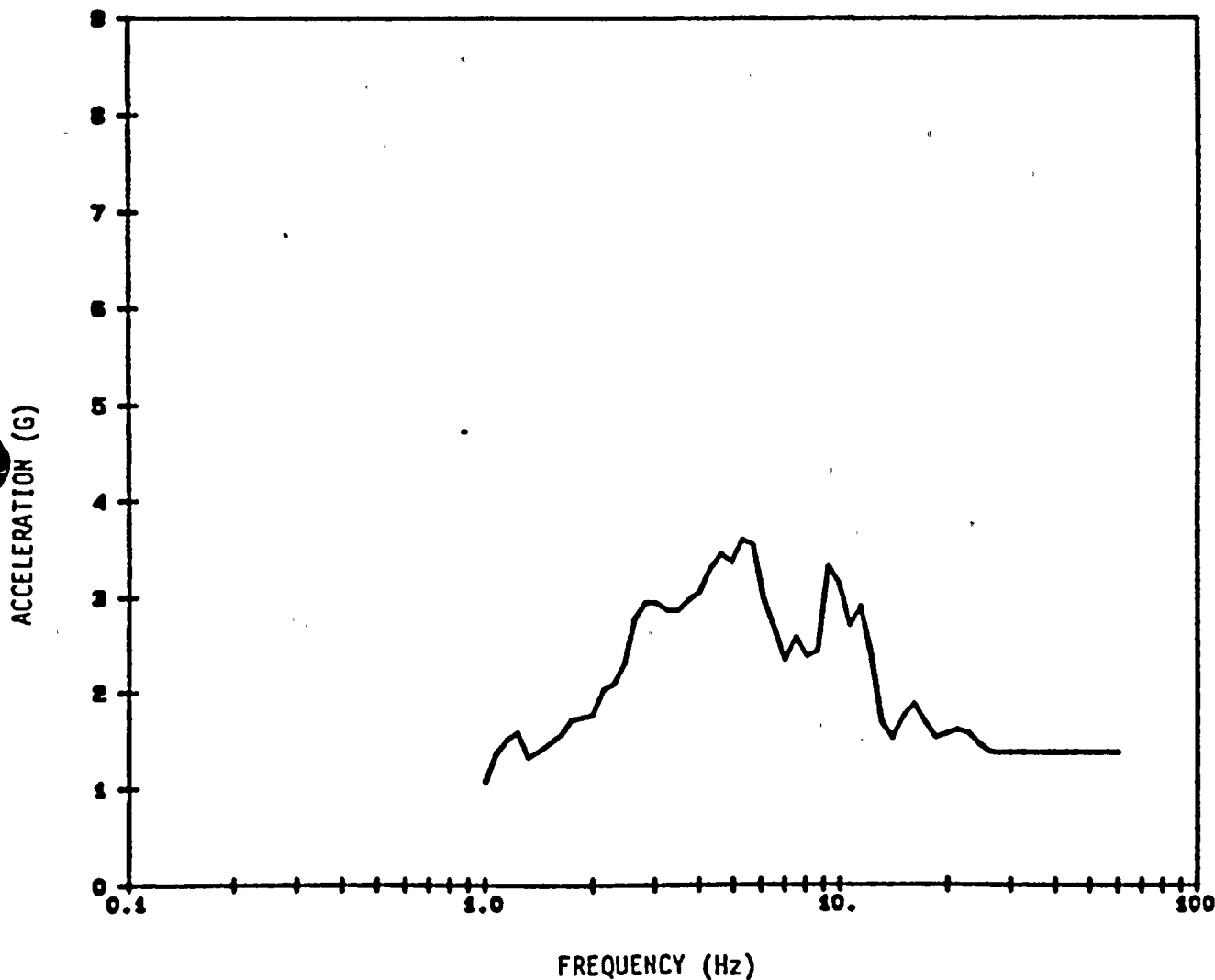


Figure 3-13. Imperial Valley, CA, 15 October 1979, El Centro #4, Component S40E, 5% Damped Spectral Acceleration - Record 13 Scaled to  $S_a = 3.0g$



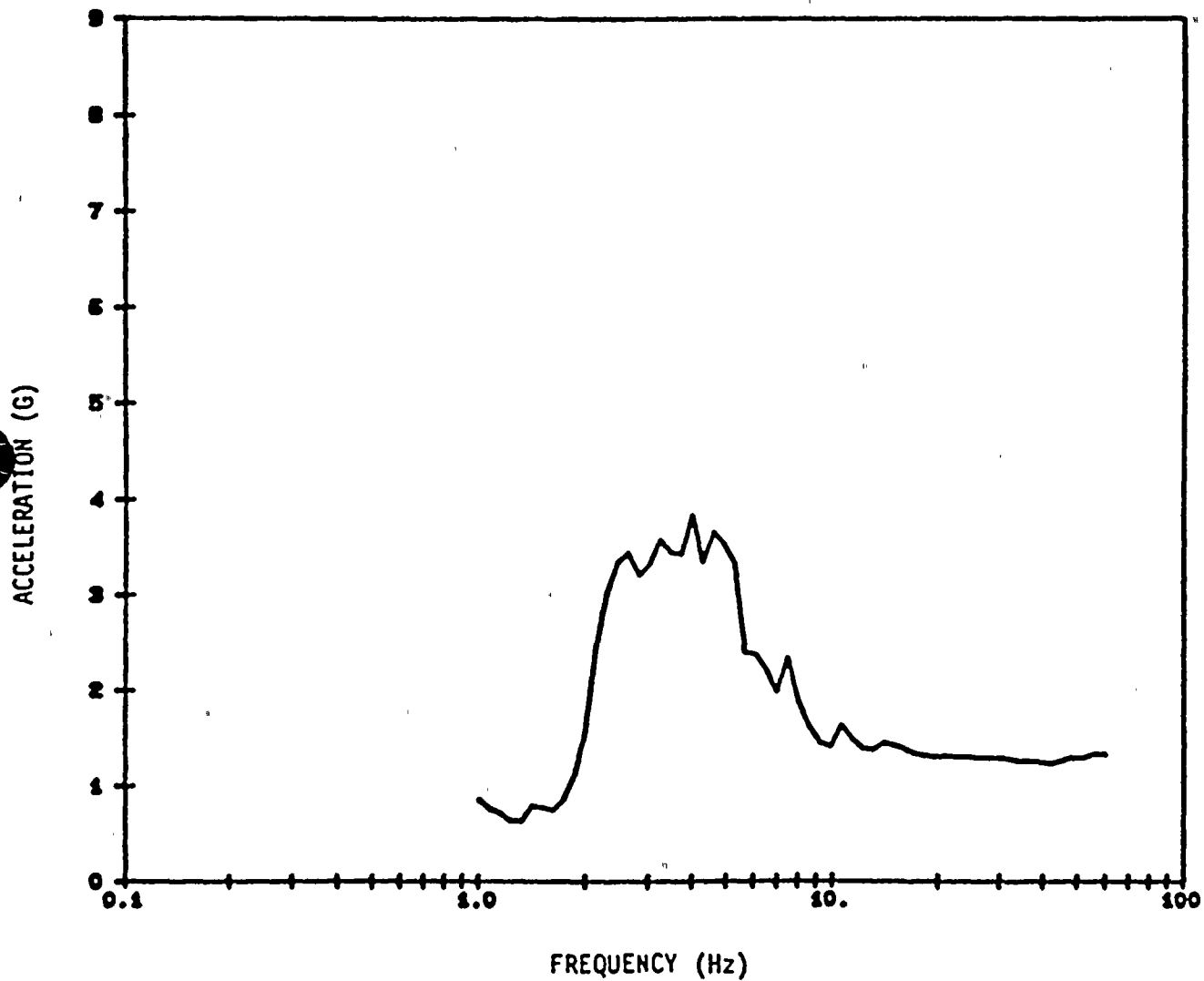


Figure 3-14. Parkfield, CA, 27 June 1966, Temblor, Component N65W,  
5% Damped Spectral Acceleration - Record 14 Scaled to  $\xi_a = 3.0g$



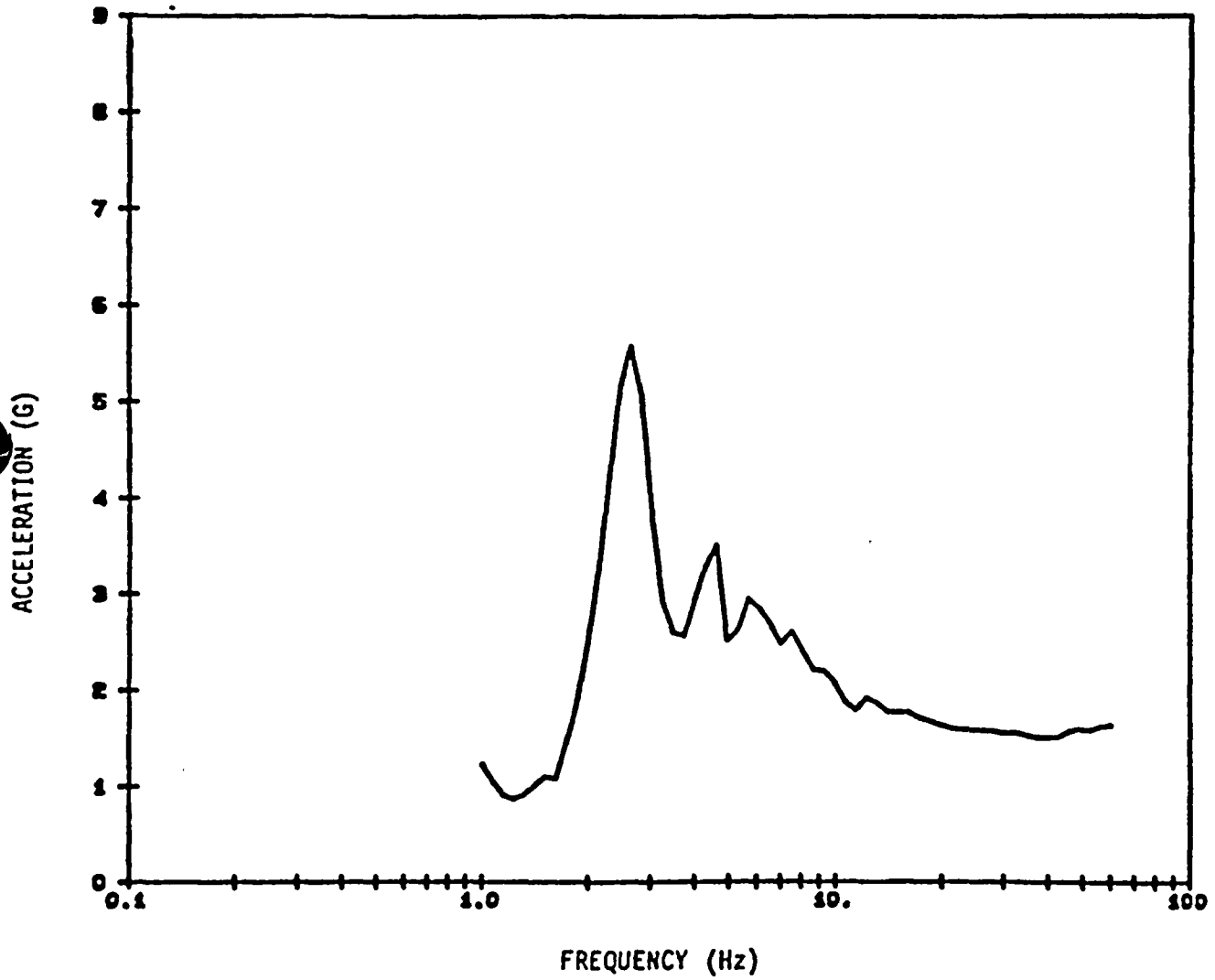


Figure 3-15. Parkfield, CA, 27 June 1966, Temblor, Component S25W,  
5% Damped Spectral Acceleration - Record 15 Scaled to  $\bar{S}_a = 3.0g$



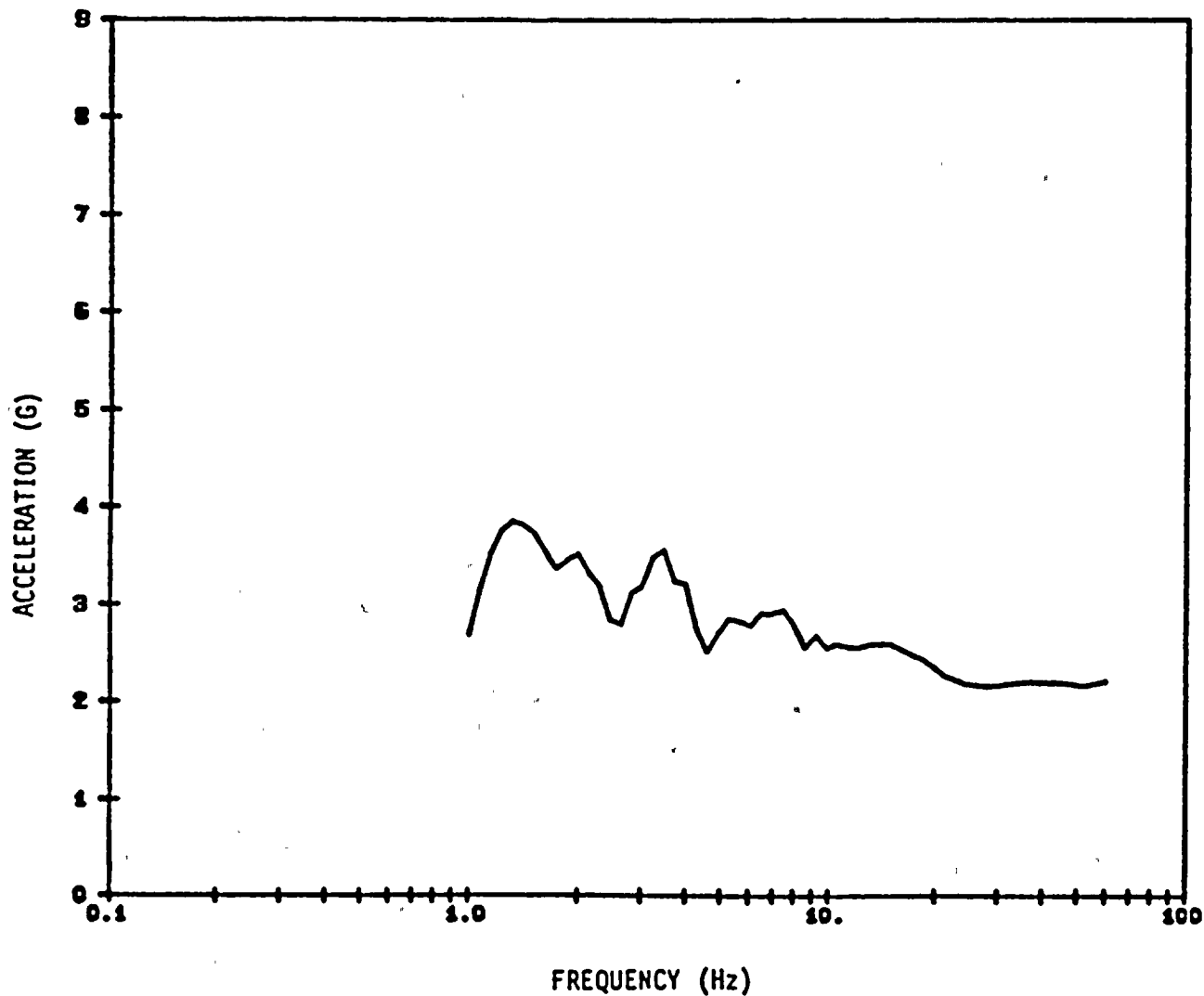


Figure 3-16. Morgan Hill, CA, 24 April 1984, Coyote Lake Dam, Component N75W, 5% Damped Spectral Acceleration - Record 16 Scaled to  $\bar{S}_a = 3.0g$



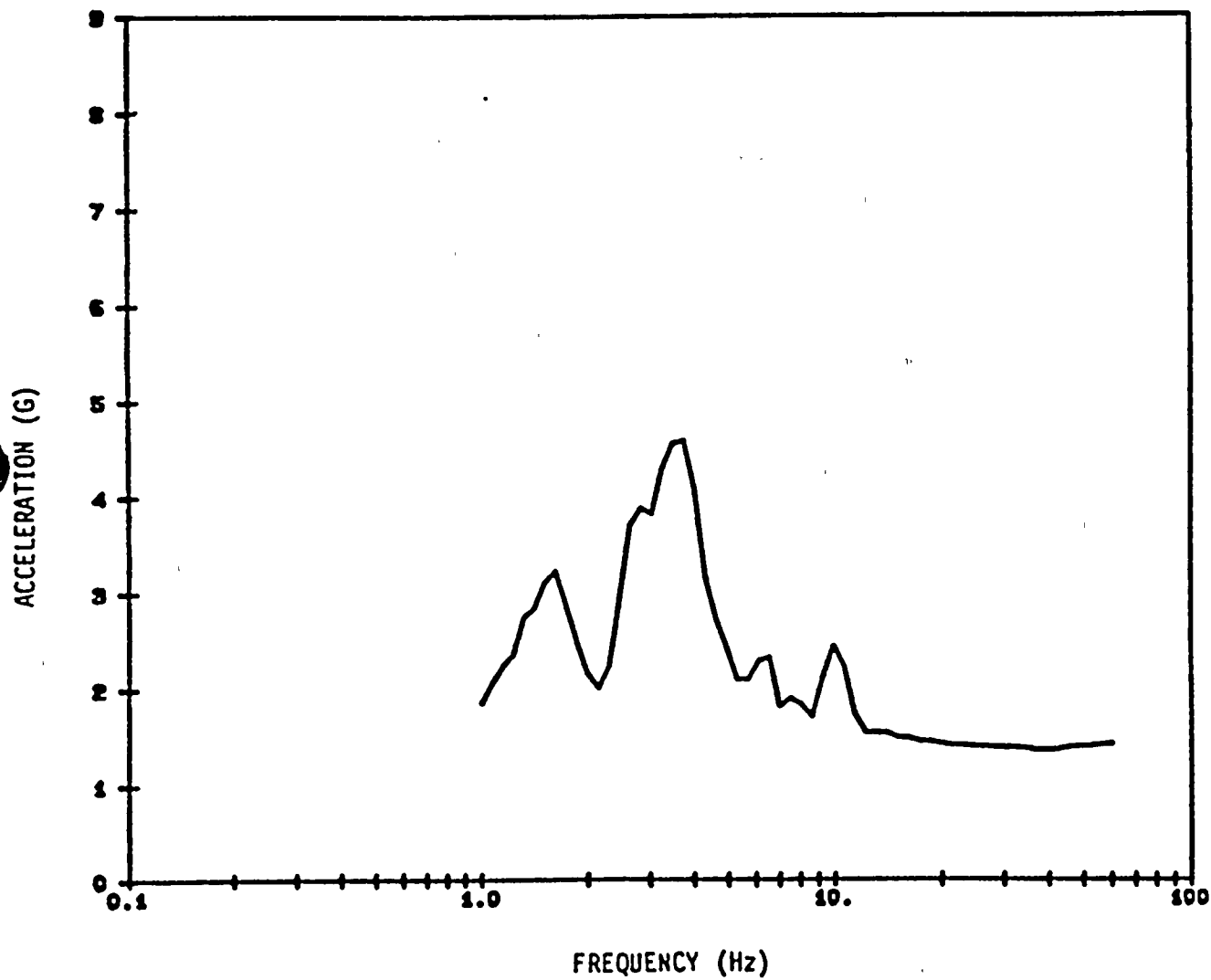


Figure 3-17. Morgan Hill, CA, 24 April 1984, Coyote Lake Dam, Component S15W, 5% Damped Spectral Acceleration - Record 17 Scaled to  $S_a = 3.0g$



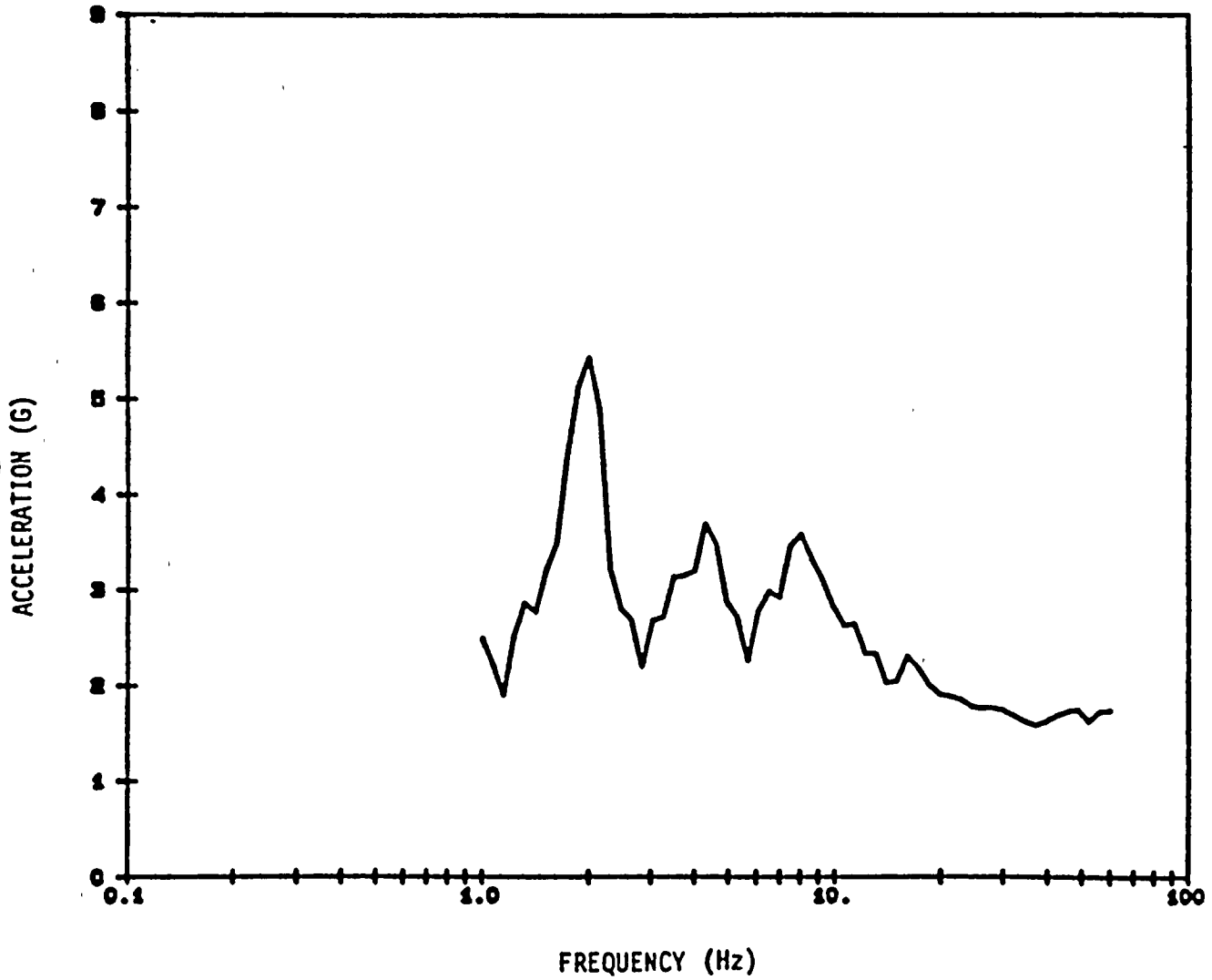


Figure 3-18. Coalinga, CA, 02 May 1983, Pleasant Valley Pump Station, (Switchyard), Component 045, 5% Damped Spectral Acceleration - Record 18 Scaled to  $S_a = 3.0g$



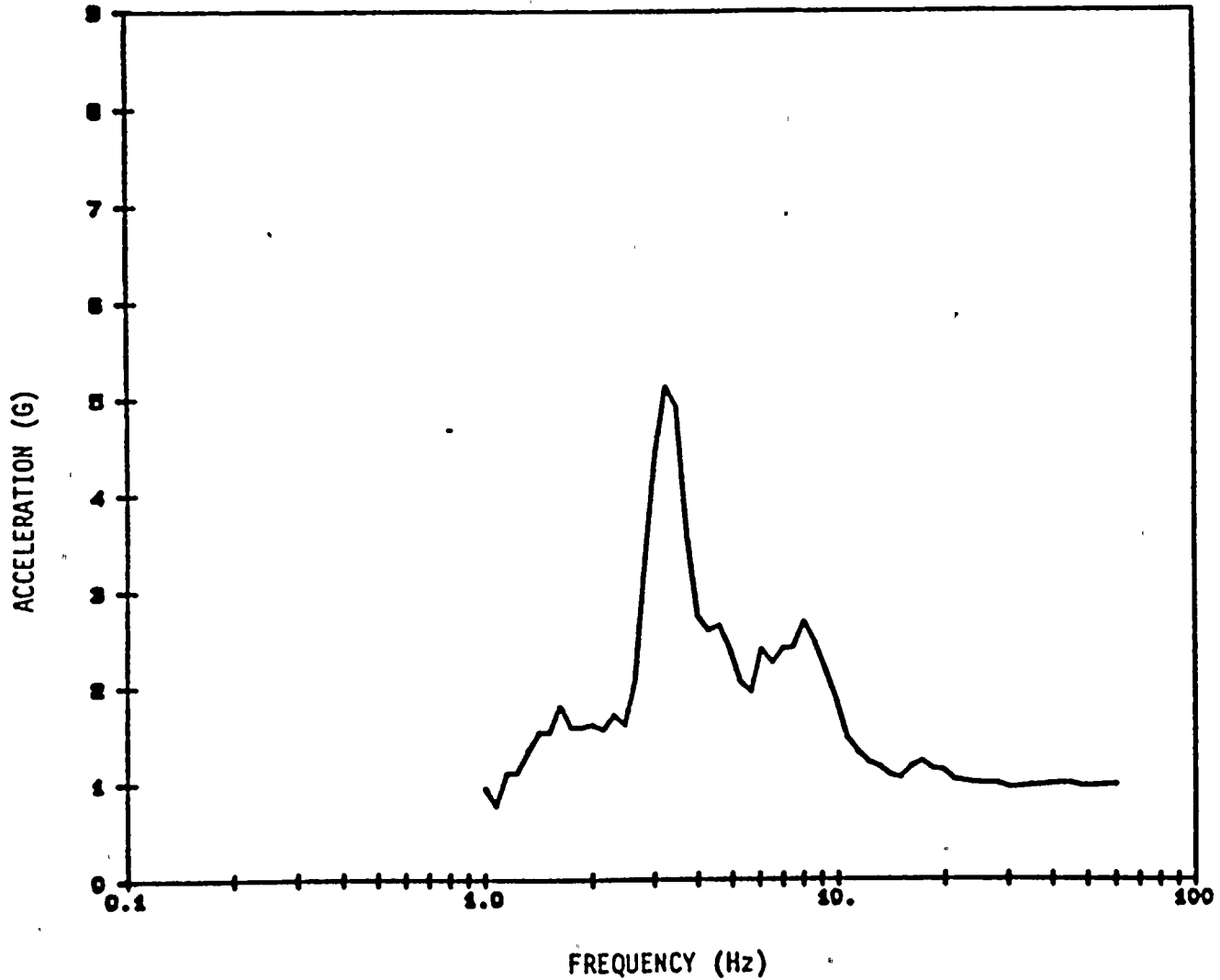
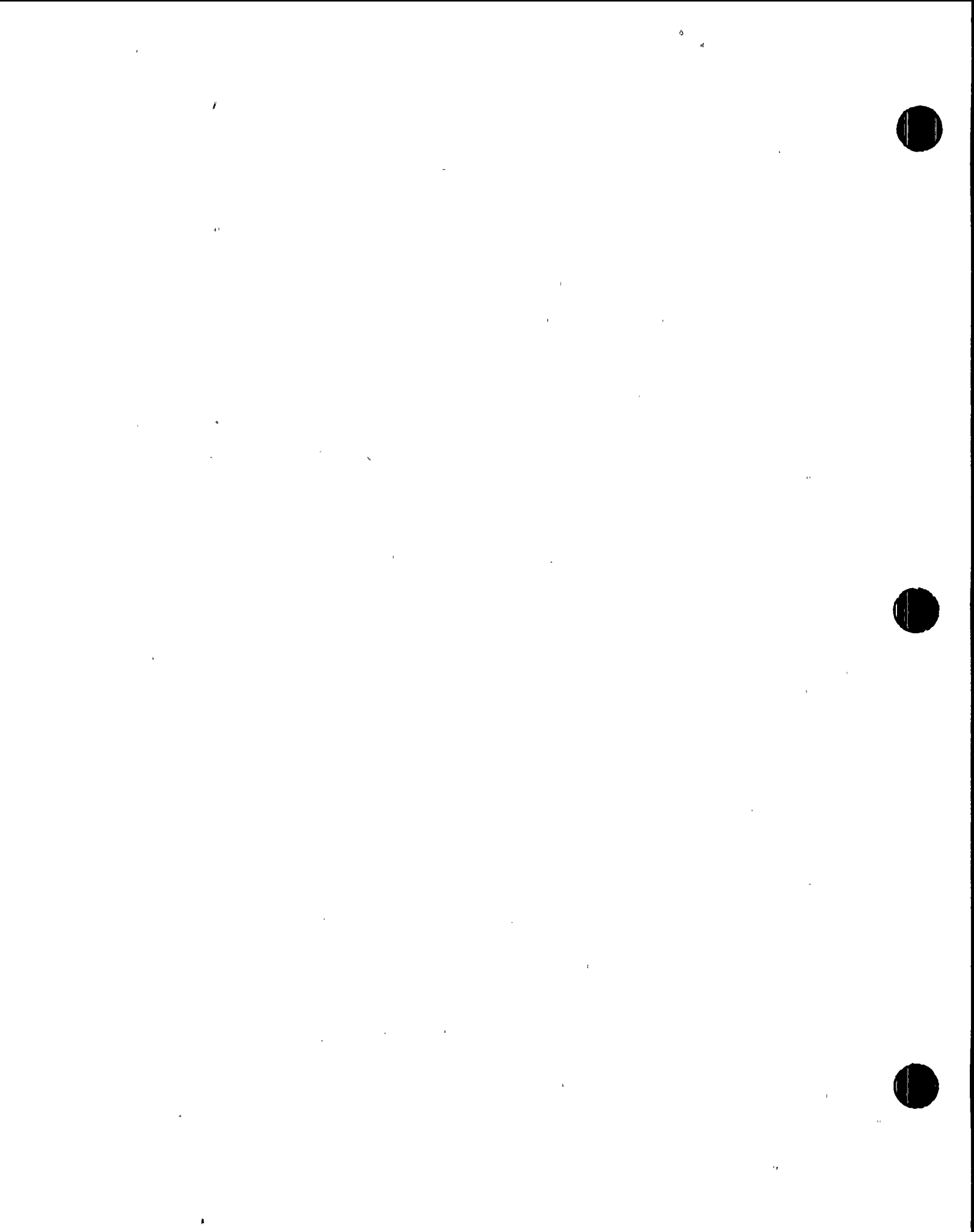


Figure 3-19. Coalinga, CA, 02 May 1983, Pleasant Valley Pump Station, (Switchyard), Component 135, 5% Damped Spectral Acceleration - Record 19 Scaled to  $S_a = 3.0g$



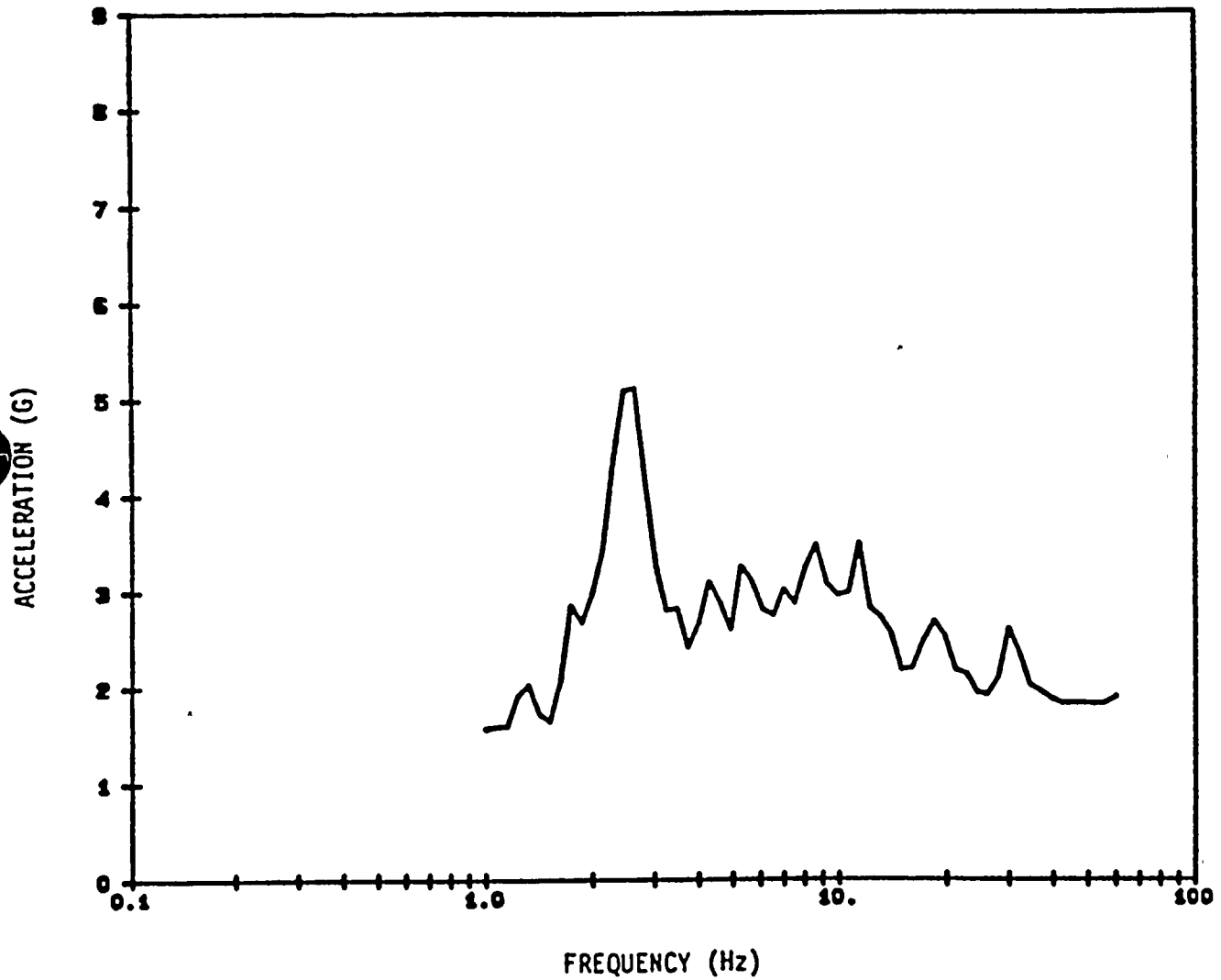


Figure 3-20. Dayhook. Scaled (X1.7). Component N10E, Baseline Corrected, 5% Damped Spectral Acceleration - Record 20 Scaled to  $S_a = 3.0g$



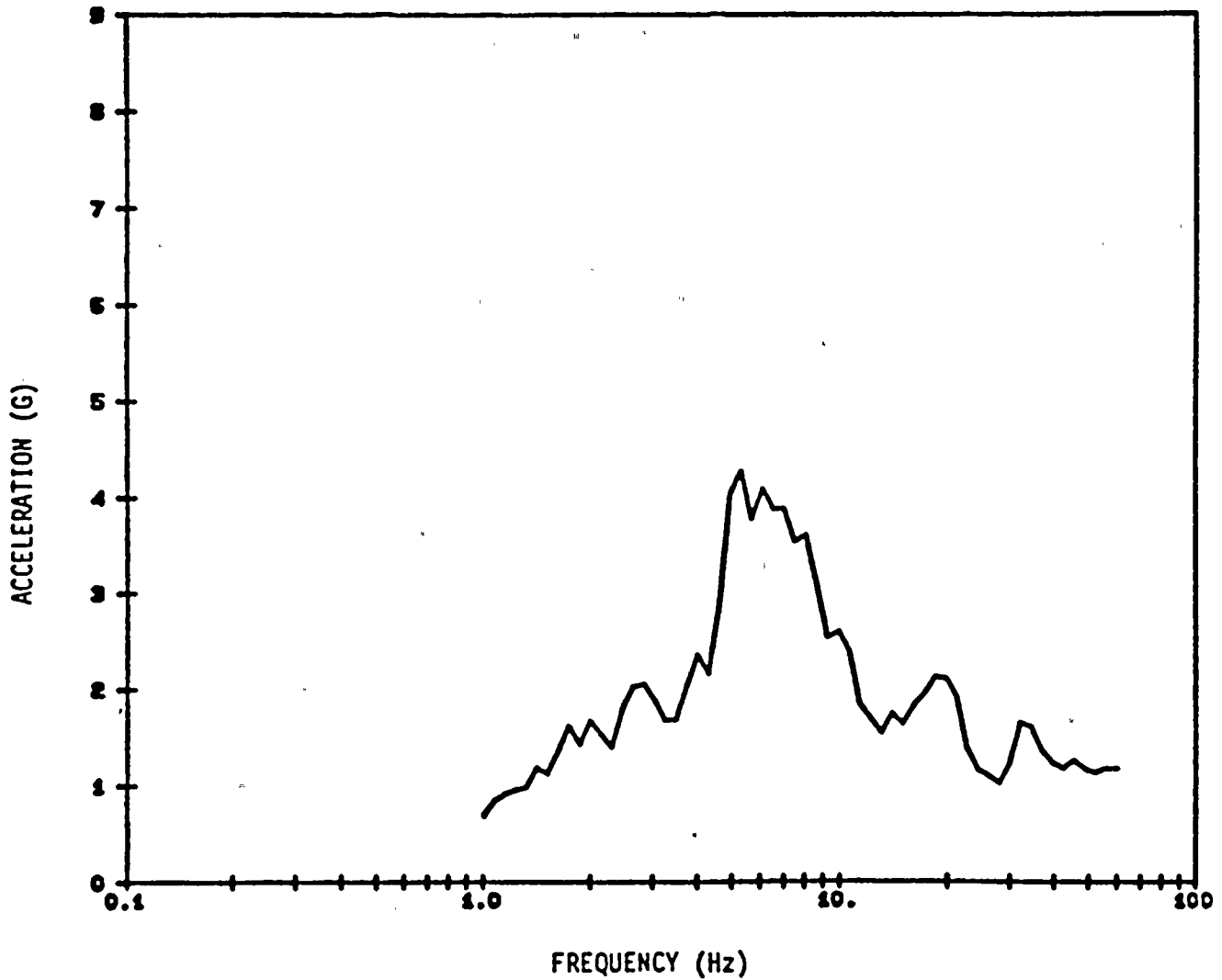


Figure 3-21. Dayhook, Scaled (X1.7), Component N80%; Baseline Corrected, 5% Damped Spectral Acceleration - Record 21 Scaled to  $S_a = 3.0g$



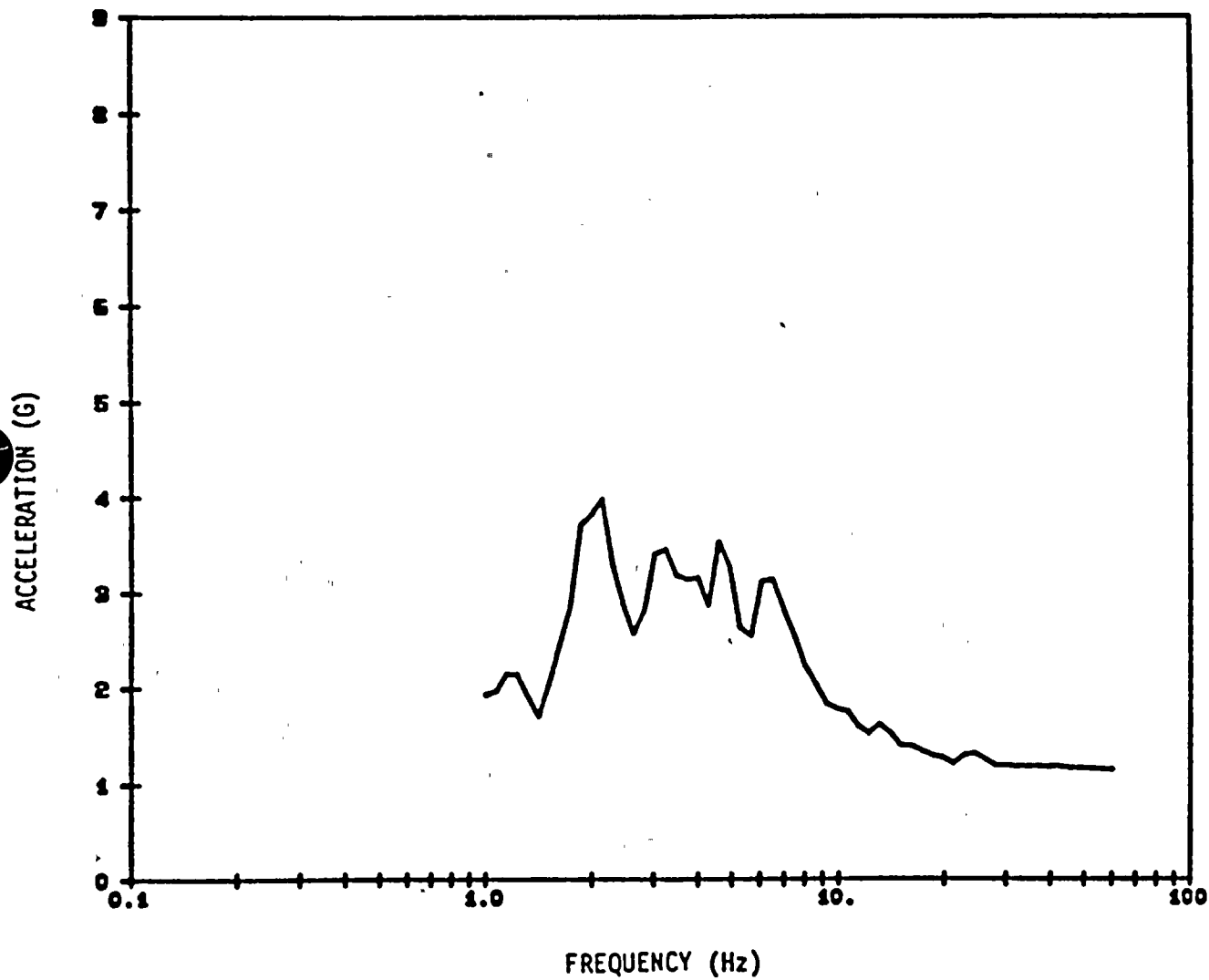


Figure 3-22. DCP, North M=7.0, Strike Slip Bilateral, 5% Damped Spectral Acceleration - Record 22 Scaled to  $S_a = 3.0g$



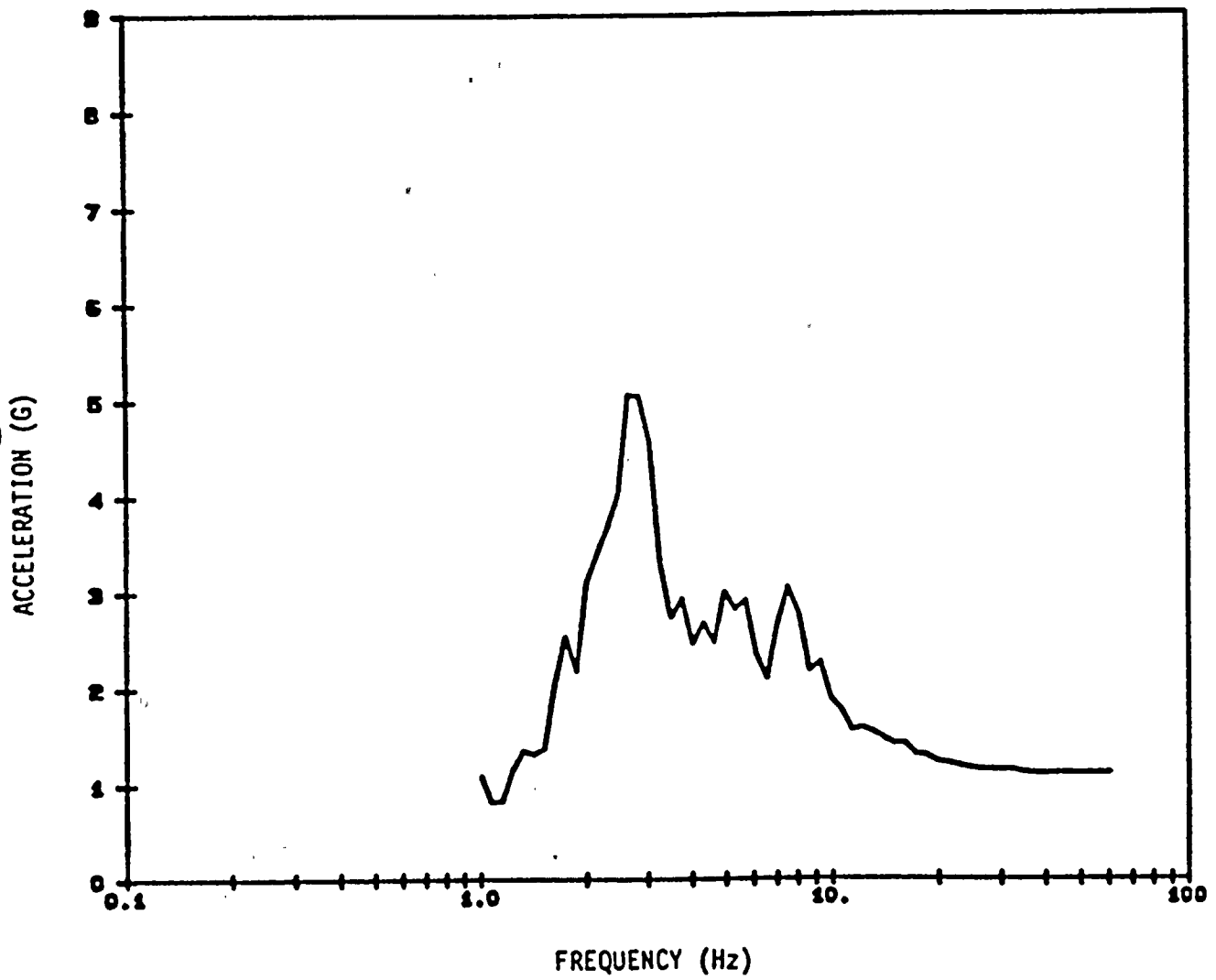


Figure 3-23. DCP East M=7.0, Strike Slip Bilateral, 5% Damped Spectral Acceleration  
- Record 23 Scaled to  $\bar{S}_a = 3.0g$



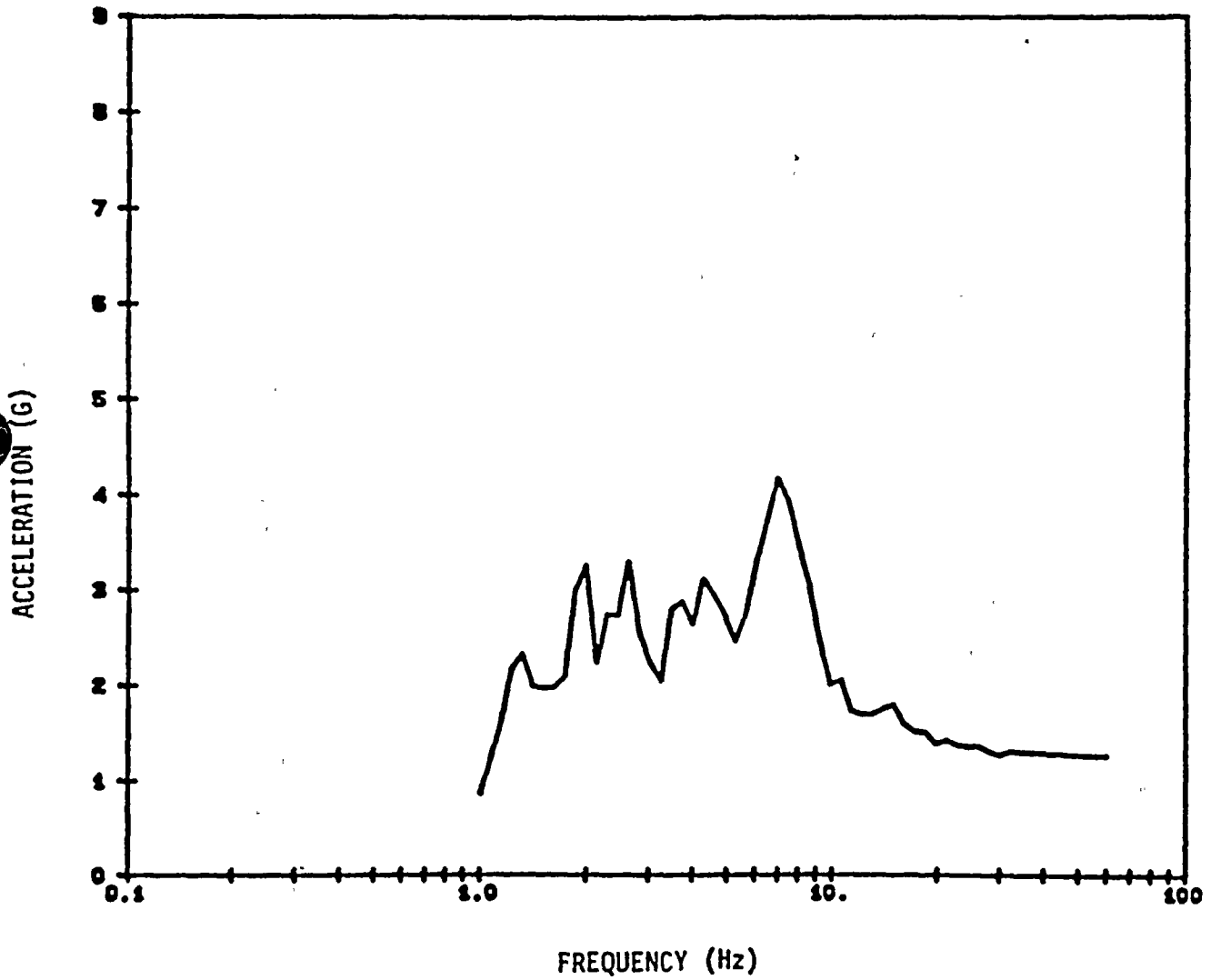


Figure 3-24. DCP North M=7.0 Strike Slip Unilateral, 5% Damped Spectral Acceleration  
- Record 24 Scaled to  $\bar{S}_a = 3.0g$



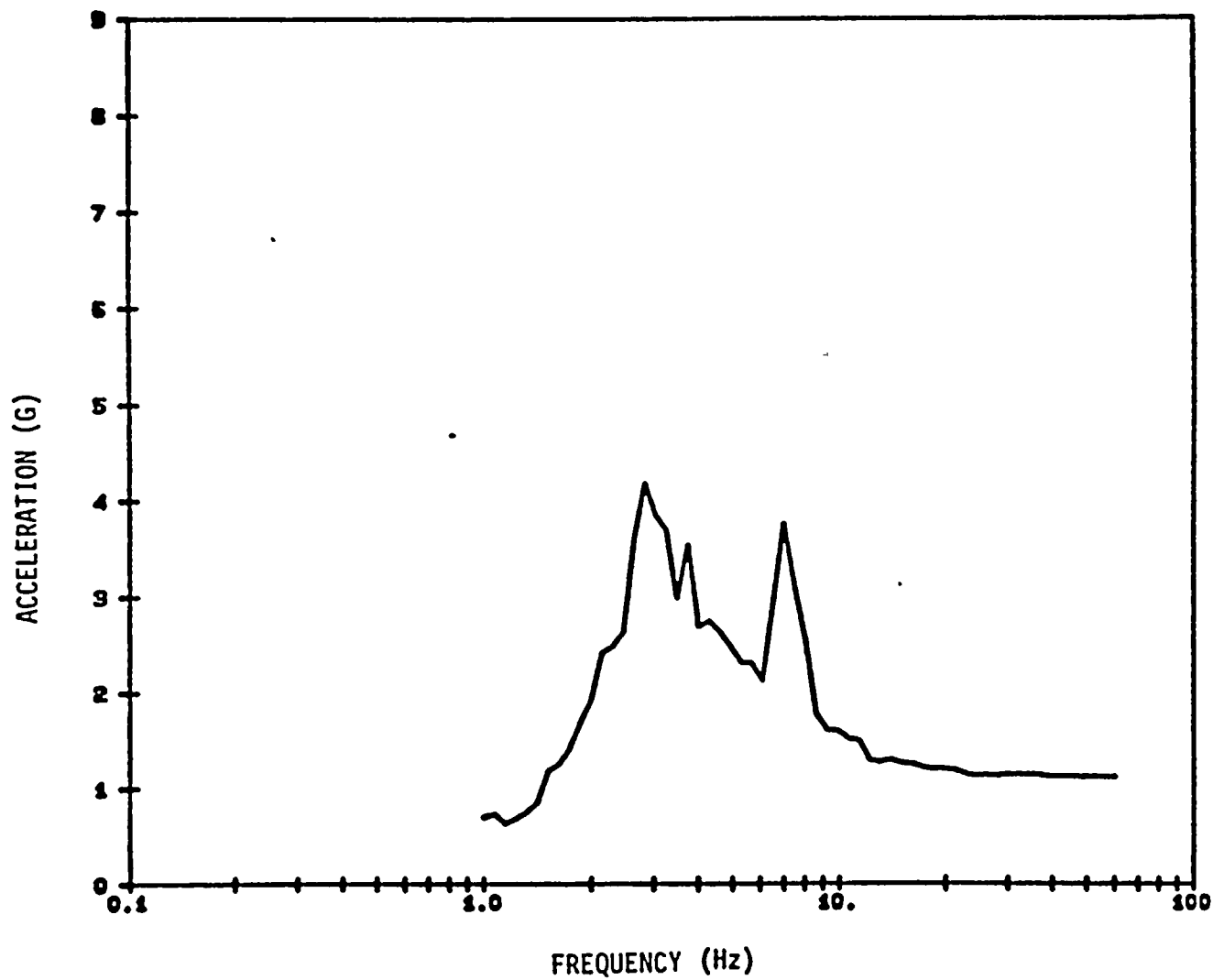


Figure 3-25. DCP East M=7.0 Strike Slip Unilateral, 5% Damped Spectral Acceleration  
- Record 25 Scaled to  $\xi_a = 3.0g$



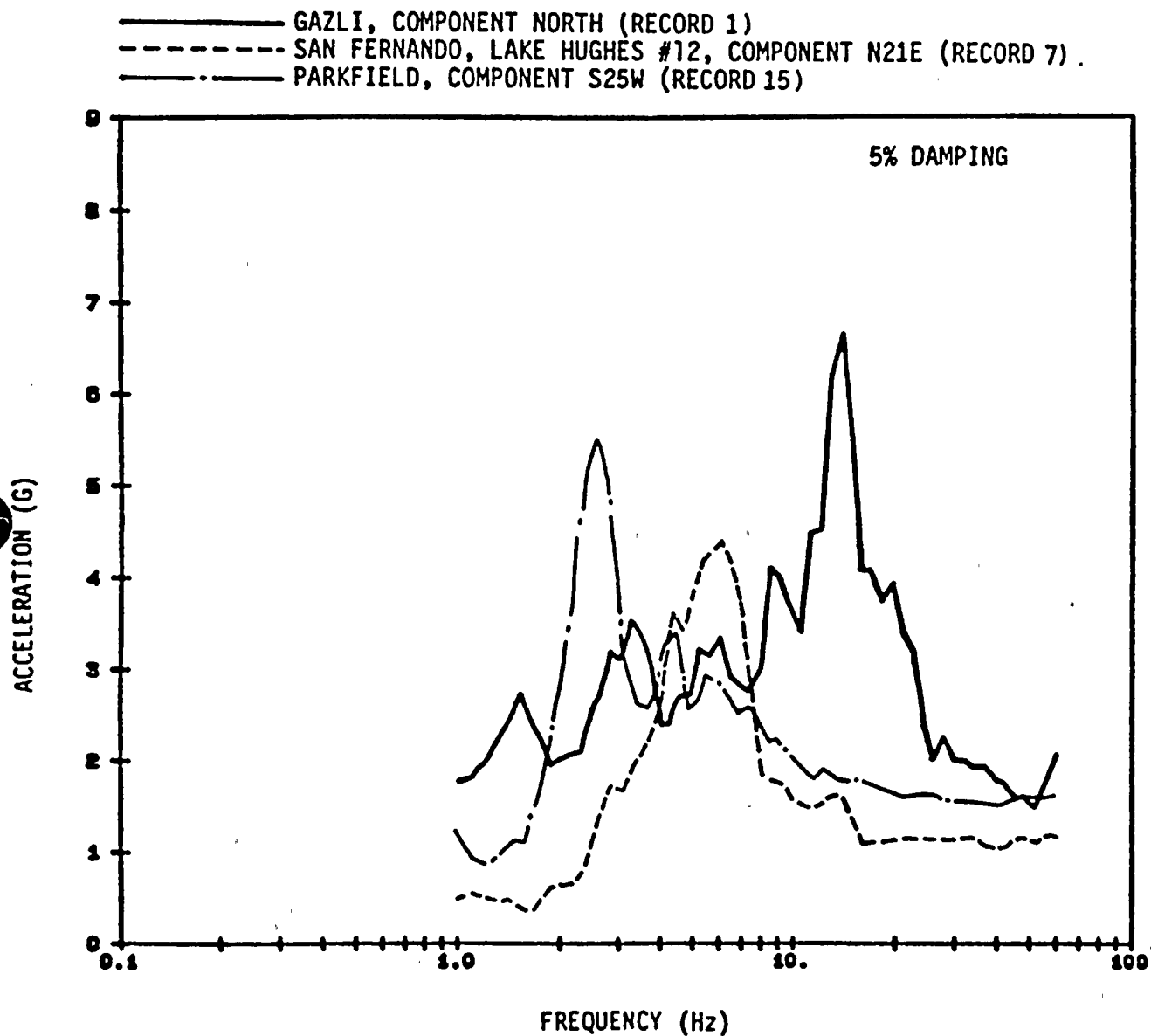


Figure 3-26. Acceleration Response Spectra for Three Empirical Records Scaled to an Average Spectral Acceleration of 3.0g Over the Frequency Range of 3 to 8.5 Hertz



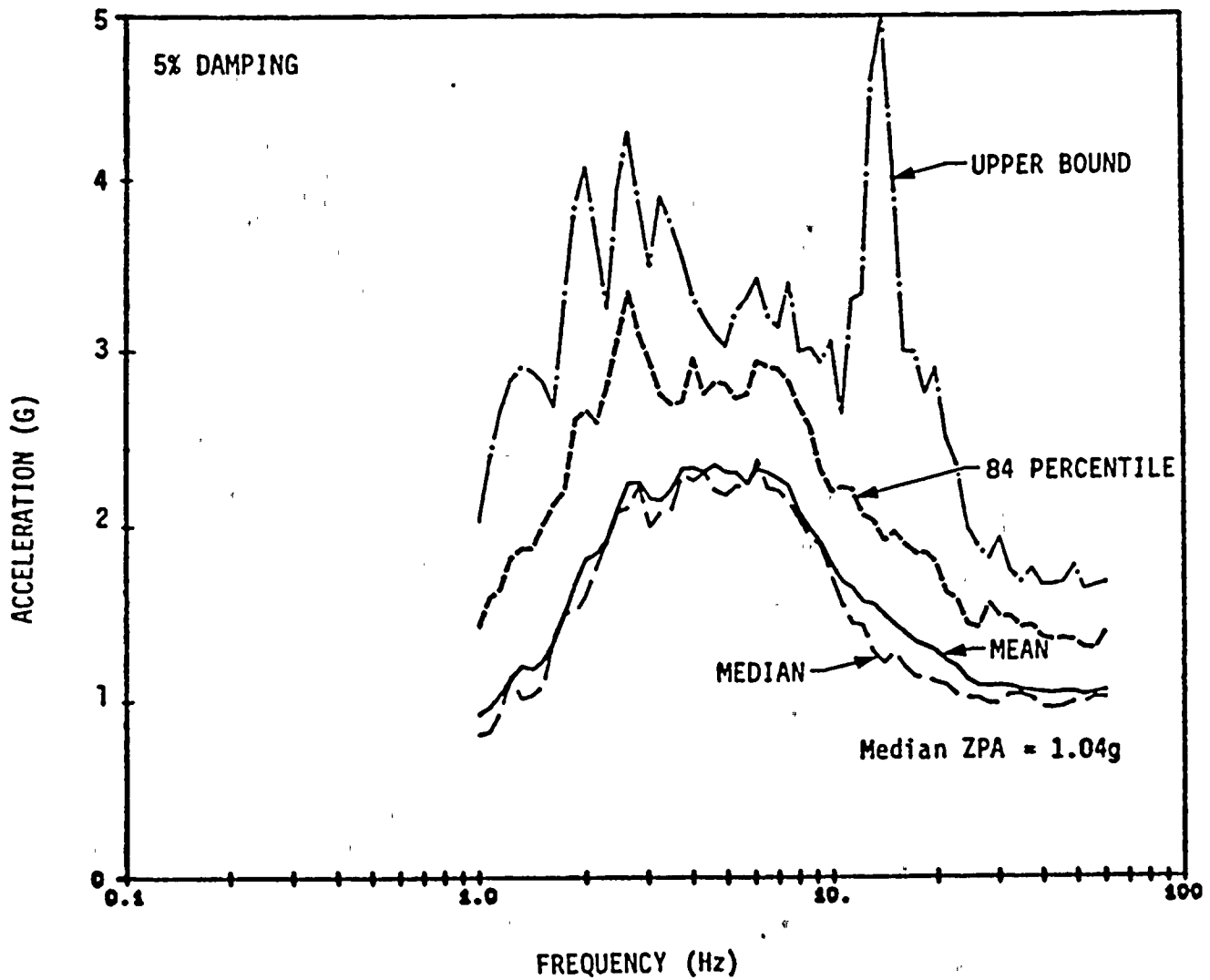


Figure 3-27. Mean, Median, 84% NEP, and Upper Bound Spectra for Ensemble of 25 Scaled Records ( $\bar{S}_a = 2.25g$ )



Table 3-1. Earthquake Time - Histories

EARTHQUAKE DATE	MAGNITUDE	RUPTURE MECHANISM	RECORDING STATION SITE CONDITIONS DISTANCE	T. HISTORY NUMBER	COMP	ORIGINAL RECORD			TIME HISTORY ADJUSTMENTS	MODIFIED RECORD			
						PEAK ACCEL. (G)	PEAK VELOC. Cm/Sec	V/A CM/SEC G		PEAK ACCEL. (G)	PEAK VELOC. (Cm/Sec)	V/A CM/SEC G	S <sub>A</sub> 13-0.5 MZ (G)
GAZLI, U.S.S.R. 17 MAY 1976	MS = 7.0 ML = 6.4	REVERSE	KARAKYR POINT ROCK/STIFF ALLUV. 3 KM	2	EAST NORTH	0.70	47.2	68	NONE	0.70	47.2	68	1.33
				1		0.66	44.4	68		0.66	44.4	68	1.31
TABAS, IRAN 16 SEP 1978	MS = 7.5 ML = 6.6	THRUST	TABAS STIFF ALLUV./ROCK 3 KM	4	TRAN LONG	0.70	105	150	NONE	0.70	105	150	2.48
				3		0.81	91.5	113		0.81	91.5	113	2.27
SAN FERNANDO, CA 09 FEB 1971	MS = 6.6 ML = 6.4	THRUST	PACOIMA DAM ROCK, 3 KM	5	S16E S74W	1.17	114	97	NONE	1.17	114	97	2.00
				6		1.08	58.3	54		1.08	58.3	54	1.89
			LAKE HUGHES #12 ROCK, 20 KM	7	N21E N69W	0.37	14.7	40	DISTANCE	0.94	36.8	40	2.38
				8		0.29	12.8	44		0.72	32.0	44	2.27
				9		N69W	0.29	27.8		96	DISTANCE	0.92	89.0
IMPERIAL VALLEY, CA 15 OCT 1979	MS = 6.9 ML = 6.6	STRIKE- SLIP	DIFFERENTIAL ARRAY DEEP ALLUVIUM 5 KM	10	N00E N90W	0.49	42.5	87	SITE RESPONSE	0.57	31.7	56	1.38
				11		0.35	67.8	192		0.51	40.2	78	1.55
			EL CENTRO #4 DEEP ALLUVIUM 4 KM	12	S50W S40E	0.37	77.6	210	SITE RESPONSE	0.37	34.8	94	0.75
				13		0.49	37.1	76		0.53	31.0	58	1.16
PARKFIELD, CA 27 JUN 1966	MS = 6.4 ML = 5.6	STRIKE- SLIP	TEMLOR ROCK, 10 KM	14	N65W S25W	0.28	14.5	51	DISTANCE & MAG.	0.55	47.9	87	1.27
				15		0.41	22.5	55		0.70	58.7	83	1.33
MORGAN HILL, CA 24 APR 1984	MS = 6.1 ML = 6.2	STRIKE- SLIP	COYOTE LAKE DAM ROCK, 0.1 KM	16	N75W S15W	1.30	79.7	61	MAGNITUDE	1.66	124	74	2.29
				17		0.71	51.9	73		0.89	85.7	97	1.95
COALINGA, CA 02 MAY 1983	MS = 6.7 ML = 6.5	REVERSE	PLEASANT VALLEY PUMP STATION (SWITCHYARD) STIFF ALLUV./ROCK 10 KM	18	N45E S45E	0.61	73.9	121	DISTANCE	0.85	103	121	1.63
				19		0.53	39.5	75		0.74	55.3	75	2.38
TABAS, IRAN 16 SEP 1978	MS = 7.5 ML = 6.6	THRUST	DAYHOOK ROCK, 17 KM	20	TRAN LONG	0.39	27.5	70	DISTANCE	0.66	46.8	70	1.12
				21		0.38	36.7	97		0.64	62.4	97	1.67
HOSGRI	MS = 7.0	STRIKE- SLIP	-	22	NORTH EAST	0.45	48.6	108	-	0.45	48.6	108	1.16
				23		0.54	43.4	80		0.54	43.4	80	1.47
				BILATERAL STRIKE- SLIP UNILATERAL		24	NORTH EAST	0.42		41.8	100	-	0.42
25	0.58	38.4	66		0.58	38.4		66	1.56				

3-39



#### 4. LINEAR ELASTIC RESPONSE FOR MEDIAN GROUND MOTION INPUT

Linear elastic modal responses were previously defined in Table 2-6 while the 5% damped median ground spectrum for  $\bar{S}_a = 2.25g$  is shown in Figure 3-27. Using the square-root-sum-of-squares (SRSS) combination of modes, the modal results of Table 2-6 can be combined with the spectral accelerations from Figure 3-27 to estimate the elastic response of the Turbine Building for this spectrum shape. Correction must be made for the fact that median damping of the Turbine Building was defined to be 7% whereas Figure 3-27 is depicted in terms of 5% damped spectra. The resultant elastic computed responses (Demands) for  $\bar{S}_a = 2.25g$  are shown in Table 4-1. Yield capacities were previously defined in Table 2-3 and Figures 2-10 and 2-11 for the shear walls, operating floor and turbine pedestal, respectively. The ratios of Demand to Yield Capacity for each element are also shown in Table 4-1.

For the operating floor, the ratio of Demand to First-Yield Capacity (D/C) for  $\bar{S}_a = 2.25g$ , is 2.50. Factoring  $\bar{S}_a$  downward by the D/C ratio indicates that the operating floor will begin to yield at about  $\bar{S}_a = 0.90g$ . Thus, at  $\bar{S}_a = 2.25g$  the operating floor will deform well out onto the second slope of the force-deflection curve shown in Figure 2-10. As a result, the elastically computed drift for the operating floor of 1.57 inches is too low. Using simplified inelastic corrections based



upon the Newmark ductility approach, it is estimated that the operating floor will drift about 2.0 inches based upon median structural properties at  $\bar{S}_a = 2.25g$ .

As shown in Figure 2-10, even after the First-Yield Capacity, C, of 1210-Kips is reached for each of the four beam elements, the operating floor retains a stiffness of about 14% of the "elastic" stiffness. Thus, the operating floor continues to support additional inertial forces with increasing drift. There is no consequence of a computed elastic demand to First-Yield Capacity (D/C) ratio as high as 2.50 except that the operating floor drifts will exceed those computed based upon the initial elastic stiffness.

Based upon the D/C ratio of 0.68 shown in Table 4-1 for the turbine pedestal at  $\bar{S}_a = 2.25g$ , the turbine pedestal is expected to remain elastic up to an  $\bar{S}_a = 3.30g$ . At  $\bar{S}_a = 2.25g$ , the elastic drift of the turbine pedestal is 1.89 inches. Using an SRSS combination of the pedestal drift plus the estimated operating floor drift of 2.0 inches, the gap closure between the pedestal and the operating floor is estimated to be about 2.75 inches at  $\bar{S}_a = 2.25g$ , which is less than the available gap of 3.375 inches. Thus, at  $\bar{S}_a = 2.25g$ , it is not expected that the turbine pedestal will impact the operating floor for the median spectrum shape case. However, by extrapolation, impacts would be



expected to occur for  $\bar{S}_a = 3.0g$ . This expectation was not confirmed by the nonlinear analysis results since only a small fraction of the nonlinear  $\bar{S}_a = 3.0g$  trials resulted in impact. It was found that the SRSS combination of pedestal and operating floor drifts is excessively conservative since the pedestal and operating floor tend to remain more in-phase with each other so that relative drifts tend to be much less than predicted by the SRSS combination. Thus, standard techniques used with elastic analysis for estimating gap closures are too conservative for this case.

At  $\bar{S}_a = 2.25g$ , it is expected that the lower segment of both Walls 19 and 31 will slightly yield in shear because their D/C ratios slightly exceed unity. At higher  $\bar{S}_a$  levels, it can be expected, based on the linear analysis, that most of the inelastic shear wall drift will be concentrated within these lowest segments since the D/C ratios for these lower segments are substantially larger than for the higher segments. Similarly, flexural yielding would not be expected except possibly in the middle section of Wall 19 because the flexural D/C ratios are much less than the shear D/C ratios for all other segments. Both of these expectations were confirmed by the nonlinear analyses. Lastly, one would expect roughly equal maximum nonlinear drifts for Walls 19 and 31 because the D/C ratios in shear for these two walls are similar. This expectation was not confirmed by the nonlinear analysis results. In



nearly every case, the maximum nonlinear drifts occurred in the lowest segment of Wall 31. Within Wall 19, however, the nonlinear drifts spread more throughout the wall height, although they were still predominantly in the lowest segment. This slightly greater spreading of drifts over the height provided some protection for the lowest segment of Wall 19 which was not evident for the lowest segment of Wall 31. The elastically computed D/C ratios presented in Table 4-1 do not provide any clue as to why drifts were more concentrated into the lowest segment of Wall 31 than for Wall 19. Thus, the linear elastic results summarized in Table 4-1 provide considerable, but not complete, insight into the nonlinear performance of the Turbine Building at  $\bar{S}_a = 3.0g$  and greater.



Table 4-1. Elastically Computed Response for Figure 3-27  
Median Spectrum Scaled to  $\bar{S}_a = 2.25G$

LOCATION	DRIFTS (INCHES)
TOP OF PEDESTAL	1.89
CENTER OF OPERATING FLOOR	1.57** (2.00)
WALL 19	
EL 140	0.26
EL 123	0.16
EL 104	0.06
WALL 31	
EL 140	0.27
EL 119	0.18
EL 107	0.12

\*Revised to 7% damping

\*\* Operating floor is actually highly inelastic so this elastic computed drift is too small. Value in parenthesis is more realistic for inelastic operating floor.

ELEMENT	SHEAR $V_R$ (Kips)	$\frac{V_R}{V_Y}$	MOMENT $M_R$ (Kip-Ft. x $10^6$ )	$\frac{M_R}{M_Y}$
TURBINE PEDESTAL	45,400	0.68	--	--
WALL 19				
OPERATING FLOOR (PER BEAM)	2,910	2.41	--	--
EL 123+	9,520	0.90	.16	.70
EL 104+	10,240	0.93	.36	.91
EL 85+	10,820	1.18	.55	.77
WALL 31				
OPERATING FLOOR (PER BEAM)	3,030	2.50	--	--
EL 119+	12,330	0.93	.26	.40
EL 107+	14,560	0.86	.43	.59
EL 85+	16,460	1.10	.78	.74



## 5. NONLINEAR ANALYSES WITH MEDIAN STRUCTURE PROPERTIES

### 5.1 Results

Twenty-five nonlinear time history analyses were performed at both  $\bar{S}_a = 3.0g$  and  $\bar{S}_a = 6.0g$  using the median structure properties defined in Section 2 and the 25 time-histories of input defined in Section 3. Results of the analyses are summarized in Tables 5-1 and 5-2 for  $\bar{S}_a$  of 3.0g and 6.0g, respectively. These tables list the maximum total drift at the top of both Walls 19 and 31, the operating floor, and the turbine pedestal. In some cases, the two operating floor beams do not displace the same amount, particularly at the  $\bar{S}_a = 6.0g$ ; thus the values listed are the average of the two beams which is judged to be a better indicator of their inertial effect on the shear walls. Also shown are the maximum story drifts for each wall defined as a percentage of the wall segment (story) height. In nearly every case, the maximum story drifts occurred in the lowest segment of each wall. Tables 5-1 and 5-2 also indicate for which cases the turbine pedestal impacted the operating floor. Lastly, the probability of severe shear wall distress is estimated for each trial using the random shear wall distress criteria defined by Equation 2-5. Defining  $P_{F_i}$  as the probability of severe distress for Trial  $i$ , the median estimate of the probability  $P_F$  of severe distress for each  $\bar{S}_a$  value is obtained from:



$$P_F = \frac{\sum_{i=1}^N P_{F_i}}{N} \quad (5-1)$$

where N is the number of trials or 25 for these cases.

The following points should be noted from Tables 5-1 and 5-2:

1. Both maximum story drifts and total drifts of Wall 31 tend to exceed those drifts for Wall 19 despite the fact that the elastic computed Demand/Capacity ratio tends to be greater for Wall 19 (Table 4-1). Drifts for Wall 31 are greater than for Wall 19 for 22 (88%) of the 3.0g cases and all 25 (100%) of the 6.0g cases.
2. The number of cases of pedestal impact are much fewer than might be expected from comparing the operating floor and turbine pedestal drifts with the available gap (3.375 inches). The operating floor and turbine pedestal were always partially in-phase at the times of maximum drifts so that their individual drifts should not be combined for comparison with the available gap. In fact, the operating floor tended to drift into the pedestal. Thus, rather than



the pedestal loading the operating floor and causing it to drift further, the opposite occurs. The turbine pedestal tends to stabilize the operating floor and prevent it from drifting further. This situation is the opposite of what was expected prior to performing the analyses. At  $\bar{S}_a = 3.0g$ , impact occurred in only 9 cases (36%) and never occurred when the operating floor drifts were less than the gap size (3.375 inches). Even for the 11 trials where the operating floor drift ranged between 1.0 and 1.67 times the gap size, impact only occurred in 7 cases (64%). For the two cases where operating floor drifts exceeded 1.67 times the gap size, impact did occur. Even at  $\bar{S}_a = 6.0g$ , impact did not occur in 3 out of the 5 trials for which the operating floor drifted less than 1.67 times the gap size. Thus, in summary:

$$\frac{\text{Operating Floor Drift}}{\text{Gap Size}} \leq 1.0 \quad \text{No Impact} \quad (5-2)$$

$$\frac{\text{Operating Floor Drift}}{\text{Gap Size}} \geq 1.67 \quad \text{Impact}$$

3. At  $\bar{S}_a = 3.0g$ , the maximum story drift was less than 0.45% of the story height for all but 3 of the trials. Thus, in 22 cases (88%), the median (randomness only) probability of severe distress was essentially zero. Even in the worst case



(Trial 18), the maximum story drift was only 0.69% which corresponds to a 46% median probability of severe distress for this case. The overall median (randomness only) probability of severe distress was only 3.1% for the 25 equally weighted trials.

4. At  $\bar{S}_a = 6.0g$ , only 7 trials (28%) produced maximum story drifts less than 1.1% of the story height which corresponds to a median (randomness only) probability of severe distress of essentially 100%. Thus, for 72% of the trials, severe distress is nearly certain. However, in the lowest case (Trial 11); the maximum story drift was only 0.57% which corresponds to a median (randomness only) probability of severe distress of 9%. The 4 lowest cases (Trials 7, 8, 11, and 21) at  $\bar{S}_a = 6.0g$  produced approximately the same drifts as the three highest cases (Trials 15, 18, and 20) at  $\bar{S}_a = 3.0g$ . This situation indicates the variability introduced when any single ground motion parameter is used to serve as a damage descriptor, even when a carefully chosen parameter such as  $\bar{S}_a$  is used. On the average,  $\bar{S}_a$  worked well even though considerable variability exists. At  $\bar{S}_a = 6.0g$ , the overall median probability of severe distress was 87.6% for the 25 equally weighted trials. Thus:



Randomness Only

$$\bar{S}_a = 3.0g: P_F = 3.1\% \text{ (Severe Distress Very Unlikely)}$$

(5-3)

$$\bar{S}_a = 6.0g: P_F = 87.6\% \text{ (Severe Distress Very Likely)}$$

5. In Section 2.3 it was discussed that the operating floor model began to err significantly (stiffness too high) when the computed operating floor relative drifts exceeded about 8.0 inches. For these cases, the operating floor drifts were underpredicted and the shear wall loads and drifts were slightly overpredicted. No such cases occurred at  $\bar{S}_a = 3.0g$ , however, at  $\bar{S}_a = 6.0g$ , this situation occurred in 12 of the 25 cases. The consequences of these occurrences on the previously summarized results was judged to be negligible. For all 12 cases, the maximum computed shear wall story drift was at least 1.21%, and the reported probability of shear wall distress was 100% in each case. It would be necessary to reduce the maximum shear wall drifts to less than 0.95% to have any significant influence on the reported probability of shear wall distress. This reduction is considered to be inconceivable even with the use of a more appropriate operating floor stiffness after relative drifts exceed about 8.0 inches.



For use in a Seismic Probabilistic Risk Assessment (SPRA), a fragility curve must be defined which provides the probability of severe distress as a continuous function of the ground motion level. However, nonlinear analyses were only made at two discrete ground motion levels corresponding to  $\bar{S}_a = 3.0g$  and  $6.0g$ . A continuous median (randomness only) fragility curve was estimated by interpolating and extrapolating the probability of severe distress values given in Equation 5-3. The median fragility curve was assumed to be lognormally distributed as has been common practice in most SPRA studies. Fitting the results given in equation 5-3 to a lognormal distribution, the median (randomness only) fragility curve is defined by the following median value,  $\bar{S}_a$ , and randomness logarithmic standard deviation,  $\beta_R$ :

Median (Randomness Only) Fragility Curve

$$\text{Median } \bar{S}_a^v = 4.60g$$

(5-4)

$$\beta_R = 0.23$$



Equation 5-4 leads to:

$\bar{S}_a$	Median $P_F$
3.15	5%
4.60	50%
6.70	95%

## 5.2 Prediction of Median (Randomness Only) Fragility From Elastic Results

In most cases, nonlinear time history results are not available from which to estimate the median (randomness only) fragility curve. As a result, the median fragility is normally estimated from an elastic analysis using the median input spectrum shape. With an available median-centered elastic analysis, such as that presented in Section 4, the median fragility curve in terms of  $\bar{S}_a$  can be estimated from:

$$\bar{S}_a = \frac{\bar{S}_{aR}}{(D/C)_R} F_\nu F_R \quad (5-5)$$

where  $\bar{S}_{aR}$  is the reference level at which the elastic analysis was performed,  $(D/C)_R$  is the Demand/Capacity ratio resulting in critical elements from a median centered analysis using  $\bar{S}_{aR}$ ,  $F_\nu$  is an estimated inelastic energy absorption factor, and  $F_R$  is an estimated response



factor. Both  $F_u$  and  $F_R$  are random variables which are typically assumed to be lognormally distributed with randomness logarithmic standard deviation,  $B_{R_u}$  and  $B_{R_R}$ , respectively.

For the elastic analysis presented in Section 4, the  $\bar{S}_{aR}$  was 2.25g. The D/C ratio is the ratio of the elastic computed Demand defined by  $V_R$  in Table 4-1 to the yield point capacity  $V_Y$ . As shown in Table 4-1, the  $(D/C)_R = V_R/V_Y$  ratio varies between elements. The  $(D/C)_R$  ratio for elements which control the damage state being considered should be used. In Table 4-1, the controlling elements are the lowest segments of Walls 19 and 31, for which the  $(D/C)_R$  ratios are 1.18 and 1.10, respectively. Since beneficial load redistribution would not be expected to occur between Walls 19 and 31, the higher  $(D/C)_R$  ratio of 1.18 for Wall 19 would normally be chosen for use in Equation 5-5. However, since the nonlinear analyses of the Turbine Building indicate that Wall 31 is actually more critical, the  $(D/C)_R$  ratio of 1.10 appropriate to this wall is used in Equation 5-5. This choice enables a direct comparison between the median fragility estimated from Equation 5-5 and that obtained from the nonlinear analysis (Equation 5-4).

Since the elastic analysis of Section 4 is median centered (median spectra shape, and median structure properties), the median value of  $F_R$  is unity. No structure property variation was included in the nonlinear



time-history analyses, so the only random variability to be included in  $F_R$  is the variability in spectral accelerations about the median at any specific frequency for the time histories which were used. It was noted in Section 3 that within the frequency range of primary interest (3.5 to 9 Hz) the ratio of the 84% NEP to median spectral acceleration was approximately 1.24. This ratio corresponds to a  $\beta_{R_R} = 0.215$  which is used herein.

Thus, from Equation 5-5, the following estimates for median fragility and variability are obtained:

$$\frac{V}{S_a} = \left( \frac{2.25g}{1.10} \right) F_{\mu}^V = 2.05g \cdot F_{\mu}^V \quad (5-6)$$

$$\beta_R = \left[ \beta_{R_{F_{\mu}}}^2 + \beta_{R_R}^2 \right]^{1/2} = \left[ \beta_{R_{F_{\mu}}}^2 + (0.215)^2 \right]^{1/2}$$

The only remaining task is to estimate the median value  $F_{\mu}^V$  and randomness variability  $\beta_{R_{F_{\mu}}}$ .

Throughout this report, damage is defined in terms of story drifts,  $\delta_T$ . For each wall segment, the story drift can be converted to story ductility  $\mu_s$  by:

$$\mu_s = \frac{\delta_T}{\delta_Y} \quad (5-7)$$



where  $\delta_Y$  is the elastic yield drift as given by:

$$\delta_Y = \frac{V_Y}{K} \quad (5-8)$$

and the Concrete Capacity  $V_C$  is conservatively substituted for the Yield Capacity  $V_Y$  as discussed later in this section. Values of  $V_C$  and  $K$  are listed in Tables 2-3 and 2-4, respectively. For the bottom segment of Wall 31,  $\delta_Y = 0.113$  inches or 0.043% of the segment height. Thus, a maximum drift of 0.7% corresponds to a maximum story ductility  $\mu_S$  of 16.4 for the bottom segment of Wall 31. However,  $F_u$  relates to the system ductility  $\mu$  which is always equal to or less than the maximum story ductility  $\mu_S$  of the critical segment.

The system ductility  $\mu$  is estimated from:

$$\mu = \frac{\sum W_i \delta_{T_i}}{\sum W_i \delta_{e_i}} \quad (5-9)$$

where  $W_i$  are the inertial weights influencing the drift of the critical wall segment,  $\delta_{T_i}$  are the estimated maximum total drifts of each of these weights corresponding to  $\delta_T$  or  $\mu_S$  being reached in the critical wall segment, and  $\delta_{e_i}$  are the elastically computed drifts of each of these weights scaled to  $\delta_Y$  being reached in the critical wall segment.



The solution of Equation 5-9 requires the exercising of judgement in the selection of inertial weights to be included and in estimating the inelastic deformed shape  $\delta_T$  from the elastic deformed shape  $\delta_{e_i}$ . If  $\delta_{T_i}$  were proportional to  $\delta_{e_i}$  at all locations of interest, then  $\mu = \mu_s$ . However, the inelastic portion of  $\delta_{T_i}$  tends to concentrate within segments with the highest  $(D/C)_R$  ratios such that  $\delta_{T_i}$  is not normally proportional to  $\delta_{e_i}$ , and therefore, Equation 5-9 produces  $\mu$  estimates which are much lower than  $\mu_s$ . This situation is particularly true when the highest  $(D/C)_R$  ratio is near the base of the structural model as is the case for the Turbine Building shear walls.

From Table 2-6, it can be seen that the shear in the bottom segment of Wall 31 comes primarily from the third mode. As also seen in Table 2-6, neither the operating floor weight nor Wall 19 participate to any great extent in this mode. Therefore, only the three nodal weights (Nodes 16, 18, and 20) on Wall 31 are included in the solution of Equation 5-9.

The maximum deformation results produced from each nonlinear time-history analysis as tabulated in Tables 5-1 and 5-2 are used to estimate the inelastic deformed shape,  $\delta_{T_i}$ , for the three nodes on Wall 31. Admittedly, this decision makes this analysis a "post-prediction" since this information is not normally available when Equation 5-9 is used.



However, this decision also enables the most direct comparison of Equation 5-6 with the nonlinear results. The elastic deformed shape  $\delta_{e_1}$  used is that given in Table 4-1 scaled so that the bottom element undergoes the yield displacement of 0.113 inches. The elastic deformed shape and inelastic deformed shape used for several different drift levels are given in Table 5-3. The first case in Table 5-3 is the elastic case scaled to the yield drift and corresponds to an  $\bar{S}_a = 2.05g$ . The second case represents the median deformed shape for  $\bar{S}_a = 3.0g$  from Table 5-1, while the last case represents the median deformed shape for  $\bar{S}_a = 6.0g$  from Table 5-2. The third and fourth cases correspond to maximum story drifts in the bottom segment of Wall 31 of 0.40% and 0.70%, respectively. The deformed shapes given in Table 5-3 for these two cases were estimated using the deformed shapes in Tables 5-1 and 5-2 for trials with similar levels of bottom segment drifts. Also shown in Table 5-3 are the story drift ductilities  $\mu_s$  from Equation 5-7 and the system ductilities  $\mu$  from Equation 5-9 for each of five cases.

NUREG/CR-3805 (Reference 4) recommends a Spectral Averaging Method for estimating  $F_\mu$  for any given  $\mu$ . First the ratio of secant to elastic stiffness is estimated from:

$$\frac{K_s}{K} = \frac{1 + s(\mu-1)}{\mu} \quad (5-10)$$



where  $s$  is the ratio of the second slope stiffness to elastic stiffness on the force-deflection diagram (see Figures 2-6, 2-7, or 2-8). Next, the secant frequency  $f_s$  to elastic frequency  $f$  ratio is estimated from:

$$\frac{f_s}{f} = \sqrt{K_s/K} \quad (5-11)$$

Spectral accelerations are then averaged over a frequency band extending from an upper frequency,  $f_u$ , to the secant frequency,  $f_s$ , where  $f_u$  is from:

$$\frac{f_u}{f} = (1-B) + B \left( \frac{f_s}{f} \right) \quad (5-12)$$

$$B = 2C_F \left( 1 - \frac{f_s}{f} \right) - 1 \quad (5-13)$$

except that  $0 \leq B \leq 0.7$

The coefficient  $C_F$  is a function of ground motion duration; however for longer duration records such as those used herein,  $C_F$  is approximately 2.3. This frequency band is centered on an effective frequency  $f'_{ea}$  given by:

$$f'_{ea} = \frac{f_u + f_s}{2} \quad (5-14)$$



The inelastic energy absorption factor is then given by:

$$F_u = \nu \left( \frac{f'_{ea}}{f} \right)^2 \frac{S_a(f, \beta)}{S_a(f_u - f_s, \beta'_{ea})} \quad (5-15)$$

where  $S_a(f, \beta)$  is the spectral acceleration at the elastic frequency,  $f$ , and damping,  $\beta$ , and  $\overline{S_a(f_u - f_s, \beta'_{ea})}$  is the average spectral acceleration over the frequency band from  $f_u$  to  $f_s$  at an effective damping,  $\beta'_{ea}$ , given by:

$$\beta'_{ea} = \left( \frac{f_s}{f'_{ea}} \right)^2 [\beta + \beta_H] \quad (5-16)$$

$$\beta_H = C_N \left( 1 - \frac{f_s}{f} \right) \quad (5-17)$$

The coefficient  $C_N$  is also a function of the ground motion duration, but can be approximated as  $C_N = 0.11$  for the longer duration records used in this study.

The third mode frequency which dominates shears in the bottom segment of Wall 31 is 8.6 Hz and the elastic damping,  $\beta$ , was taken to be 7%. Table 5-4 presents  $F_u$  values obtained by the Spectral Averaging Method (Equations 5-10 through 5-17) together with intermediate parameters for the 5 cases listed in Table 5-3. Also shown are the  $\overline{S_a}$  values obtained



from Equation 5-6 and a comparison with the nonlinear time-history results for Cases 2 (3.0g) and 5 (6.0g) where such results are available. For Case 2, the Spectral Averaging Method estimates an  $\bar{S}_a$  of 2.67g versus the actual 3.0g or an 0.89 ratio of predicted to actual. For Case 5, the Spectral Averaging Method predicts  $\bar{S}_a = 6.27g$  versus the actual 6.0g or a 1.05 ratio of predicted to actual. For the case of 0.7% maximum story drift corresponding to 50% probability of severe wall distress, the Spectral Averaging Method predicts  $\bar{S}_a = 4.30g$ . Although actual nonlinear analyses do not exist for this case, a median estimate of  $\bar{S}_a^v = 4.60g$  was presented in Equation 5-4 for 50% probability of severe wall distress. The estimate provided by the Spectral Averaging Method is 4.30g or 93% as large. In conclusion, it is judged that the Spectral Averaging Method provides an excellent, but slightly conservative prediction of the median fragility.

The Riddell-Newmark Method (Reference 6) has been more commonly used in SPRA studies to estimate  $F_u$  and  $\bar{S}_a$ . This method is substantially easier to use. However, NUREG/CR-3805 (Reference 4) shows that the Riddell-Newmark Method is unconservatively biased for shear wall hysteresis behavior, particularly for the longer duration ground motion records. Also, at higher  $F_u$  levels, the Riddell-Newmark Method produces about twice the coefficient of variation for predicted versus actual  $F_u$  than does the previously described Spectral Averaging Method. Even so, because of its greater simplicity, the Riddell-Newmark Method was also investigated.



In the Riddell-Newmark Method,  $F_{\nu}$  is given by:

$$F_{\nu} = \text{larger of } F_{\nu_1} \text{ or } F_{\nu_2} \quad (5-18)$$

$$F_{\nu_1} = \text{smaller of } F_{\nu_3} \text{ or } F_{\nu_4}$$

in which  $F_{\nu_2}$ ,  $F_{\nu_3}$ , and  $F_{\nu_4}$  apply to different frequency ranges. For 7% damping, those values are given by:

$$\begin{array}{l} \text{ZPA Limit} \\ F_{\nu_4} = \frac{S_{a(f,\beta)}}{\text{ZPA}} \nu^{0.11} \end{array} \quad (5-19)$$

$$\begin{array}{l} \text{Acceleration Range} \\ F_{\nu_3} = (2.673\nu - 1.673)^{0.411} \end{array} \quad (5-20)$$

$$\begin{array}{l} \text{Velocity Range} \\ F_{\nu_2} = (2.240\nu - 1.240)^{0.611} C_f \end{array} \quad (5-21)$$

$$\text{When } \left(\frac{f_k}{f}\right) < 1.0 \quad : \quad C_f = \left(\frac{f_k}{f}\right)$$

$$\left(\frac{f_k}{f}\right) \geq 1.0 \quad : \quad C_f = 1.0$$

in which  $f_k$  is the knuckle frequency between the zone of approximately



constant amplified spectral acceleration and the zone of approximately constant amplified spectral velocity. For the medium spectrum shown in Figure 3-27 and used herein,  $f_k = 2.7$  Hz; whereas  $f = 8.6$  Hz, so that  $F_{\mu_2}$  will only govern in Equation 5-18 at very large values of  $\mu$ . For 7% damping, the ratio  $\frac{S_a(f, \beta)}{ZPA}$  at  $f = 8.6$  Hz is  $(\frac{1.75}{1.04}) = 1.68$  for the median spectrum shown in Figure 3-27. In this case when,

$$\mu \leq 2.3 \quad F_{\mu_3} \text{ CONTROLS}$$

$$2.3 \leq \mu \leq 11.3 \quad F_{\mu_4} \text{ CONTROLS}$$

$$\mu \geq 11.3 \quad F_{\mu_2} \text{ CONTROLS}$$

As described above, the Riddell-Newmark Method does not take any credit for the second slope ( $sK$ ) of the force-deflection diagram (Figure 2-6). The effect of this second slope can be significant when either  $\mu$  is large (as is the case herein) or when  $s$  is not close to zero (as is the case for the Operating Floor). Often for concrete shear wall structures, the yield capacity  $V_y$  is defined in terms of the concrete-only (capacity  $V_c$ ), and the second slope  $s$  and the extent of this slope to the ultimate capacity  $V_u = V_c + V_s$  is defined by the amount of shear load carried in the steel. When the second slope is ignored as above, the dichotomy is that the steel capacity, which is actually very



beneficial, is being ignored. This effect is automatically considered in the Spectral Averaging method in the definition of the secant stiffness by Equation 5-10. It may also be considered in the Riddell-Newmark Method by replacing the actual force-deflection diagram with a pseudo elastic perfectly plastic diagram having the same area and the same capacity  $V_{\mu}$  as that of the actual diagram at a displacement of  $\mu\delta_y$ . This replacement is illustrated in Figure 5-1. The capacity ratio, R, then becomes:

$$R = \frac{V}{V_y} = 1 + s(\mu-1) \quad (5-22)$$

and the pseudo ductility factor  $\mu'$  for the elasto-perfectly plastic relationship of equal area is:

$$\mu' = 0.5 + \frac{(\mu-1)(1+R) + 1}{2R^2} \quad (5-23)$$

With these modifications, a reduced  $F_{\mu}'$  is obtained from Equation 5-18 through 5-20 by substituting  $\mu'$  for  $\mu$ . The Modified Riddell-Newmark  $F_{\mu}$  value is then defined by:

$$F_{\mu} = F_{\mu}' \cdot R \quad (5-24)$$



The modification of Equation 5-24 is necessary because the Demand/Capacity ratio was defined in terms of  $V_y$ . Alternately,  $F'_\mu$  can be used directly by redefining the D/C ratio in terms of the  $V_\mu$  capacity. Both alternatives lead to the same result. The first alternative is used herein so that D/C remains the same for the Spectral Averaging, Riddell-Newmark, and Modified Riddell Newmark Methods (i.e., the entire differences are included in  $F'_\mu$  for ease of comparison).

Table 5-5 presents  $F'_\mu$  and  $\bar{S}_a$  results obtained for the four inelastic cases of Table 5-3 based on the Spectral Averaging, the Riddell-Newmark, and the Modified Riddell-Newmark Methods. Again, it should be noted that the  $\mu = 3.3$  case corresponds to  $\bar{S}_a = 3.0g$  and the  $\mu = 23.2$  case corresponds to  $\bar{S}_a = 6.0g$ . Therefore, these two cases can be used to judge the accuracy of each of the three methods for estimating  $F'_\mu$ . Also, the  $\mu = 11.5$  case corresponds to a maximum story drift of 0.7% which relates to the 50% probability of severe distress previously estimated from the nonlinear run to be  $\bar{S}_a^v = 4.6g$ .

At  $\mu = 3.3$ , the Spectral Averaging Method underpredicts  $\bar{S}_a$  by 11%, the Riddell-Newmark Method overpredicts by 31%, and the Modified Riddell-Newmark overpredicts by 39%. At  $\mu = 23.2$ , the Spectral Averaging Method overpredicts by 4%, the Riddell-Newmark Method overpredicts by 18%, and the Modified Riddell-Newmark overpredicts by 25%. Comparing each



method's results with the estimated  $\bar{S}_a^v = 4.6g$  at  $\mu = 11.5$ , it appears that the Spectral Averaging Method underpredicts by 7%, the Riddell-Newmark Method underpredicts by 2%, and the Modified Riddell-Newmark Method overpredicts by 23% for this case. It can be seen that the Riddell-Newmark and more so the Modified Riddell-Newmark Methods tend to substantially overpredict the  $\bar{S}_a$  capacity. For severely pinched shear wall hysteretic behavior and longer duration time-histories of input, this same tendency to overpredict inelastic capacities was found and reported in NUREG/CR-3805 (Reference 4). However, since this overprediction is consistent, it can be removed through the use of an effective  $F_{\nu_e}$ , which is related to  $F_{\nu}$  reduced by a duration factor  $C_D$ .

Since the Modified Riddell-Newmark more properly accounts for the influence of the second slope stiffness,  $sK$ , this method is corrected for the duration and pinched hysteresis behavior effect. The correction consists of defining an effective  $F'_{\nu_e}$  by:

$$F'_{\nu_e} = 1 + C_D (F'_{\nu} - 1) \quad (5-25)$$

$$F_{\nu_e} = F'_{\nu_e} R$$

Based upon the results presented in Reference 4 plus those obtained herein, it is estimated that for longer duration ground motions:



$$C_D = 0.6$$

(5-26)

With this correction,  $F_{\mu_e}$  and  $\bar{S}_a^v$  are also tabulated in Table 5-5.

After the above defined effective duration correction is made, the Effective Riddell-Newmark Method does an equally excellent job of estimating  $\bar{S}_a$  as does the Spectral Averaging Method. At  $\mu = 3.3$ , it overpredicts  $\bar{S}_a$  by 12% whereas the Spectral Averaging Method underpredicted by 11%. At  $\mu = 23.2$ , the Effective Riddell-Newmark Method underpredicts by 2% whereas the Spectral Averaging Method overpredicts by 4%. Thus, as shown in Table 5-5, averaging the results from both methods provides a nearly exact prediction in those two cases.

It is recommended that for longer duration ground motion and pinched shear wall type hysteretic behavior,  $F_{\mu}$  be predicted by both the Spectral Averaging Method and by the Effective Riddell-Newmark Method as described, herein. When the  $F_{\mu}$  estimates from those two methods agree with each other within a factor of about 1.3, then the predicted  $F_{\mu}$  value should be taken as the average of the two values. When the two methods produce  $F_{\mu}$  values which differ from each other by more than a factor of about 1.3, the results of both methods should be viewed with great caution. This latter case is not expected to happen often.



Following the above recommendation, the median fragility corresponding to a maximum story drift of 0.7% or  $\mu = 11.5$ , is estimated to be  $\bar{S}_a^v = 4.39g$  which is 5% less than that shown in Equation 5-4 based upon the nonlinear time-history analyses. It is concluded that for the Turbine Building, the median fragility can be accurately estimated using Equation 5-5 and elastic analysis results. This same conclusion should be equally applicable to the other Diablo Canyon buildings where nonlinear analysis results are not available.

It is also necessary to estimate the randomness variability of the median fragility curve as defined by Equation 5-6. The needed randomness variability  $\beta_{R_{F_\mu}}$  is made up of two parts. The first part,  $\beta_1$ , consists of the random scatter of time-history computed  $F_\mu$  values versus that predicted by the above defined prediction approach. The second part,  $\beta_2$ , consists of the randomness variability in  $F_\mu$  due to the randomness variability of  $\mu_s$  corresponding to severe wall damage.

The random scatter of time-history computed  $F_\mu$  values versus the predicted  $F_\mu$  values can be estimated for the Spectral Averaging Method using the results presented in NUREG/CR-3805 (Reference 4). On this basis, it is estimated that :



Spectral Averaging Method

$$\beta_1' = 0.06 + 0.03 [F_{\mu}^v - 1.0] \quad (5-27)$$

where  $F_{\mu}^v$  is the median estimate of  $F_{\mu}$  used in Equation 5-6 to estimate  $\frac{v}{S_a}$ . With  $F_{\mu}^v$  estimated to be 2.10,  $\beta_1$  becomes 0.093. However, much of  $\beta_1$  comes about because of the local peak and valley variability of the response spectrum obtained from the input time-history. This variability has already been included in the  $\beta_{RR} = 0.215$  estimate contained in Equation 5-6. It would therefore be wrong and potentially excessively over conservative to add in the full  $\beta_1$  estimate. Thus,  $\beta_1$  should be reduced by a correction factor  $\alpha$ :

$$\beta_1' = \alpha \beta_1 \quad (5-28)$$

where  $\alpha$  must be judgmentally estimated. Whenever,  $\beta_1$  is much smaller than  $\beta_{RR}$ , the value of  $\alpha$  selected is unimportant. However, the value of  $\alpha$  used becomes important when  $\beta_1$  approaches or exceeds  $\beta_{RR}$ . Based purely on judgement, it is suggested that  $\alpha$  be taken as 0.4. Thus,  $\beta_1'$  becomes 0.037. Even though Equation 5-27 is strictly only correct when the Spectral Averaging Method is used, it is considered to also be applicable for the approach recommended herein for obtaining  $F_{\mu}$ .



The random variability of story drift associated with severe damage was defined by Equation 2-5 to be 0.15. This same variability also applies to  $\mu_s$ . Using this  $\beta_{R\mu}$ , it is computed that a maximum drift of 0.4% lies at  $-3.73 \beta_{R\mu}$  below the median estimates of damaging drift of 0.7%. Correspondingly, from Table 5-3, it is estimated that a system ductility  $\mu$  of 6.0 lies at  $-3.73 \beta_{R\mu}$  below the median value of 11.5. Thus,  $\beta_2$  may be estimated using the  $\bar{S}_a$  values in Table 5-5 for these two system ductilities:

$$\beta_2 = \frac{\ln \left[ \frac{\bar{S}_a(\mu=11.5)}{\bar{S}_a(\mu=6.0)} \right]}{3.73} = \frac{\ln \left[ \frac{4.39}{3.50} \right]}{3.73} = 0.061 \quad (5-29)$$

The combined  $\beta_{R\mu}$  is then obtained from:

$$\beta_{R\mu} = [(\beta_1)^2 + (\beta_2)^2]^{1/2} \quad (5-30)$$

to be 0.071. The median (randomness only) fragility variability is then obtained from Equation 5-6. Thus, from the elastic analysis results, the median (randomness only) fragility curve is estimated to be:



Median (Randomness Only) Fragility Curve

$$\text{Median } \frac{V}{\bar{S}_a} = 4.39g$$

(5-31)

$$\beta_R = 0.23$$

These results which are based upon the extrapolation of a single median-centered elastic response spectrum analysis are within 5% of the results presented in Equation 5-4 obtained from 50 nonlinear time-history analyses (25 each at  $\bar{S}_a = 3.0g$  and  $\bar{S}_a = 6.0g$ ).

5.3 Influence of Ground Motion Characteristics on Shear Wall Drift

Although the primary purpose of the nonlinear time-history analyses was to provide a fragility estimate for the Turbine Building in support of the Seismic Probabilistic Risk Assessment, a secondary purpose was to better understand the characteristics of ground motion capable of damaging the Turbine Building shear walls. To serve this second purpose, characteristics of the response spectra shown in Figures 3-1 through 3-25 are compared with the maximum story drifts presented in Table 5-1 for  $\bar{S}_a = 3.0g$  for each record.

Basically, all of the records were linearly scaled to have the same 5%



damped average spectral acceleration  $\bar{S}_a$  in the 3 to 8.5 Hz frequency range. It was judged that  $\bar{S}_a$  was the best single parameter descriptor of the potential for damage to the Turbine Building shear walls from the various ground motion records. However, with all 25 records scaled to  $\bar{S}_A = 3.0g$ , Table 5-1 illustrates that the maximum story drift ranged from a low of 0.05% to a high of 0.69% of the wall segment height, with a median value of 0.22%. A similarly large scatter also holds for the 25 records scaled to  $\bar{S}_a = 6.0g$ . Furthermore, in both cases the maximum story drifts are reasonably uniformly distributed within these broad ranges as shown in Figure 5-2 which presents plots of the natural logarithm of maximum story drift ordered from the lowest to highest values versus cumulative non-exceedance probability plotted on a cumulative normal probability scale. If drifts were distributed lognormally, the points would lie on a straight line on this plot. It can be seen from Figure 5-2 that the assumption of a lognormal distribution of maximum drifts is reasonable for both  $\bar{S}_a = 3.0g$  and  $\bar{S}_a = 6.0g$  particularly for a range of maximum drifts from 0.10% to 2.0% which far exceed the drift range of primary interest (0.5% to 1.0%). Assuming the straight-line lognormal distribution shown on Figure 5-2, the logarithmic standard deviation for maximum story drift are 0.75 and 0.50 for  $\bar{S}_a = 3.0g$  and  $6.0g$ , respectively. Such large dispersion indicates that  $\bar{S}_a$  does not serve as a good descriptor of maximum story drift. Yet, in a brief investigation, no better single



parameter was found. It appears that the detailed, multiple-frequency characteristics of the response spectrum of each record is important. Therefore, for  $\bar{S}_a = 3.0g$ , these additional frequency characteristics are described versus the resultant maximum story drifts.

At  $\bar{S}_a = 3.0g$ , Record 18 produced the largest story drift of 0.69%. As shown in Figure 3-18, this record contains particularly high spectral accelerations from 1.5 to 2.3 Hz with the 5% damped spectral acceleration spiking to 5.5g at 2.0Hz. Records 15, 20, and 23 contained similar, but lesser low frequency spikes. All three of these records contain particularly high spectral acceleration from 2.1 to 3.3 Hz spiking above 5.0g at 2.6 Hz. Records 15 and 20 produced the second and third highest story drifts of 0.61% and 0.59%, respectively. For some reason, Record 23 with a spectrum very similar to that of Records 15 and 18 produced a lesser, but still moderately high drift of 0.32%. These are the only 4 records with 5% damped spectral acceleration below 3.0 Hz which approach or exceed 5.0g. Obviously the spectral acceleration in the 2.0 to 3.0 Hz range had an important influence on the maximum shear wall story drifts for  $\bar{S}_a = 3.0g$ .

Record 24 produced the fourth highest drift of 0.43%, but it occurred in Wall 19 rather than Wall 31 which had the highest drift in nearly all other cases. For Record 24, the maximum story drift in Wall 31 was only



0.29%. The spectrum from Record 24 differs from that of any of the other records in that it contains two spikes rather than one spike in the 2.0 to 3.0 Hz range. Both spikes are to about 3.3g with one centered at 2.0 Hz and the other at 2.6 Hz. Because of these two spikes, the average spectral acceleration in the 2.0 to 3.0 Hz range is generally high, although not as high as that for any of the other 10 records which produced maximum story drifts in excess of 0.25%. It is believed that the high spike to above 4.0g at 7.0 Hz on the Record 24 response spectrum played a major role in contributing to the large drift of Wall 19 which had an elastic model frequency of 9.5 Hz.

The response spectra for Records 2 and 22 both contain spikes to about 4.0g at about 2.0 Hz. Yet Record 2 produced the fifth highest maximum story drift of 0.42% while Record 22 produced a maximum story drift of 0.19% which is less than a median story drift for  $\bar{S}_a = 3.0g$ . Record 2 also contains high spectral acceleration in the 3.5g to 4.5g range over the 6.0 Hz to 9.0 Hz frequency range, whereas Record 22 has low spectral acceleration ranging from 1.8g to 3.2 g in this same 6 Hz to 9 Hz frequency range. It becomes clear that records must have high spectral accelerations of at least 3.5g both in the 6 to 9 Hz range and in the 2 to 3 Hz range to produce maximum story drifts in excess of 0.4%. The 6 to 9 Hz frequency range is important to initiate strong inelastic response of the shear walls, while the 2 to 3 Hz frequency range is



important to carry these drifts out to at least 0.4% maximum story drift. Missing either characteristic is sufficient to prevent large story drifts.

Records 5, 6, 9 and 16 all had similar characteristics of a high spectral acceleration spike between 3.5g and 4.4g at frequencies between 1.9 and 2.6 Hz coupled with moderately high spectral acceleration between about 2.5g and 3.5g in the 6 to 9 Hz frequency range. These 4 records exhibited maximum story drifts ranging from 0.26% to 0.38%. On the other hand, Record 25 also had a 5% damped spectral acceleration spike of about 4.2g near 2.8 Hz but had spectral accelerations less than 2.0g above 8.3 Hz so that the Turbine Building shear walls never began to drift significantly inelastically. For this reason, both the 2.8 Hz spike to 4.2g and the 7 Hz spike to 3.8g were ineffective and a below median maximum story drift of 0.19% resulted.

Record 17 does not contain any high spectral acceleration spike in the 2 to 3 Hz range. However, its spectral acceleration does spike above 4.5g in the 3.5 to 3.7 Hz range and although dropping, it remains above 3.7g at 3.6 Hz. This record produced a maximum story drift of 0.28%.



These 13 records were the only records which had

$$S_{a5\%} \geq 3.75g \text{ in the 2.4 to 2.8 Hz frequency range}$$

or

$$S_{a5\%} \geq 3.0g \text{ in the 1.7 to 2.0 Hz frequency range}$$
(5-32)

Eleven of these records produced maximum story drifts in excess of 0.25% for  $\bar{S}_a = 3.0g$ . None of the 12 records which did not exceed either of the two conditions of Equation 5-32 produced maximum story drift in excess of 0.25%. Two of the records which did exceed at least one of the conditions of Equation 5-32 produced drifts of only 0.19% because they did not possess sufficient spectral content in the 8.6 Hz to 9.5 Hz frequency range necessary to initiate significant inelastic response. Thus, in addition to exceeding one of the two conditions of Equation 5-32, it is also necessary to exceed

$$S_{a5\%} \geq 2.1g \text{ in the 8.6 to 9.5 Hz frequency range} \quad (5-33)$$

in order to achieve maximum story drifts in excess of 0.25% for the median structural model.

In other words, with median properties, the Turbine Building shear walls can only be potentially damaged by ground motion with broad frequency



2  
11  
2